COASTAL MICROSTRUCTURE:

FROM ACTIVE OVERTURN TO FOSSIL TURBULENCE

A Dissertation

by

PAK TAO LEUNG

Submitted to the Office of Graduate Studies of
Texas A&M University
in partial fulfillment of the requirements for the degree of

DOCTOR OF PHILOSOPHY

December 2011

Major Subject: Oceanography

Coastal Microstructure: From Active Overturn to Fossil Turbulence

COASTAL MICROSTRUCTURE:

FROM ACTIVE OVERTURN TO FOSSIL TURBULENCE

A Dissertation

by

PAK TAO LEUNG

Submitted to the Office of Graduate Studies of
Texas A&M University
in partial fulfillment of the requirements for the degree of

DOCTOR OF PHILOSOPHY

Approved by:

Chair of Committee,	David Brooks
Committee Members,	Robert Hetland
	Achim Stössel
	Scott Socolofsky
Head of Department,	Piers Chapman

December 2011

Major Subject: Oceanography

ABSTRACT

Coastal Microstructure: From Active Overturn to Fossil Turbulence.

(December 2011)

Pak Tao Leung, B.S., University of California;

B.A., University of California; M.S., University of California

Chair of Advisory Committee: Dr. David Brooks

The Remote Anthropogenic Sensing Program was a five year effort (2001- 2005) to examine subsurface phenomena related to a sewage outfall off the coast of Oahu, Hawaii. This research has implications for basic ocean hydrodynamics, particularly for a greatly improved understanding of the evolution of turbulent patches. It was the first time a microstructure measurement was used to study such a buoyancy-driven turbulence generated by a sea-floor diffuser. In 2004, two stations were selected to represent the near field and ambient conditions. They have nearly identical bathymetrical and hydrographical features and provide an ideal environment for a control experiment. Repeated vertical microstructure measurements were performed at both stations for 20 days. A time series of physical parameters was collected and used for statistical analysis. After comparing the data from both stations, it can be concluded that the turbulent mixing generated by the diffuser contributes to the elevated dissipation rate observed in the pycnocline and bottom boundary layer.

To further understand the mixing processes in both regions, data were plotted on a Hydrodynamic Phase Diagram. The overturning stages of the turbulent patches are identified by Hydrodynamic Phase Diagram. This technique provides detailed information on the evolution of the turbulent patches from active overturns to fossilized scalar microstructures in the water column. Results from this study offer new evidence to support the fossil turbulence theory.

This study concluded that:

1. Field Data collected near a sea-floor outfall diffuser show that turbulent patches evolve from active (overturning) to fossil (buoyancy-inhibited) stages, consistent with the process of turbulent patch evolution proposed by fossil turbulence theory.
2. The data show that active (overturning) and fossil (buoyancy-inhibited) patches have smaller length scales than the active+fossil (intermediate) stage of patch evolution, consistent with fossil turbulence theory and with laboratory studies.
3. Compared to a far-field reference, elevated dissipation rates near the diffuser were found in the seasonal pycnocline as well as in the bottom boundary layer.
4. More than 90% of the turbulent patches observed in the water column were non-overturning (active+fossil and fossil). Such patches can provide significant mixing in the interior of the ocean, far from surface and bottom boundary layers.

DEDICATION

To my mother, Anna, who was not able to wait till it is over

and

my wife, Amber, who cannot wait to have it be over.

ACKNOWLEDGEMENTS

I would like to thank my committee chair, Dr. Brooks, and my committee members, Dr. Hetland, Dr. Socolofsky, Dr. Stössel, and Dr. Smith for their guidance, support, and interest in this research and my success.

Special thanks to Dr. Gibson, who showed me how to fight for what you believe, Dr. Prandke, who showed me how to be a good scientist, and Dr. Anis, who showed me how to be a dedicated researcher.

Thanks also go to my friends, colleagues, and the department faculty and staff for making my time at Texas A&M University a great experience. I also want to extend my gratitude to Dr. Keeler, Mr. Gibbons, Mr. Burdette, Ms. Trujillo, Ms. Cooper, and everyone involved in the RASP.

Finally, thanks to my mother and father for their encouragement and to my wife for her patience and love.

TABLE OF CONTENTS

LIST OF FIGURES

Page

Page

Page

Page

Page

Page

Page

LIST OF TABLES

Page

Page

CHAPTER I
INTRODUCTION

1.1 Background

Most flows in natural or engineering settings are turbulent. Turbulence, where eddy-like motions are dominated by inertial - vortex forces, occurs in the ocean, atmosphere, galaxy, and universe. Examples of turbulence include smoke columns, the wakes of submarines and planes, flow in an oil pipeline, the jet stream in the troposphere, and self-gravitating clouds in the plasma universe before galaxy formation. The present distribution of galaxies in space was suggested to be "fossilized turbulence" in the primordial gas immediately preceding the formation of galaxies [*Gamov*, 1954]. *Feynman* [1963] said that the analysis of turbulent fluids is a physical problem that is common to many fields, but is yet unsolved. Nearly fifty years later, many still believe that forming a theoretical model to describe the behavior of turbulent flow remains an unsolved problem in physics. The study of marine turbulence is perhaps one of the biggest challenges because of the harsh environment of the open sea and the limited access to the deep ocean. Observations of turbulence can only provide "snapshots" of the water columns or layers. Hence, a given volume of water typically is observed only once.

Knowledge of turbulence often depends on the understanding of turbulent eddies, which are the most fundamental elements in the mixing processes. *Davidson* [2004] defined an eddy as "a blob of vorticity and its associated velocity field". One everyday example is the eddies formed when pouring cream into fresh coffee; an irregular swirling blob of cream with high vorticity that rapidly disperses in the warm

---

This dissertation follows the style of *Journal of Geophysical Research*.

beverage. The cumulus cloud in Vincent van Gogh's *The Starry Night* resembles the clouds of gas surrounding a variable star which has striking similarities to turbulent eddies. What are the similarities between the eddies found inside the cup of coffee and those found in the mixing layer of the open ocean? What do they tell us about fluid motions and mixing processes? These questions are the motivation behind studies of turbulence in natural flows. Researchers have been developing techniques to observe, identify, and characterize turbulent eddies for almost a century. It is not until the recent decades that modern electronic technologies have finally caught up with human curiosity.

1.2 Definition of Active and Fossil Turbulence

A scientific property is described or defined by how it is measured, as opposed to a vague or general description. For example, the color red is defined as electro-magnetic waves with a wavelength between 630 and 740 nm, opposed to describing it as the color of a ripe apple, which is less specific. Similarly, force is defined as the product of mass and acceleration of an object, hence, force only exists for non-zero acceleration. New theories often arise upon the realization that certain properties had not previously been sufficiently defined. Einstein's work on relativity begins by defining simultaneity and length, while Newton skipped over them with "I do not define time, space, place, and motion, as being well known to all. Only I must observe that the common people conceive those quantities under no other notions but from the relation they bear to sensible object." Einstein's work does not replace Newton's; instead, it offers a more sophisticated view of the subject. They are now known as the classical mechanics and the relativistic mechanics and both play important roles in all aspects of physics. Similarly, fossil turbulence theory plays an important role in ocean turbulence study by providing a more sophisticated view to the mixing process.

Widespread disagreement on a definition has greatly complicated the study of marine turbulence. For a range of views on turbulence, see *Riley and DeBruynKops* [2003], *Fernando* [1988], *Gourlay et al.* [2001], *Itsweire et al.* [1993], *Ivey and Imberger* [1991], *Ivey et al.* [1992], *Luketina and Imberger* [1989], *Smyth and Moum* [2000], *Winters and D'Asaro* [1996], *Winters et al.* [1995] and other references discussed here in context.

What are the fundamental properties of turbulence? How does buoyancy affect turbulence? Do random temperature fluctuations in microstructure indicate that the fluid is turbulent? Turbulence is a property of fluid flows that has been notoriously difficult to define. *Libby* [1996] requires a wide spectrum of velocity fluctuations to distinguish turbulence from "unsteady laminar flow". *Frisch* [1995] also emphasizes the importance of high Reynolds numbers. *Stewart* [1969] offers a syndrome definition that lists various commonly-accepted properties of turbulence. Similarly, *Tennekes and Lumley* [1972] list irregularity, diffusivity, large Reynolds number, three-dimensional vorticity fluctuations, and large dissipation rates as distinguishing properties of turbulence, and this approach is continued by *Pope* [2000]. These varying definitions of turbulence are best summarized by G. K. Vallis, “What is Turbulence? Turbulence is like pornography. It is hard to define but if you see it, you recognize it immediately.” [*Gibson*, 1999]

Without a narrow definition of turbulence, unique signatures of some phenomena, like fossil turbulence or Coriolis-inertial waves, will be lost and all observed scalar and vector patches will be considered as turbulence. A more precise definition for buoyancy turbulence is provided implicitly by *Gibson* [1980] and explicitly by *Gibson* [1991, 1996, 1999]. It states that

Active turbulence *is an eddy-like state of fluid motion where the inertial-vortex forces of the eddies are larger than any of the other dampening forces.*

This turbulence definition, based on the inertial-vortex force (per unit mass) $\vec{v} \times \vec{\omega}$, where $\vec{v}$ is the velocity and $\vec{\omega}$ is the vorticity of the shear flow. It is designed to exclude

all flows and mixing processes as non-turbulent that depart from universal similarity laws of Kolmogorov, even though they may fit broad-syndrome definitions frequently used in oceanography.

A very important characteristic of turbulence is that it produces highly persistent, irreversible effects in a variety of hydro-physical fields. Linear waves come and go without leaving any trace, but turbulence is intrinsically irreversible and leaves remnant hydro-physical signatures. Such signatures are described by terms like “fossil turbulence” or “remanent turbulence”. In meteorology, it is well known as the inhomogeneities of temperature and humidity that remain in air after the motion which produced them has subsided and the density has become uniform; this causes scattering of radio waves, and lumpy clouds when air is rising. The effects of such fossils on turbulence investigations are well documented in most physical sciences, for example: astrophysics [*Cloutman & Whitaker*, 1980; *Vernin et al*, 2000], atmospheric physics [*Ruggiero*, 2007] and [*Jones et al.*, 2010], computational fluid mechanics [*Shen et al.*, 2009], and radio science [*Woods*, 1969]. In the ocean, the definition by *Turner* [1973] and *Gibson* [1980] can be summarized as:

Fossil turbulence *is defined as a fluctuation in any hydro-physical field produced by turbulence that persists after the fluid is no longer actively turbulent at the scale of the fluctuation.*

Fossil turbulence can be easily observed by pouring cold cream into a transparent cup with hot coffee. The jet of cream produces overturning turbulence (active turbulence), which usually fails to entrain all of the lighter fluid before it is converted to internal wave motions by buoyancy forces. The remnant fluctuations of cream (fossil cream turbulence) can be seen to persist for a relative long period as indicated by the bobbing motions in the cup. It can also be noticed that the eddies start from small length scale and rapidly expand [*Gibson*, 1980; *Leung and Gibson*, 2004]. However, the energy would cascade from large scale to small from the mean flow. As they grow in size, the

overturning motion slows down and eventually comes to a stop (dissipated). The cloud of cream would not disappear immediately once the overturning motion dissipated. If the coffee is allowed to sit aside without any disturbance, that cloud of cream eventually diffuses into the coffee, becoming undetectable. Several observations can be made from this simple daily life example: 1) overturning patch cascade from small scale to large until it reaches the critical size; 2) the overturning motion is damped out as the patch grows in size; 3) scalar (cream, density, temperature) structures remain after the velocity microstructure dissipates; and 4) stirring and mixing happen at different stages of the process.

It is not difficult to imagine similar processes occurring in the ocean; for example, when sewage is being ejected into the ocean from the outfall diffusers, or when fresh water mixes with sea water in estuaries. Active turbulence is rare in the ocean because it is rapidly damped by buoyancy, Coriolis, viscous, and other forces. Potential entropy, represented by the variance of temperature, salinity, or density, is produced by the stirring resulting from active overturns. The scalar fluctuations are gradually and irreversibly mixed later and elsewhere by active+fossil and fossil turbulence to produce the entropy of mixing. Most mixing and diffusion in the ocean is initiated by active turbulence, but is then completed by fossil turbulence.

However, due to the length and time scales of those processes in the ocean, observation can only be made by obtaining snapshots of the water column in the form of vertical profiling. Problems arose when such snapshots were used to explain the turbulent events. For example, scalar microstructures were often misinterpreted as active overturns, or insufficient data were collected to cover the entire process. Accurate marine turbulence measurements were often difficult to obtain due to instrumentation limits. Without long data records capturing the evolving turbulent events [*Baker and Gibson, 1987*], signatures of fossil turbulence were often misinterpreted or simply ignored. Analytical tools to study evolving turbulent events, such as different versions of Hydrodynamic Phase Diagrams (HPD), were developed [*Gibson,* 1980; *Ivey and Imberger,* 1991], but seldom utilized due to the lack of data. HPDs also aid in the

identification of the sources of turbulence within a region of interest and offer an alternative view for understanding different phases of a evolving patch.

1.3 Turbulent Patch Identification

Engineers often deal with non-stratified flows with limited Reynolds numbers; in contrast, oceanographers study marine turbulence influenced by both stratification and shear. Experiments with turbulence in natural flows are difficult to conduct in the laboratory because of the large range of spatial and temporal scales of the patches. Hence, oceanographers have relied on data collected from field observations. As early as 1919, G. I. Taylor used current-meter measurements to estimate the rate at which kinetic energy was dissipated by the tides through turbulence in shallow seas [*Taylor*, 1919; *Batchelor*, 1996].

The length scale of ocean mixing is in the order of a few centimeters. This requires specialized ‘microstructure’ instruments such as shear probes and high resolution temperature probes. It was not until 1980s that fast-response sensors became available and reliable enough for free-falling profilers to observe high frequency micro-scale velocity and scalar fluctuations. The energy dissipation rates and overturn scales can then be estimated. Since then, one of the major objectives of analyzing microstructure profiles is to identify turbulent patches and compute their characteristic vertical lengths.

Several algorithms for the identification of overturning turbulent patches from microstructure density profiles have been proposed (Figure 1). They are usually derived from Thorpe's method [*Thorpe*, 1977], which rearranges the observed density profile $\rho(z)$ into a stable monotonic reference density profile $\rho_m(z)$ which contains no inversions. Density fluctuations and Thorpe displacements can then be computed. A density fluctuation, defined as $\rho'(z) = \rho(z) - \rho_m(z)$, indicates the change in density before and after the mixing event. Thorpe displacement $d_T(z)$ is the vertical distance that an individual fluid parcel of the observed profile ρ(z) must be moved in order to generate the stable monotonic density profile $\rho_m(z)$. The Thorpe scale L_T is defined as the root mean square of the Thorpe displacement, and is proportional to the mean eddy size. Statistical properties of $\rho'(z)$ or $d_T(z)$ profiles are usually the main input for the algorithms of turbulent patch identification, whereas L_T is an important parameter when characterizing an eddy. Unfortunately, there is no accepted statistical model of overturning that can be used as a reference for validating the computed density fluctuation or Thorpe displacement profiles. The lack of any theoretical model has led to the search for methods of turbulent patch identification based on realistic reasoning and empirical parameters.

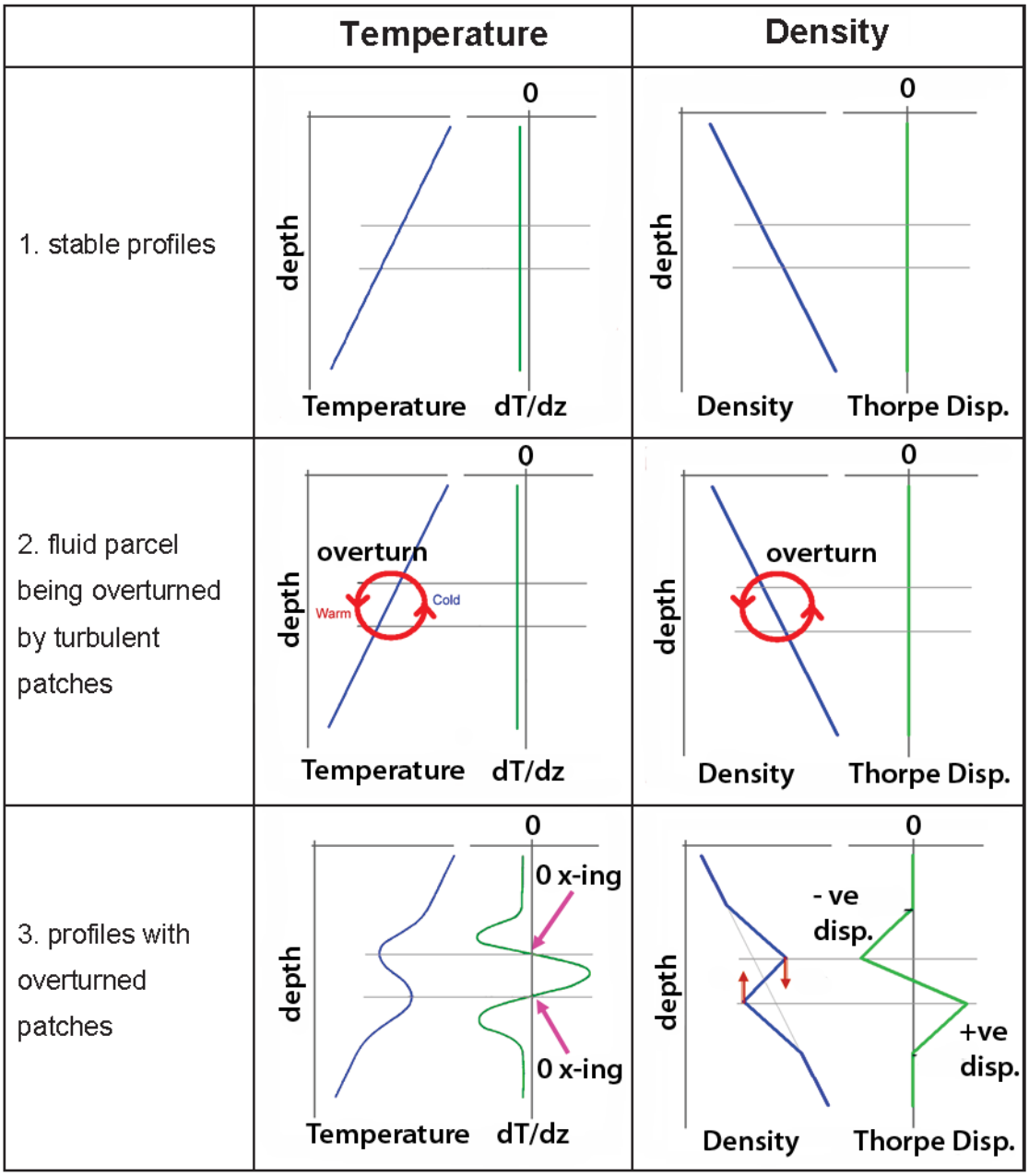

Figure 1. Schematics of overturns disturbing a stably stratified water column and how such overturns can be identified from temperature, dT/dz, density, and Thorpe displacement profiles. Overturn turn patch can be defined from dT/dz by zero-crossing method or from non-zero Thorpe displacement values.

Dillon [1982] defined a complete overturn as a region where no heavier or lighter fluid parcels in $\rho(z)$ relative to $\rho_m(z)$ are found outside the patch, and no heavier or lighter fluid particles relative to $\rho_m(z)$ outside the patch are found within it. *Gregg* [1980] proposed zero-crossing counting as an alternative method for turbulent patch identification. In this method, a turbulent patch is identified as the depth interval at which the distance between consecutive zero crossing density fluctuations are smaller than a certain threshold. To avoid potential artifacts caused by instrumental noise, only strongly pronounced patches, which imply a relatively high background density gradient, are usually considered [*Prandke and Stips*, 1992]. *Moum* [1996a,b] proposed two conditions to validate a turbulent patch. 1) Patches should contain only data with significantly different fluctuation signals from their respective noise levels; 2) patches must have well defined upper and lower boundaries. These conditions require that the patch size (L_p) be smaller than the maximum Thorpe displacement (L_{Tmax}) throughout the patch and the sum of the Thorpe displacement over the depth range of the patch is required to be 0 (i.e. $\int d_T(z)dz = 0$).

1.4 Turbulent Patch Classification

Once turbulent patches are identified from the microstructure density profiles, their characteristic vertical length can be computed to understand the mixing events. Such vertical length scales include Thorpe scale, Kolmogorov scale, and Ozmidov scale. The Thorpe scale (L_T) is the root-mean-square value of the Thorpe displacement (d_T) which characterized the vertical length of the observed overturning patch in vertical profile [*Thorpe*, 1977]. The Kolmogorov scale [*Kolmogorov*, 1941] is

$$L_K = (\nu^3/\varepsilon)^{1/4} \quad (1)$$

is an estimate of the smallest length scale for a turbulent eddy, where ν is kinematic viscosity and ε is the turbulent dissipation rate of the eddy. Physically, it is the length scale where the viscous forces are balanced with the inertial forces and become significant to the overturn. With the Kolmogoroff-Obukhov law:

$$U = (\varepsilon L)^{1/3} \tag{2}$$

where U and L are the characteristic velocity and characteristic length, L_K can relate to Reynolds number (*Re*) with

$$Re = (\varepsilon L^4)^{1/3}\nu^{-1} = UL_K\nu^{-1} \tag{3}$$

When *Re* is supercritical, viscous forces become insignificant to the flow. The Ozmidov scale [*Ozmidov*, 1965], defined as

$$L_O = (\varepsilon/N^3)^{1/2} \tag{4}$$

where N is the buoyancy frequency, is the vertical size of the largest eddies which can overturn in stably stratified water. Buoyancy has only a minor effect at small scales but is more significant at larger scales. This explains why the overturning motion slows down as the turbulent patch increases in size. With Equation 2, L_O can be related to Froude number (*Fr*) by

$$Fr = (\varepsilon)^{1/3}N^{-1}L^{-2/3} = U/(NL_O) \tag{5}$$

If $Fr < 1$ (subcritical), buoyancy is significant and inhibites the turbulent patch from overturning. Equation 3 and 5 are often referred to as the turbulent Reynolds number (Re_T) and the turbulent Froude number (Fr_T). They are the largest and smallest scales of an overturning patch.

Much debate has centered on the relationship of the Ozmidov length scale L_O, and the overturn scale L_T at the initiation of turbulence. Observations [*Dillon*, 1982; *Peters et al*., 1988; *Seim and Gregg*, 1994] from measurements in the ocean thermocline show that the value of L_O has good agreement with the estimated overturn length scale L_T. However, *Gibson* [1987a] suggested that in the initial stages of a mixing event, L_O could be much larger than L_T, but with the development of the turbulence, L_T would approach L_O. This scenario has also been observed in laboratory experiments on grid-generated turbulence.

Information on the evolution of the mixing events can be obtained by studying the fundamental length scales, L_T, L_K, L_O, and their ratios. For example, when the ratio of L_O to L_K (the intermittency factor) is sufficiently large, the length scale of the largest overturning eddies and the smallest are well separated, providing a broad spectral range of turbulent eddies, the smallest of which may have isotropic properties [*Gargett et al*., 1984]. The ratios L_T to L_O and L_T to L_K can be used to define the turbulent Froude number $Fr_T = (L_O/L_T)^{2/3}$ and the turbulent Reynolds number $Re_T = (L_T/L_K)^{4/3}$, respectively [*Luketina and Imberger*, 1989]. With the ratio of L_O and L_K, *Imberger and Boashash* [1986] defined the small-scale Froude number as $Fr_S = (L_O/L_K)^{2/3}$. Since there are only three independent length scales, the three dimensionless numbers can all be defined in terms of the ratio of any two of these length scales. Hence, the three dimensionless numbers are not independent and are related by $Fr_T = (Re_T)^{-1/2} Fr_S$. This expression indicates that the large and small scale turbulent Froude numbers are connected by the turbulent Reynolds number, so the specification of the two parameters Fr_T and Re_T is sufficient to characterize the turbulence. The state of turbulence in a stratified fluid may thus be inferred from the Fr_T versus Re_T diagram [*Ivey and Imberger*, 1991]. While the Fr_T versus Re_T diagram can use to reflect the status of the current energy budget of the turbulence [*Imberger and Ivey*, 1991], *Gibson* [1987a] has implied that it can also be interpreted as an activity diagram, also known as a Hydrodynamic Phase Diagram (HPD), to describe the evolution of the turbulence.

According to the fossil turbulence theory, a turbulent patch undergoes evolution through three different phases during the stirring-mixing process: the active phase when the patch actively overturns, the fossil-active phase when the overturn is damped by buoyancy, and the fossil phase when the overturn is damped by both buoyancy and viscosity (Figure 2). Turbulent patches at the fossil phase are scalar microstructure (with no velocity microstructure), they remain after the turbulence that created them has decayed. Because vertical profiles can only provide a snapshot of the water column, it is impossible to distinguish active overturns from fossilized patches. As a result, all observed patches are typically considered to be active overturns although some of them are actually scalar microstructures. The difference between stirring and mixing then becomes indistinguishable. To overcome this problem and to provide a more accurate description of turbulent events, the technique of HPD was developed by classifying the hydrodynamic phase of the observed patches.

Different versions of turbulent activity diagrams have been introduced in the past [*Ivey and Imberger*, 1991] and all are based on the turbulence activity parameters (A_T). Values of A_T observed in the ocean range from slightly larger than 1, indicating active turbulence, to less than 10^{-2}. The average is about 0.25 from *Caldwell et al.* [1980]. A_T is related to the Froude number (Fr) of the overturn by

$$A_T = (Fr/Fr_o)^{3/4} \tag{6}$$

where Fr_o is the Froude number at fossilization (when the patch reaches Ozmidov scale and buoyancy becomes dominant). A_T can be plotted as a function of any parameter which gives a measure of the Reynolds number at log-log scales. This gives a "hydrodynamic phase diagram" (HPD) which is divided into four areas representing the four hydrodynamic states: active-turbulence, active+fossil-turbulence, fossil-turbulence, and non-turbulence (Figure 3 and Figure 4).

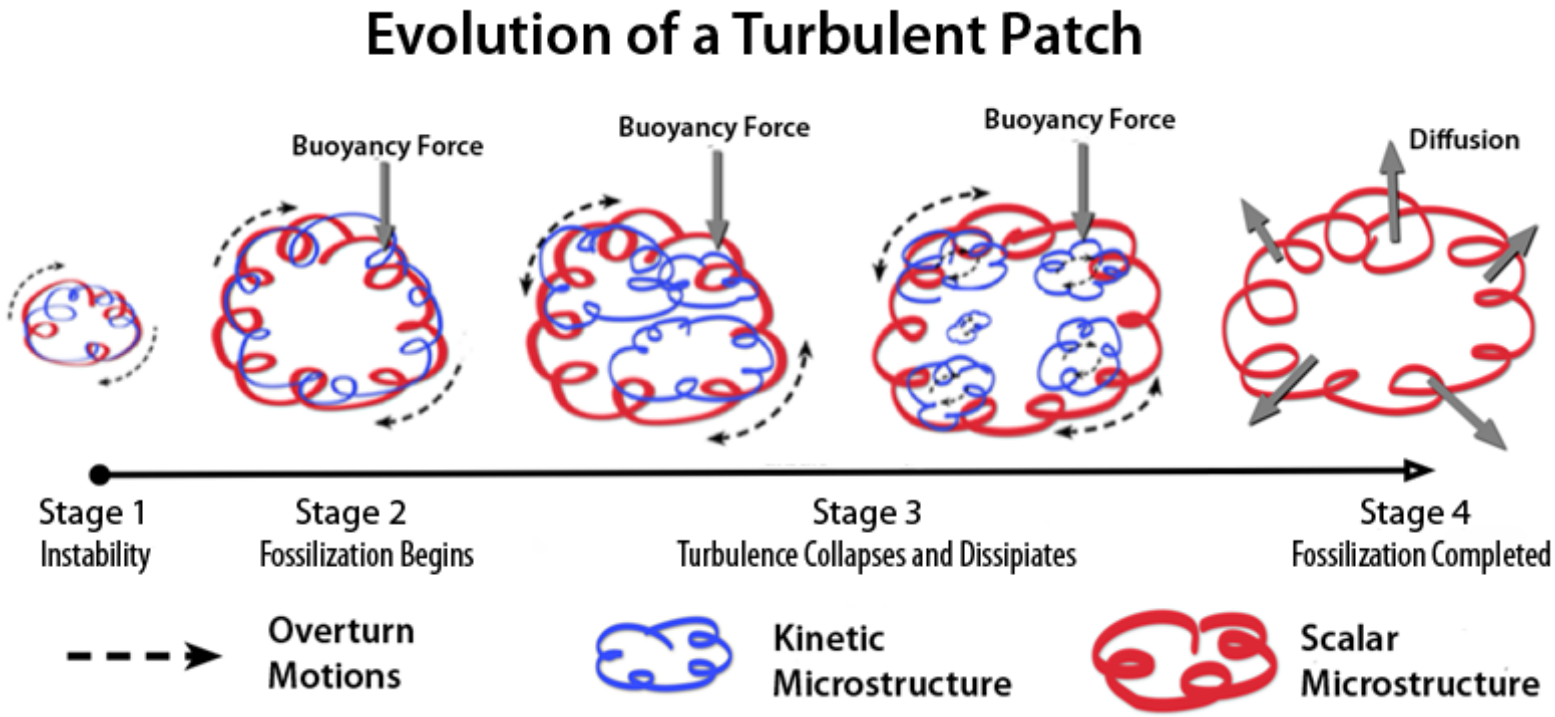

Figure 2. The evolution of a turbulent patch according to the Fossil Turbulence Theory. A shear layer will have instabilities that grow as waves (Stage 1). These waves grow into billows and collapse into patches of turbulence (Stage 2). Kinetic structures collapse and dissipate while the scalar structures retain the scale of the billows. In this stage, the large scale is fossilized while the small scale remains overturning. Kinetic structures (blue) collapse and dissipate. In this stage, the large scale is fossilized while the small scale remains active, hence the active+fossil phase (Stage 3). Eventually the kinetic structure dissipates, leaving only the scalar microstructure (red) as a remnant of the turbulence (Step 4) and the patch has become completely fossilized.

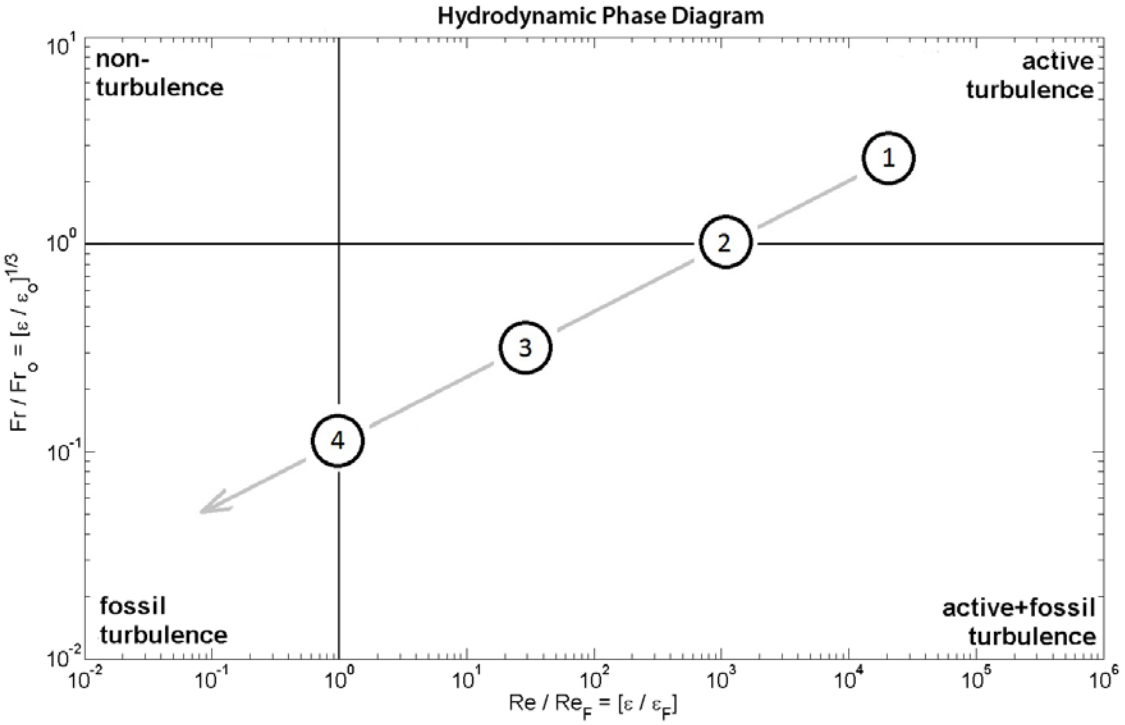

Figure 3. Four stages of an evolving turbulent patch as indicated in a Hydrodynamic Phase Diagram. For RASP 2004, the mean time scale between Stage 1 and 2 is 96 s, Stage 3 is 7 min, and Stage 4 is 17 min.

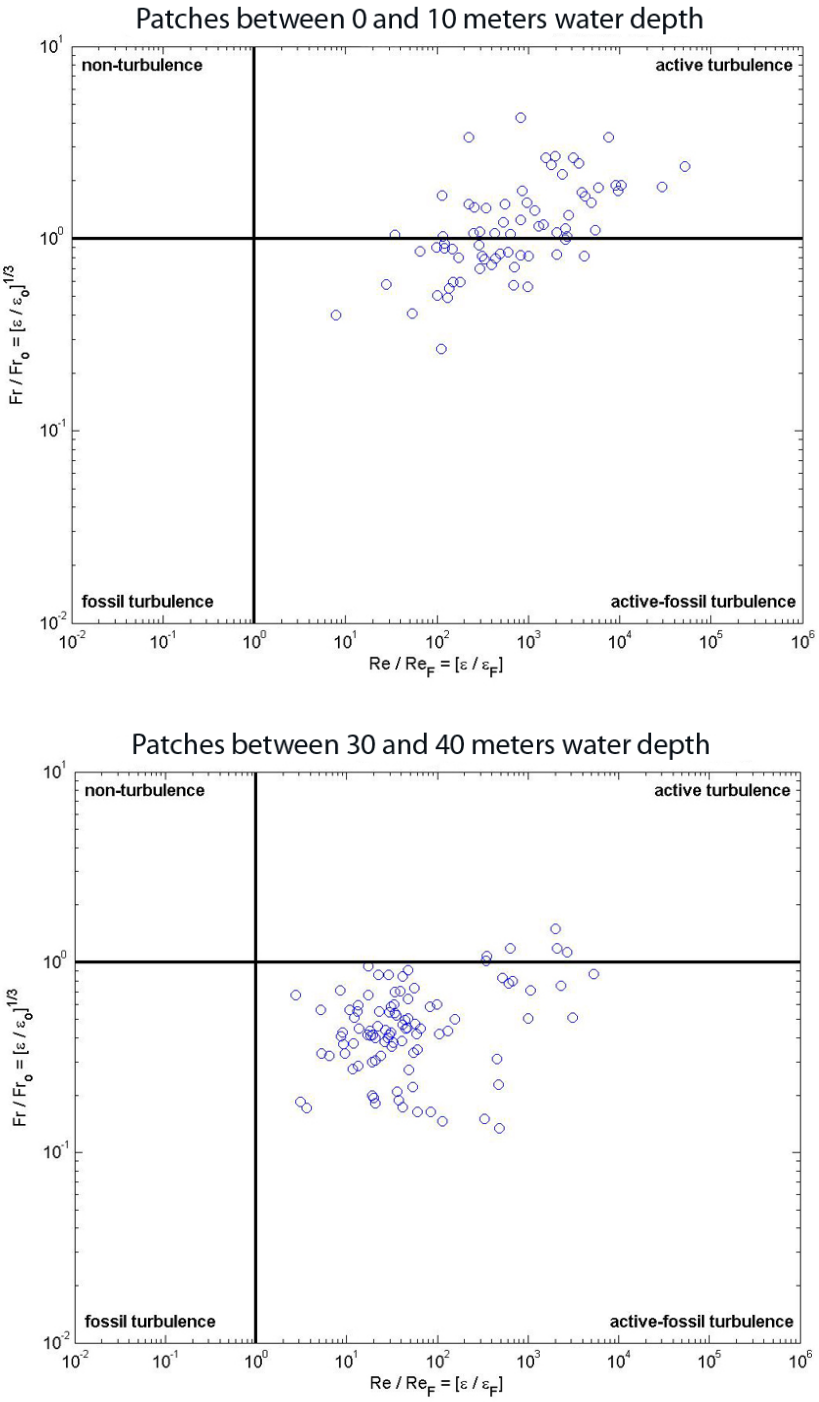

Figure 4. Hydrodynamic Phase Diagrams (HPD) of turbulent patches observed between the depth of 0 to 10m (top) and 30 to 40m (bottom) in a stratified water column. Each point on the HPDs represents one turbulent patch. More points in the active quadrant of the 0 to 10m HPD (top) indicate that the mixing is more active at that depth range than 30 to 40m. The active overturns are believed to be caused by wind stress induced turbulence on the surface.

A variation of HPD consisting of the normalized Froude number and the normalized Reynolds number was introduced by *Gibson* [1986]. This variant is widely accepted and is used for this study. The ordinate of the Gibson HPD is derived from the definition of Froude number (Equation 5). With Kolmogorov's second universal similarity hypothesis, Kolmogoroff-Oboukhov law (Equation 2) can be used for the characteristic velocity *U*. *Fr* is then normalized by Fr_o and gives

$$Fr/Fr_o = (\varepsilon/\varepsilon_o)^{1/3} \tag{7}$$

which is the ratio between the *Fr* of the observed patch with dissipation rate ε and a theoretical patch with identical *L* and *N* values at the beginning of fossilization with dissipation rate ε_o. Similarly, the abscissa of the HPD is derived from the definition of Reynolds number (Equation 3) with *U* from the Kolmogoroff-Oboukhov law and *L* is the Ozmidov Scale (Equation 4). Ozmidov Scale is used here because it represents the largest overturning scale. Then *Re* can be rewritten as $Re = \varepsilon/N^2\nu$ and the normalized Reynolds number becomes,

$$Re/Re_F = \varepsilon/\varepsilon_F \tag{8}$$

where ε_F is the dissipation rate for the patch at complete fossilization (the overturn motion is damped out by both buoyancy and viscous forces).

The dissipation rate ε_o when the overturning eddy is first affected by the buoyancy force can also be estimated from the maximum Thorpe overturn scale of the turbulent patch

$$\varepsilon_o = 3L_{T\,Max}^2 N^3 \tag{9}$$

[*Gibson et al*., 1993], where $L_{T\,Max}$ is the maximum Thorpe displacement of the patch. When the overturning motion of the patch is completely inhibited by the buoyancy force, its dissipation rate [*Gibson*, 1980] is given by

$$\varepsilon_F = 30\nu N^2 \tag{10}$$

Table 1 summarizes the definition of the different phases of a turbulent patch and their relationship with the corresponding parameters.

There are four quadrants on a HPD (Figure 4). Each quadrant represents one of the four hydrodynamic phases (i.e. active, active+fossil, fossil, and non-turbulence). Each turbulent patch identified by the density (or temperature) vertical profiles is represented by a point on the HPD. The location of the point on the diagram indicates the hydrodynamic phase of the corresponding turbulent patch and is determined by the values of normalized *Fr* and normalized *Re*. The upper right quadrant of the HPD represents patches that are fully turbulent because the normalized Froude number and the normalized Reynolds numbers are both supercritical ($\varepsilon \geq \varepsilon_o \geq \varepsilon_F$). Most patches in oceans and lakes are found in the active+fossil quadrant ($\varepsilon_o \geq \varepsilon \geq \varepsilon_F$), indicating that the largest scales are fossil and the smallest scales are active. The lower left quadrant of the HPD represents patches that are fully fossil turbulence patches ($\varepsilon_o \geq \varepsilon_F \geq \varepsilon$). With such a diagram, scalar microstructures can be distinguished from the active overturns. HPDs can improve the overall understanding of the water column because they show not just the strength but also the evolution of the turbulent event.

Table 1. Definition of Hydrodynamic Phases.

Hydrodynamic Phase	Definition
Active-Turbulence (overturning) $\varepsilon \geq \varepsilon_o$ and $\varepsilon \geq \varepsilon_F$	An eddy-like, nearly isotropic, state of fluid motion which arises when the inertial forces of the eddies are larger than either the buoyancy or viscous forces that tend to damp them out.
Fossil-Turbulence (non-overturning) $\varepsilon_o \geq \varepsilon$ and $\varepsilon_F \geq \varepsilon$	Remnant fluctuations in various hydrophysical fields which persist after the fluid is no longer actively turbulent on the scale of the fluctuation. Overturn eddy is damped out by both buoyancy and viscous forces.
Active+fossil-Turbulence (transition between Active and Fossil) $\varepsilon_o \geq \varepsilon \geq \varepsilon_F$	Remnant fluctuation in various hydrophysical fields which are actively turbulent at small scales but fossil-turbulence at large scales. Buoyancy forces are significant at large scale and inhibit the overturn.
Non-Turbulence $\varepsilon_F \geq \varepsilon \geq \varepsilon_o$	Fluid motions dominated by buoyancy and viscous forces, with no remnant microstructure from previous active-turbulence at any scale.
Turbulence at Fossilization $\varepsilon = \varepsilon_o$	Active-turbulence where the inertial forces of the largest eddies are just balanced by buoyancy forces of the ambient stable stratification.
Turbulence at Complete Fossilization $\varepsilon = \varepsilon_F$	Fossil turbulence where the inertial forces of the largest active turbulence eddies are just balanced by viscous forces
Buoyancy-Inertial-Viscous Transition $\varepsilon = \varepsilon_o = \varepsilon_F$	A unique state of stratified flow where buoyancy, inertial and viscous forces are all in balance.

1.5 Stages of Turbulent Patch Evolution

The evolution of a turbulent patch according to the Fossil Turbulence Theory can be summarized in the following steps. A shear layer will have instabilities that grow as waves (Stage 1). These waves grow into billows and will later collapse into patches of turbulence. These turbulent patches maintain the scale of the billows, while at the same time there is a cascade of energy to smaller scales as the overturns collapse into turbulent motions (Stage 2). Kinetic structures dissipate (kinetic energy converts to internal energy) and further collapse into micro-scales while the scalar variance retains the scale of the billows. In this stage, the large scale is fossilized while the small scale continues to overturn (Stage 3). Eventually the kinetic structures vanish, leaving only the scalar microstructure as a remnant of the turbulence (Stage 4) and the patch has become completely fossilized.

Stage 1. Shear instability to small disturbances

A shear layer (mixing layer) may become turbulent if the gradient Richardson number (*Ri*) falls below the critical value of 0.25 [*Itsweire et al.,* 1993]. Shear instabilities are generated as unstable internal waves develop Kelvin-Helmholtz (K-H) instabilities that grow in amplitude and eventually become turbulent, producing turbulent billows. When *Ri* of the flow, defined as the squared ratio of the ambient buoyancy frequency to the ambient velocity shear, falls below a critical value of 0.25, the K-H instabilities will grow, break, and overturn to produce K-H billows. *Ri* physically represents the ratio between potential energy (PE) and kinetic energy (KE). Its value reduces with a decreasing PE (either due to mixing or patch growth) or an increasing KE (due to excitation of fluid motion). KE grows in time if *Ri* is less than the critical value (0.25) and decays if $Ri > 0.25$ [*Itsweire et al.,* 1993].

As the billow entrains fluid and grows in time, the velocity shear and stratification change and result in the reduction of the gradient Richardson number across the patch. Assuming a billow is generated between two layers having a fixed

density difference $\Delta\rho$ and velocity difference ΔU then the bulk Richardson Number is given by $Ri_B = \frac{g}{\rho}\frac{\Delta\rho}{\Delta U^2}H$, where H is the thickness of the mixing layer, g is 9.81m/s^2, and ρ is ambient density. Assuming ΔU *and* $\Delta\rho$ are constant across the patch, then H is proportional to Ri_B. Therefore, value of Ri_B increases and TKE production reduces as the patch grows.

Stage 2. Fossilization Begins: Billows grow in scale until they are arrested by the stratification.

The K-H billows grow in Stage 1 until they reach the maximum scale allowed by buoyancy forces and will be arrested by the stratification signaling transition to Stage 2. When the eddies reach the Ozmidov scale ($L_O = (\varepsilon/N^3)^{1/2}$), the density they are trying to overturn is no longer passive but begins to overwhelm their inertial-vortex forces. The eddies then fail to overturn and start to collapse. The collapse of billows promotes small scale turbulence and local mixing, leading to gradual homogenization of the patch. As a result, the value of *Ri* increases because of the smearing of the local density and velocity gradients, and there will be no further energy transfer to the overturning billows at the large scales.

This is the beginning of the fossilization process. On the Hydrodynamic Phase Diagram (HPD), it is indicated by the $(\varepsilon/\varepsilon_O)^{1/3} = 1$ line, where ε_O is the dissipation rate at the beginning of fossilization [*Gibson*, 1980]. The mean Ozmidov scale for RASP 2004 patches is 0.72 m with a time scale of 96 s.

Stage 3. Active + Fossil Patches: Kinetic structure breaks down; scalar structures remain

At this stage, the kinetic structure of the overturn will collapse and break down into smaller turbulent patches. The approximate time scale for the kinetic structure to be completely dissipated is given by $T_{diss} = ({L_P}^2/\varepsilon)^{1/3}$, where L_P is the vertical length scale of the active+fossil patch. For RASP 2004, the mean active+fossil patch size is L_P = 2.07 m with mean dissipation rate of 6.56 x 10^{-8} W/kg. Hence, the mean time scale for

the kinetic structures to dissipate is 403 s (~7 minutes). After that, the patch will be completely fossilized and the mixing process will be completed by diffusion. Fossilization progresses from the largest scales to smaller scales. In this stage, structures with smaller scales continue to overturn until their scales are fossilized. The eddies in this stage are referred to as "active+fossil turbulence" [*Gibson*, 1980] to emphasize the transition between active and fossil stages. The eddies are being fossilized at the largest scales but still overturn at smaller scales.

As the kinetic structures break down and decay, the temperature structure (or other scalar fluctuations) does not collapse but retains the maximum Thorpe overturn scale of the former billow. The kinetic overturn scales become smaller than temperature overturn scales. Temperature overturn scales of the fossil preserve the overturn scale of the turbulence when fossilization begins (Stage 2). This is referred to as the fossil temperature turbulence to characterize it as the remnants from the beginning of the turbulent event.

Stage 4. Complete Fossilization: Kinetic structures have dissipated; scalar structures undergo diffusion

The eddies will continue to dissipate until the dissipation rate ε reaches $\varepsilon_F = 30\nu N^2$, where N is buoyancy frequency. [*Gibson*, 1980]. This is represented by the $(\varepsilon/\varepsilon_F) = 1$ line on HPDs. The inertial-vortex forces in the eddies of this stage are not able to overcome the viscous forces to overturn. Although the kinetic structures have dissipated, the scalar variance persist as fossil remnants. Eddies at this stage are referred to as fossils.

The difference between the molecular viscosity and molecular diffusivity is critical in retaining microstructure in the scalar field after the small eddies have stopped overturning. The small eddies driving the cascade are weakened by molecular viscosity, while the temperature gradients are smoothed by molecular diffusivity. The ratio of viscosity to thermal diffusivity is the Prandtl number, which has a value of ~7 for

seawater. The Prandtl number for salinity is even larger because salt diffuses more weakly than heat. Thus, the variance can persist long after the kinetic structures are dissipated.

Once the patch becomes completely fossilized, the mixing process will be completed by diffusion of the localized scalar fluctuations within the patch. The time scale for diffusion (T_D) can be estimated from $T_D = (L_S)^2/D$, where L_S is the vertical length scale of the scalar gradients within the fossilized patch, and D is the molecular diffusivity. L_S is of the order of centimeters for the RASP. Note that the values of molecular diffusivity for temperature and salinity are 10^{-7} m^2/s and 10^{-9} m^2/s, respectively. Hence, it will take up to 10^5 s (~ 27 hrs) for the temperature gradient and 10^7 s (115 days) for the salinity gradient in the fossil patch to vanish by diffusion. Even the kinetic structure has long-since dissipated, the final step of the mixing process takes much longer to complete due to the slow progression of molecular diffusion.

It is important to note that all of these time scales are estimated by using mean length scales from each stage of the observation. Vertical profiling technique can only provide snapshots of the water column at the time of measurement. With a sinking velocity of 1 m/s, the profiler takes about 5 min to profile a 300 m water column. This translates to a minimum of 10 min gap between profiles. It is also unreasonable to assume that the profiler can measure the exact same water parcel twice in the dynamic marine environment. The same patch was not likely measured twice by successive profile casts. Therefore, it is unlikely that the entire evolution of an isolated patch can be observed by vertical profiling. The HPD can be used to understand the different mixing stages based on profile data (Figure 3). It was shown in laboratory studies that a turbulent patch follows a slope 1/3 decay line on the HPD as it evolves from active to fossil turbulence [*Gibson*, 1987a, 1991]. However, it is not logical to assume that any patches that lie on a slope 1/3 line are different stages of the same turbulent patch.

1.6 Motivation and Objective

The motivation behind this study is to better understand coastal mixing processes and buoyancy turbulence. The proposed research focuses on identifying and classifying turbulent patches in vertical microstructure profiles collected in coastal regions of Honolulu, Hawaii. The three major objectives of this study are: 1) Identify overturn patches from vertical microstructure density and temperature profiles; 2) Classify, quantify, and parameterize turbulent patches by the fundamental length scales (L_T, L_K, L_O) and the dimensionless numbers defined by their ratios (Fr_T *and* Re_T), and 3) Examine the Hydrodynamic Phase Diagrams (Fr_T versus Re_T diagrams) produced from the dataset to study the evolution of the turbulent events.

The data used for this research study were collected during the Remote Anthropogenic Sensing Program (RASP) in Honolulu, Hawaii. RASP is a collaborative effort between NOAA, the prime contractor Directed Technologies Inc. (DTI), and sub-contractors Isintech. The program aimed to 1) detect submerged ocean anthropogenic turbulence sources in the ocean by analyzing sea surface signatures obtained from multi-spectra satellite data [*Keeler et al.,* 2005], and 2) describe and understand the mechanisms of the energy transport from the submerged turbulence source to the sea surface. The Sand Island municipal wastewater outfall in Honolulu, Hawaii (Figure 5) provides a relatively steady source of submerged turbulence which is trapped by buoyancy forces of the stably stratified receiving waters in Mamala Bay [*Fischer et al.*, 1979].

The Sand Island outfall is designed with a 1040 m long diffuser section with 282 small jets that cause maximum initial dilution with dense bottom seawater. The diffuser section of the outfall is at 70 m depth on the sea floor and continuously discharges about 3.1 m^3/s of wastewater into the stratified ocean as a buoyant turbulent plume [*Roberts*, 1999]. The diffuser jets act as permanent sources of intensive turbulence in the stratified ocean water. Normally, ocean microstructure studies have highly uncertain initial conditions where it is very difficult to study the evolution of the stratified turbulence.

This study is the first application of modern microstructure instrumentation in a wastewater outfall so that the evolution of the buoyancy-driven, actively turbulent plume can be studied. The wastewater outfall represents a field laboratory to test stratified oceanic turbulence, mixing and diffusion processes with known and reproducible forcing and ambient hydrophysical conditions.

Different approaches were used in RASP throughout the years to accomplish specific goals. RASP 2003 measurements were made at stations spread across the region of interest in order to map out the anomaly region produced by physical properties generated by the diffuser jets. In 2004, measurement campaigns were designed to focus on turbulence and other hydrographic parameters at fixed stations in the anomaly and ambient regions (Figure 5). The time series data set is sufficiently large to identify possible systematic differences between the two regions, especially when such differences are small compared with the daily variability (e.g. tidal or meteorological conditions).

The microstructure instrument used in this study was Sea and Sun Technology GmbH (Trappenkamp, Germany) MicroStructure System (MSS). MSS is a multi-sensor system for the measurement of microstructure and turbulence. The installed sensors consist of high-resolution microstructure and turbulence sensors (temperature, velocity shear) and standard CTD sensors (temperature, electrical conductivity, pressure). The profilers used during the RASP experiment were additionally equipped with a combined light scattering/fluorescence sensor and a microstructure conductivity sensor. The data were transmitted on-line via electrical cable to the board unit, and further to a PC for data storage. The profiler's sinking velocity was adjusted to be approximately 1 m/s using a combination of weights and buoyancy elements. [*Prandke and Stips*, 1998a,b].

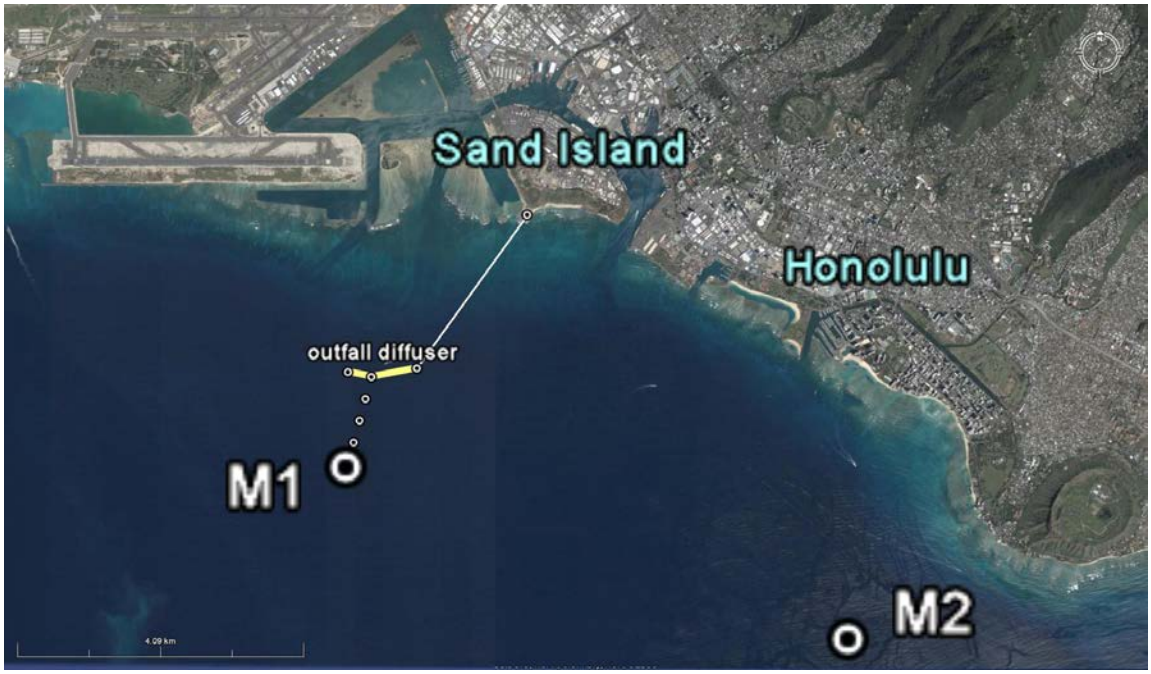

Figure 5. Location of Sand Island outfall diffuser and RASP 2004 microstructure measurement station at the area of anomaly (M1) and the area of ambient (M2).

1.7 Summary

The goal of this study is to understand buoyancy turbulence from the basic elements -- the overturn patches. The microstructure data collected during the Remote Anthropogenic Sensing Program (RASP) is an ideal candidate for Hydrodynamic Phase Diagram (HPD) studies. It consist of time series datasets from two coastal stations, one with only natural turbulence (wind forcing, bottom mixing, etc) and one with the addition of a man-made turbulence source (sewage outfall diffuser jets). By comparing the results from the HPDs with other physical parameters collected during the same period, the following questions can then be addressed:

1. What can be learned about the turbulent event by identifying and classifying the overturns patches?

2. How do overturn patches from a stratified mixing event differ from the ones generated by ambient mixing?

3. Does the observation from the coastal region resemble the growth of turbulent patches observed in laboratory [*Fernando,* 2003]?

4. What information can the HPDs provide regarding the hydrodynamic condition of the environment?

5. What can be concluded from the HPDs in terms of the phase of patch decay, and the source of turbulence in the region?

6. How do HPDs from a complete dataset compare to those with incomplete or limited dataset in past studies?

7. Is fossil turbulence significant to marine turbulence investigation, or is it a phenomenon that exists in disciplines of fluid dynamics other than oceanography?

Chapter II presents the field measurements, data processing, and analyzing methods from RASP. Parameters obtained from the ambient and anomaly stations are compared and discussed. The result shows how the coastal hydrography is affected by a submerged turbulence source. Chapter III discusses the identification of turbulent patches in microstructure measurements and the classification of their hydrodynamic phases with HPD. The technique of HPD will be examined with the RASP dataset. With HPDs, the phases of overturning can be identified, allowing detailed descriptions of the mixing processes. Chapter IV provides a conclusion to this study and recommendations for future research.

CHAPTER II
MICROSTRUCTURE FIELD MEASUREMENTS

2.1 Background

Astronauts have long noticed that they could see deep ocean bottom features from orbit. To test a claim that submerged turbulence, internal waves, and bottom topography can be observed from the orbit, a series of experiments were organized and became the Remote Anthropogenic Sensing Program (RASP).

RASP was a five year effort (2001-2005) to examine subsurface phenomena related to a sewage outfall off the coast of Oahu, Hawaii. The program consisted of space-based remote monitoring and *in-situ* sea truth measurements of the Mamala Bay region. It is the first study to use a municipal outfall as a source submerged of turbulence to understand the hydrophysical characteristics of mixing events in the ocean environment. The result demonstrated the feasibility of remotely detecting sewage outfall manifestations on the surface and in the near surface water layers.

RASP was a collaborative effort between NOAA, the prime contractor Directed Technologies Inc., sub-contractor Isintech, Scripps Institution of Oceanography, and NAVAIR. Satellite imagery and sea truth measurements were carried out simultaneously between 2002 and 2004. Optical and multispectral satellites used in the experiments included Ikonos, QuickBird, QuickSCAT, and GOES. The complete ensemble of multi-

sensor imagery was processed and analyzed by Academician Valergy G. Bondur and his team. The result was then compared with data collected from five oceanographic vessels during the same period. By using proprietary algorithms and methods, Bondur and his team revealed measureable surface wave pattern anomalies that appeared to correlate with the outfall. It was possible to infer the presence of high-frequency internal waves radiating to the southeast and southwest using remote imaging in the region of interest. The sea truth measurements appeared to be consistent with the presence of residual turbulence and internal waves originating from the vicinity of the outfall. Thus, the comparison of the satellite and sea truth data confirmed the possibility of detecting both surface and near-surface anomalies through satellite imagery.

Figure 6 shows an analysis of a typical space image fragment. It was obtained on September 2nd, 2002 by the Ikonos satellite using optical cameras. The satellite cameras took images of an 11 km wide ocean area extending 50 km south-southwest of Oahu. The satellite orbit was sun synchronous at an altitude of 680 km. Image spatial resolution was approximately 1 m in the panchromatic mode. The obtained satellite images were processed using a spatial-frequency spectrometry method [*Bondur*, 2000, 2004]. This method involves 2-D Fourier transformation and specific analysis of the 2-D spatial spectra to allow remote detection of subsurface hydrodynamic processes [*Bondur and Grebeniuk*, 2001]. The technique is based on registration of slight changes of short (<1 m) wind-driven-waves revealed by anomalous image brightness spectra different from surrounding background areas.

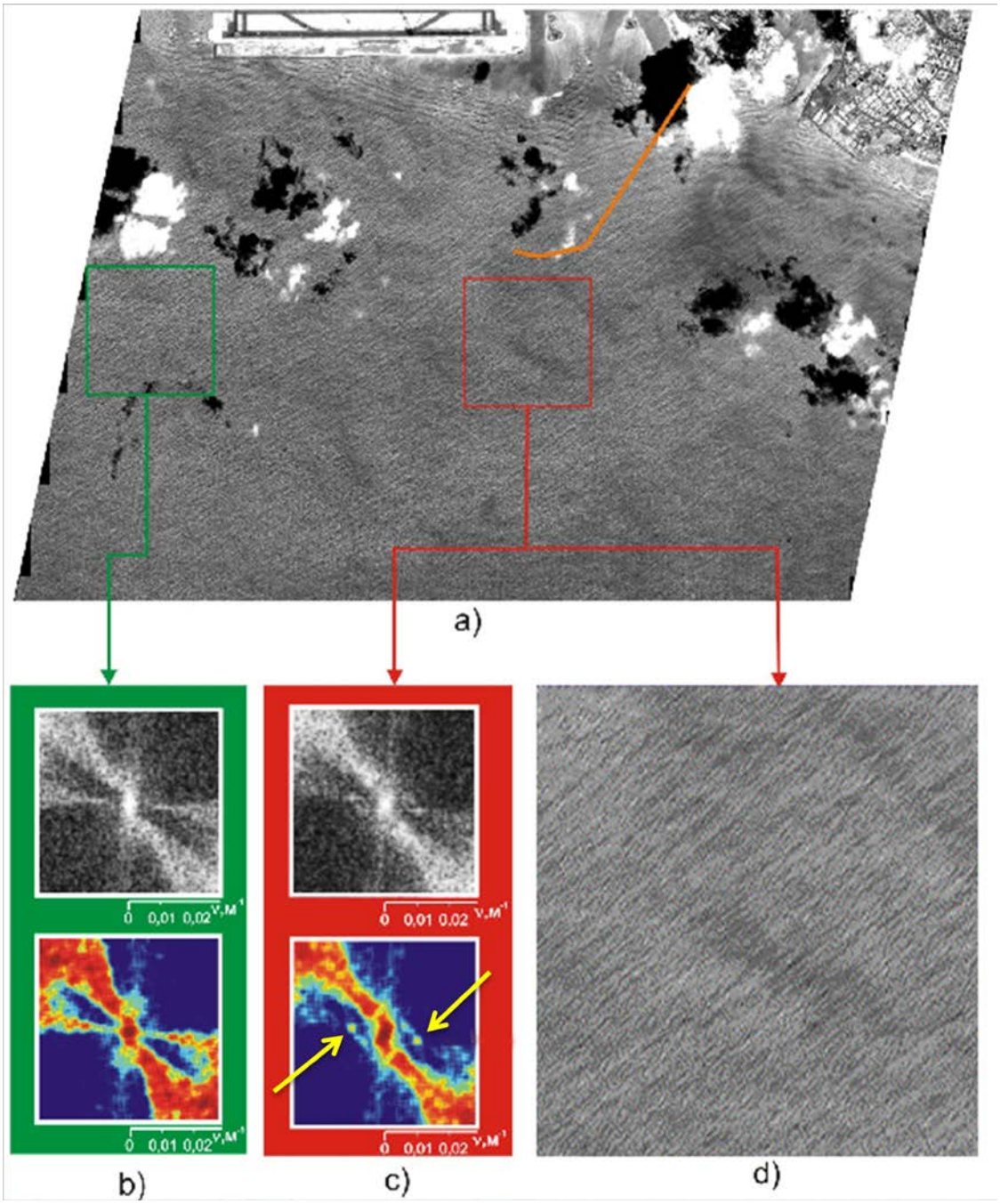

Figure 6. Fragment of Mamala Bay (Honolulu, Hawaii) Ikonos image taken on September 2nd, 2002 with marked location of the (a) outfall pipe (orange line), (b) background area (green box), and (c) outfall area (red box). Figure 5c and 5d are the processed and original image of the same fragment. The two narrow-band spectral maxima are indicated by the yellow arrows in Figure 6c. [*Bondur*, 2004].

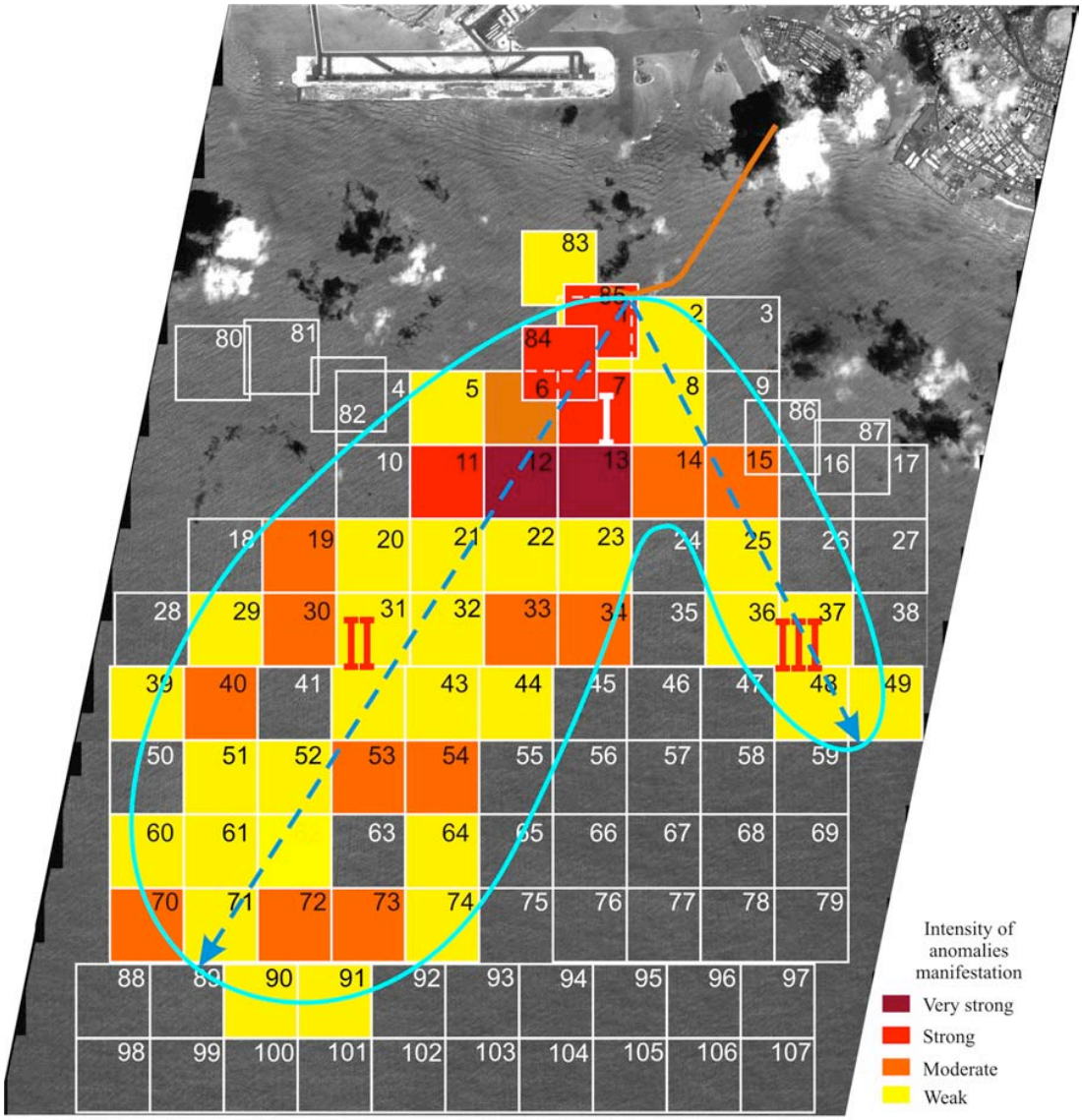

Figure 7. Spatial distribution of anomalous spectral brightness caused by submerged outfall turbulence in 1 km areas of the Ikonos image taken on September 2nd, 2002 [*Bondur and Filatov*, 2003].

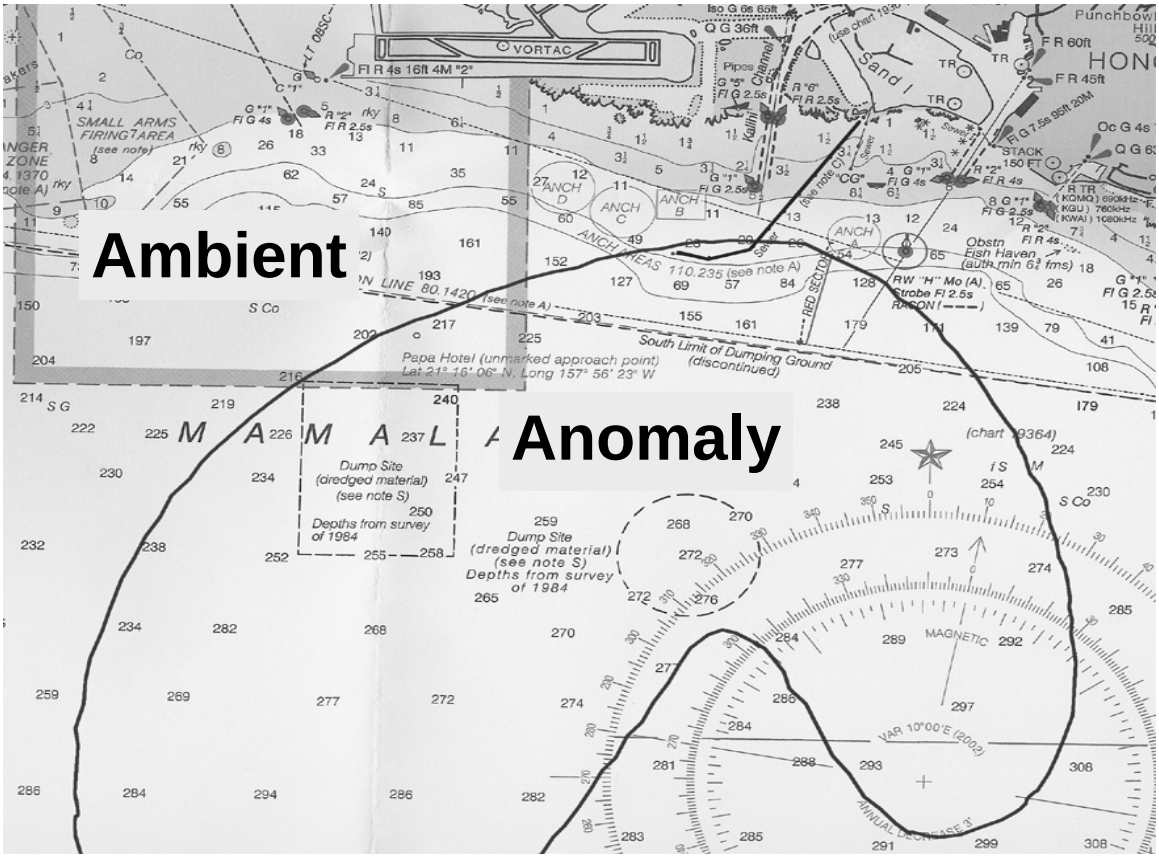

Figure 8. The "anomaly" and "ambient" regions as defined for RASP based on processed satellite images similar to Figure 7.

Figure 6b shows a 2-D spectrum for a background area of ocean surface approximately 5 km west of the diffuser for unaffected surface waves. Figure 6c shows the spectrum for an anomalous spectral region just south of the diffuser, with two narrow-band (quasi-coherent) spectral maxima that were not shown in Figure 6b. These two maxima are the detected surface manifestations of the submerged outfall. The wavelength of the spectral harmonic is approximately 93m. An enlarged pre-processed fragment of the area is given in Figure 6d and only the northwestern surface swell can be seen. The region with surface anomaly can then be outlined by combining the results from each processed fragment (Figure 7). Hereafter, the "anomaly region" will be defined as the area with observed surface anomalies from the satellite imagery analysis,

whereas the “ambient region” will be defined as the rest of the sea surface where no anomalies are observed (Figure 8).

This chapter focuses on the sea truth data collected in 2004 and investigates the sewage outfall's influence on the nearby hydrographical conditions. Satellite imagery and remote sensing aspects of RASP are not the subject of this study and can be found in other publications [e.g. *Bondur*, 2005].

2.2 Instrumentation

The MicroStructure System (MSS) is a multi-parameter system used to measure physical microstructures and turbulence in marine and limnic waters [*Prandke and Stips*, 1998a,b; *Baumert et al.*, 2005]. The complete system consists of the following components: 1) MSS profiler with CTD and microstructure sensors, 2) probe interface with parallel port for data transmission to PC, 3) PC or laptop for data acquisition, 4) high speed data acquisition software, and 5) portable ship winch SWM2000 (Figure 9). The standard sensors installed on the profiler include microstructure temperature, microstructure conductivity, shear velocity sensors, and standard CTD sensor package (i.e. temperature, conductivity, and pressure sensors). The profilers used during the RASP experiments also included light scattering (turbidity) sensors. To monitor disturbances caused by vibration of the profiler, an accelerometer is used to measure horizontal acceleration of the profiler housing. The complete sensor equipment package is summarized in Table 2. The data are transmitted real-time via electrical cable to the board unit and is transferred to a laptop for data storage.

The principle of the shear measurements is the detection of the lift forces added to an airfoil. The axis of the airfoil is aligned with the vertical sinking velocity. While the sensor is not sensitive to axial forces, cross forces are detected by a piezo-ceramic bending element connected with the airfoil. The voltage output of the piezo-ceramic beam is proportional to the lift force at the airfoil. The lift forces due to turbulent

velocity fluctuations are transmitted via a centilever to the piezo-ceramic bending element, which is recessed and sealed into the titanium cap [*Prandke*, 1994].

Figure 9. MSS-90 profiler and SWM2000 operational winch system during RASP measurement campaign.

Table 2. Summary of the sensor package installed on MSS profiler during RASP measurement campaign.

Sensors	Principle	Range	Accuracy	Resolution	Time
Velocity Shear	airfoil lift force measurement	0 - 6 s^{-1} (Dissipation rate 10^{-2} -10^{-11} W/kg)	not specified	App. 10^{-3} 1/s	3 ms
Micro-temperature	FP-07	-2...+38°C	+/- 0.02°C	0.002°C	10 ms
Micro-conductivity	2 electrode capillary system	0…60 mS/cm	Not specified	0.002mS/cm	3 ms
Pressure	piezo-resistive	50 Bar	+/- 0.1%fs	0.002%fs	30 ms
Precision Temperature	Pt 100	-2 - +38°C	+/- 0.01°C	0.001°C	150 ms at 1 m/s
Precision Conductivity	7-pole-cell	0 - 60 mS/cm	+/- 0.02 mS/cm	0.001 mS/cm	50 ms at 1 m/s
Acceleration	Inertial mass	-1 - +1 m/s^2	0.02 m/s^2	0.005 m/s^2	3 ms
Turbidity	light scattering blue light	0- 200 ppm	1 ppm	$5x10^{-4}$ ppm	3 ms
Fluorescence	fluorescence backscatter	0 - 200 ppb	0.5 ppb	$5x10^{-3}$ ppb	3 ms

The sensitive element of the micro-temperature sensor is a glass coated micro-thermistor type FP07. The sensor consists of a glass-coated thermistor hermetically sealed at the tip of a shock-resistant 12.5 mm long glass rod of diameter 2.1 mm. The glass rod thermistor is affixed with an adhesive into the end of a slim titanium shaft. To protect the glass tip of the sensor, a guard is mounted to the tip of the sensor [*Gloor*, 1995].

The microstructure conductivity sensor consists of a two-electrode probe. This type of conductivity sensor is based on developments of the Atlantis Branch of the P.P. Shirshov Institute of Oceanography [*Paka et al.*, 1999]. The inner electrode in the conic sensor tip is a capillary tube with a diameter of 1 mm. The outer electrode is the surface of the cylindrical sensor. Both electrodes are made from stainless steel. The contact surface between the inner electrode and the water is approximately 0.6 cm^2. This guarantees a low current density at the electrode surface and consequently, a low level of contact polarization noise. The spatial response of the sensor is 5 mm, approximately 5 times the capillary tube diameter [*Gibson and Swartz*, 1963].

The MSS profiler has a hydro-dynamically smooth cylindrical housing to reduce inherent vibrations resulting from the turbulent eddies that are formed at sharp edges. The profiler's sinking velocity has been adjusted by a combination of weights and buoyancy elements to be around 1 m/s. Microstructure sensors are placed at slim shafts approximately 15 cm ahead of other sensors and in the free flow region ahead of the instrument (Figure 10). This arrangement ensures undisturbed measurements of the microstructures of water stratification and velocity shear. High resolution temperature and shear sensors are the major sensors used for small scale turbulence measurements during RASP.

Two tethered free-falling MicroStructure System (MSS) profilers were used in RASP. They provide standard CTD parameters plus microstructure parameters (temperature gradient, velocity shear, micro-conductivity, turbidity, and fluorescence). Details of the MSS profilers can be found in *Prandke and Stips* [1998a,b]. Information on MSS data processing methodology can be found in *Kocsis et. al*. [1999].

The winch is specially-designed to operate free-sinking microstructure probes. It is mounted at the ship's bulwark and can be oriented in any direction. The cable goes directly from the drum into the water. The winch is controlled via a handheld unit with buttons for up, down, and speed control. A special cable is used to enable the MSS profiler to sink freely without feeling the influence of the deployment tether. The sinking properties of the cable are adjusted to the typical sinking velocity of the MSS. It has aramid strength members, giving it a breaking strength of approximately 1,900 N.

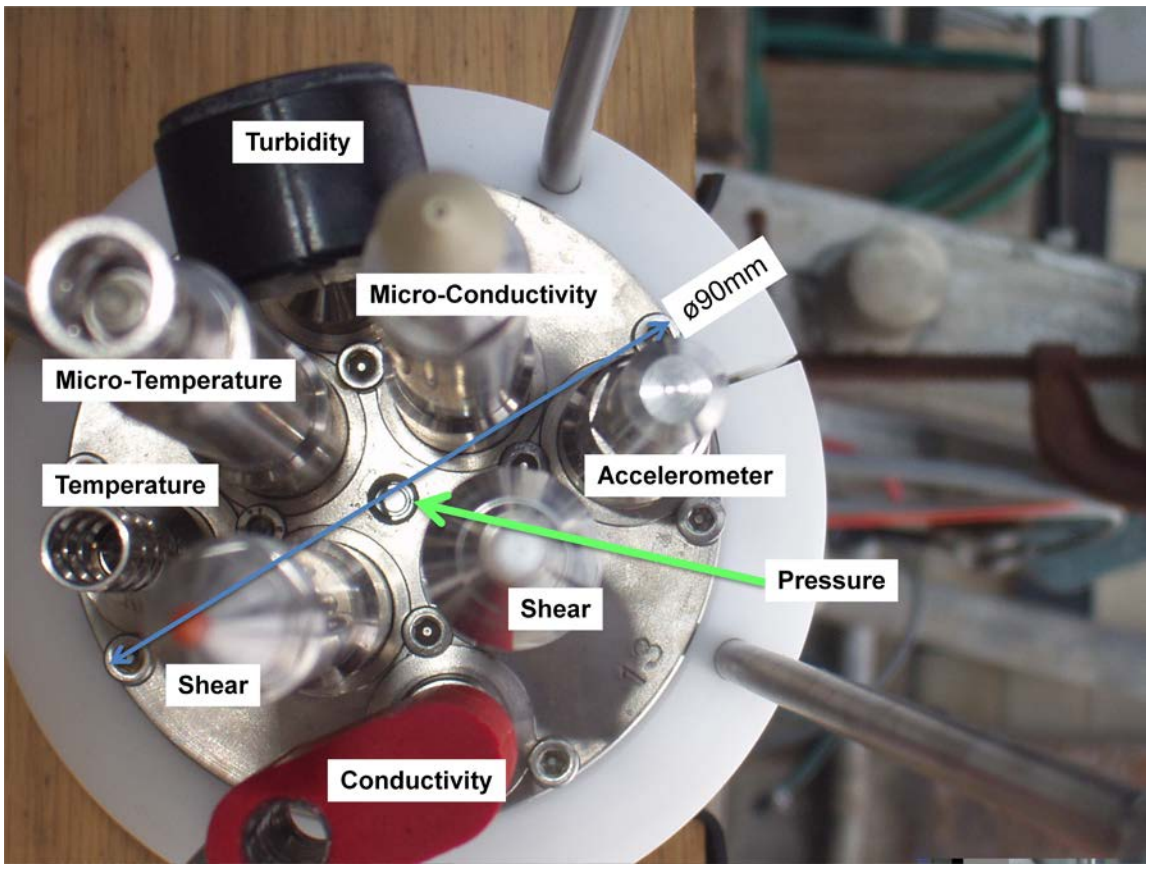

Figure 10. Front view of the sensor package installed on MSS profiler including two shear probes, micro-temperature, micro-conductivity, accurate-temperature, accurate-conductivity, acceleration, turbidity, and depth sensors.

The MSS profiler is deployed from a drifting ship with the ‘slack-tether’ method. As the profiler descends, the tether cable is paid out from the winch at a rate that is slightly faster than the separation of the profiler and the ship. This ensures that the profiler descends monotonically and vibrations from the tether line are minimal. The profiler descends at an approximated rate of 0.8 m/s. MSS profilers were deployed from a work boat (Figure 11), which provided an adequate platform for coastal profiling.

Figure 11. Workboat used for RASP microstructure measurements and drogues deployments.

2.3 Measurement Strategies and Locations

Sand Island is located off the south coast of Oahu Island in the Hawaiian Archipelago. The upgraded diffuser section was completed in 1975. The diffuser, located at depth of approximately 72 m, is 1030 m long with 282 small jets that cause an

initial dilution with denser bottom seawater. The pipe has an inner diameter of 2.13 m. It continuously discharges approximately 3 m^3/s of primary treated sewage into the stratified ocean as a buoyant turbulent plume [*Roberts*, 1999]. The rising plume mixes with the ambient ocean water until the diluted effluent reaches a trapping depth below the surface where its density matches that of the stratified receiving water [*Koh et al.*,1975]. In most cases, the lighter effluent rises above the diffuser and is trapped in the thermocline at depth of approximately 30 m to 50 m with dilution on the order of 100. However, a combination of density stratification, tides and effluent flow rate can lead to conditions where a portion of the effluent reaches the sea surface [*Roberts*, 1999]. When the plume surfaces, the range of dilution is between 300 and 1000, depends on the flow rate. Design philosophy and other details of the Sand Island outfall can be found in *Fischer* [1979]. The diffuser act as permanent sources of intensive turbulence in the stratified ocean water and is an ideal location for ocean turbulence studies.

During the early planning stage of RASP, it was hypothesized that the surface manifestation was caused by extreme abnormalities (such as larger than normal turbulent kinetic energy dissipation, or significant levels of turbidity). Hence, the RASP 2002 and 2003 measurement campaigns were designed to provide quick-scans of the area by obtaining a larger number of vertical profiles over the entire anomaly region (Figure 12) in hope of capturing the extreme conditions. Vertical profiles were collected all over the anomaly region while only a few profiles were obtained in the ambient region. Each station was profiled twice, and it took over several weeks to cover the entire anomaly area. Unfortunately, after analyzing the 2002 and 2003 field data, it is concluded that no extreme abnormalities could be found. Furthermore, the data collected from this exploratory approach contains too much spatial and temporal variation and cannot be used for meaningful statistical comparison between the two regions.

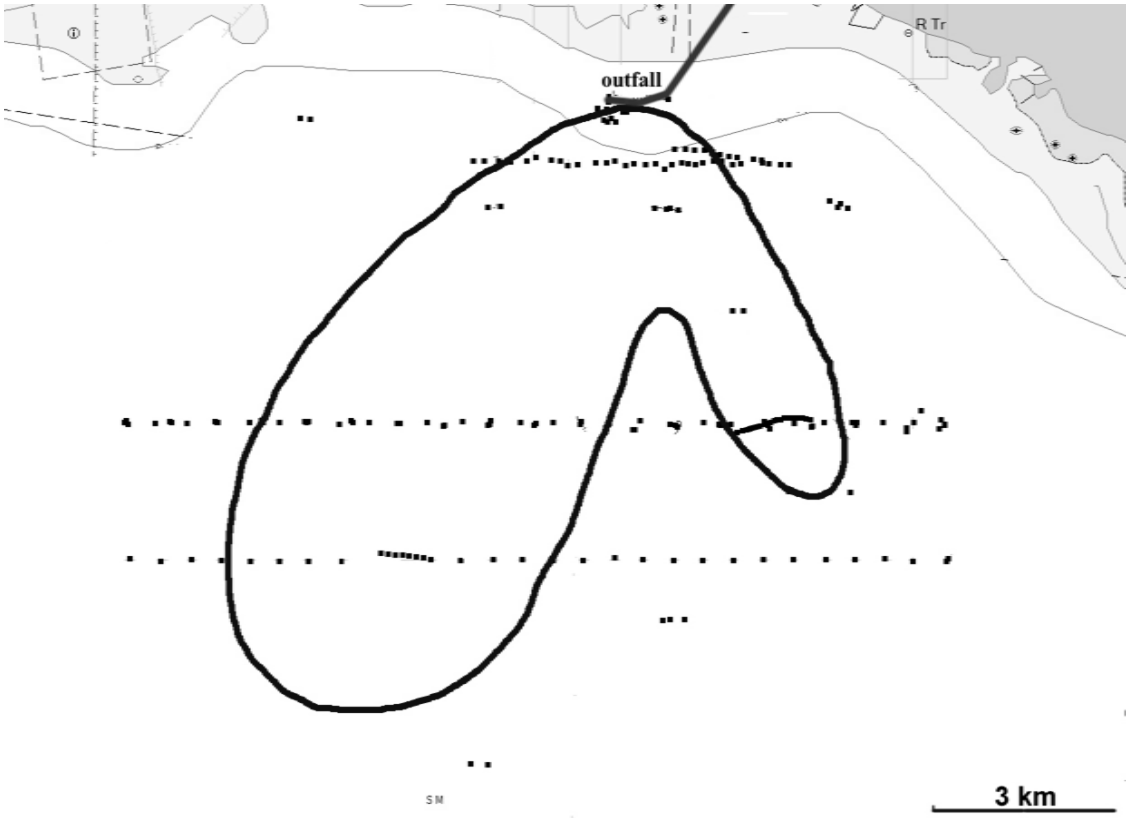

Figure 12. Location of microstructure profiles obtained during RASP 2002 and 2003 (black dots). Most of the microstructure data were collected in the core area of surface anomalies (outlined area).

With the lessons learned, the 2004 measurement campaign was designed as a controlled experiment in which the time series data measured from the experimental station were compared against data from the control station. The control station was selected to be nearly identical to the experimental station except for the existence of the submerged turbulence source which is the effect being tested. Hence, the anomaly station (M1) is the experimental station and the ambient station (M2) is the control station of this experiment (Figure 13). The bathymetrical, hydrographical, and meteorological features were carefully studied in order to select the most suitable locations. Time series data that represent the parameters over a long period of time were

collected and both stations were repeatedly measured on a regular basis within the field measurement period. Measurements were carried out at alternating stations and over different phases of the diurnal tidal cycle to minimize bias introduced by hydrographical (tidal currents) and meteorological (local wind speed, rain) conditions.

Locations of the anomaly (M1) and ambient (M2) stations were selected based on the processed satellite images with surface anomaly identified from August 13 and August 16, 2004. M1 (21.268N 157.909W) is located in the core of the anomaly, whereas M2 (21.246N 157.839W) is outside of surface manifestation. Both stations have a water depth of approximately 370 m and similar bottom topographies (Figure 14). They both are located at the deep end of a slope extending from the shoreline. However, M2 has a 21^{o} slope which is steeper than the 14^{o} slope at M1. The steeper bottom slope is likely to result in intensified bottom boundary mixing and must be taken into consideration when comparing the results.

Alford et al. [2006] provides a detailed study of the hydrographical and mixing conditions of the region. That study is based on the data collected from the Hawaiian Ocean Mixing Experiment (HOME) conducted in the summer of 2004. The data show no significant differences in mean fluxes or overall dissipation rates between M1 and M2. In addition, no remarkable difference can be found between the mean temperature, mean density, and mean salinity vertical profiles at both stations (Figure 15 to Figure 17). There are small differences between the vertical buoyancy frequency profiles, including a double peak in the seasonal pycnocline at M2, but the maximum values are almost the same (Figure 18). It can be concluded that the hydrographical condition of both stations are nearly identical and any differences would not significantly affect data.

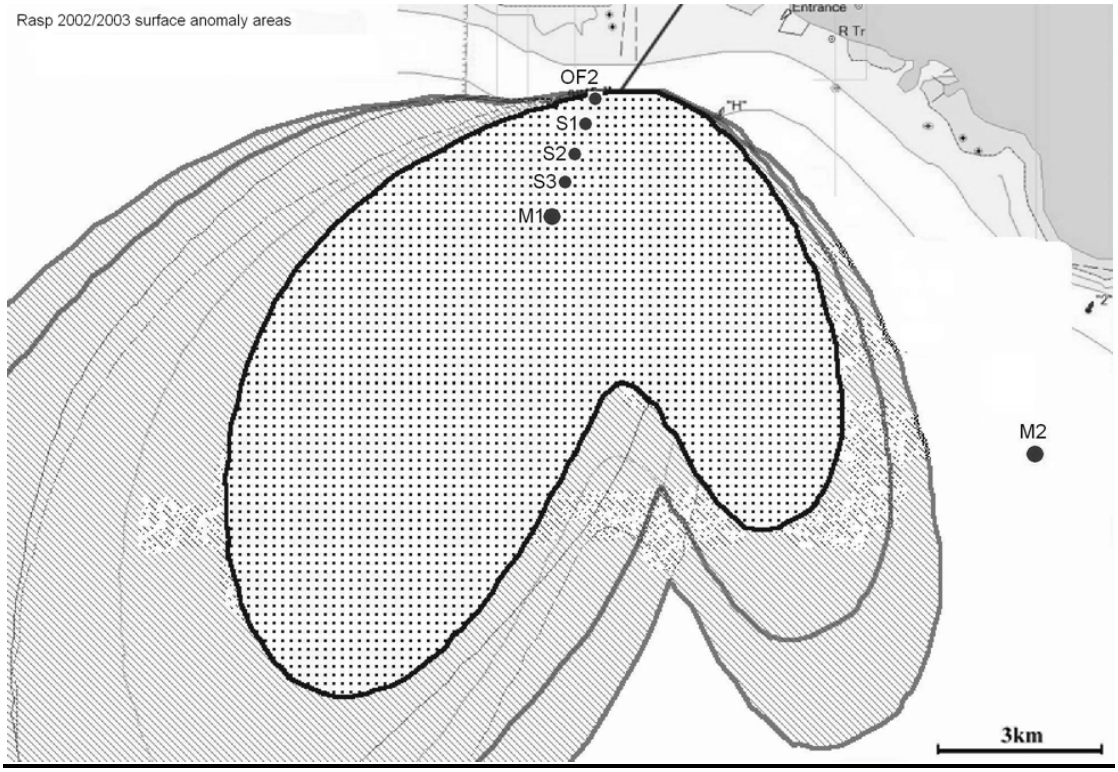

Figure 13. Location of measurement stations in RASP 2004. Station M1 is the representative station for the "anomaly" area, Station M2, located outside of the "anomaly" area, is the reference station for the "ambient" area. The advection of the plume water into the "anomaly" area was measured along the section from station OF2 (center of the outfall) to the station M1. For comparison, surface anomalies observed on different satellite images (similar to Figure 7) are outlined with different shapes and shades.

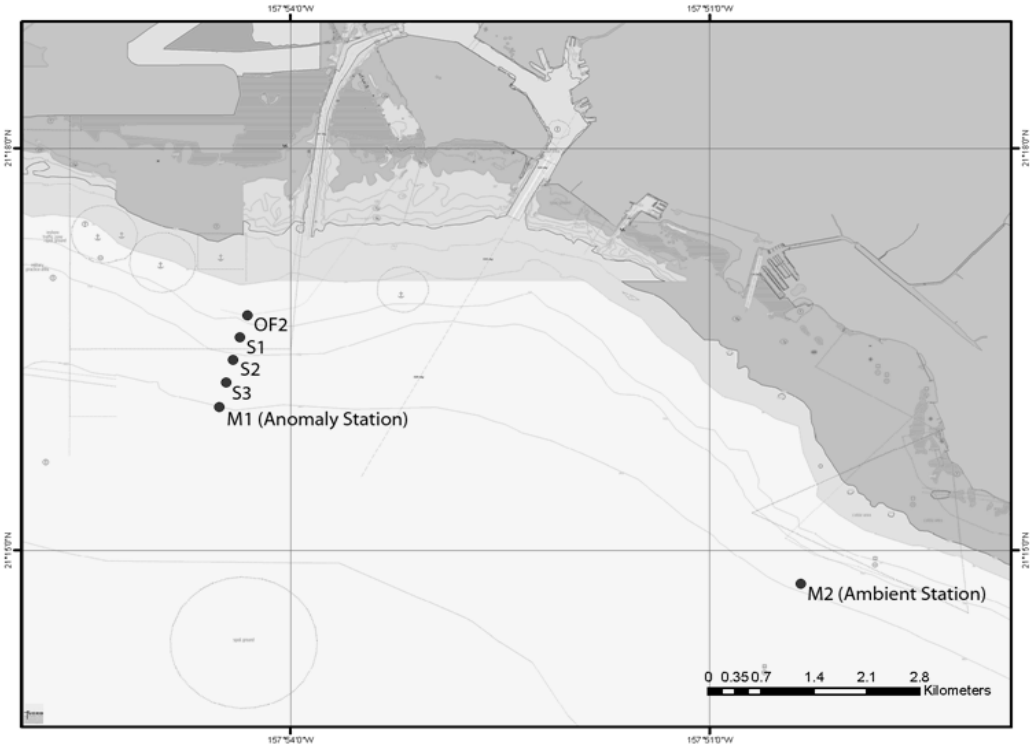

Figure 14. Bathymetry at the stations M1 and M2. Both stations are located on the same isobath (~350m), but the slope is steeper at M2.

Wind data were collected by the vessel's onboard metrological sensors during the measurement campaign. Average wind speeds of the stations are summarized in Table 3. During the measurement period, average wind speed was significantly higher at the ambient station (M2) than at the anomaly station (M1). This is due to the geographical location of M2 at the margin of Mamala Bay and exposed to the eastern and western wind, whereas M1 is sheltered by the bay. Because the production of turbulent kinetic energy (TKE) on the ocean surface is proportional to U^2, where U is the wind speed, it can be assumed that the TKE production at M2 is larger than at M1 by a factor of 1.60 (Table 3). It can be also expected that the upper water column turbulent intensity at M2 to be higher than at M1 by the same amount.

Table 3. Mean wind speed during MSS measurements at stations M1 and M2. The mean wind speed at M2 was significantly higher than at M1.

Area	Mean Wind Speed U [m/s]	95% confidence interval [m/s]	U^2 relative to the anomaly station
Station M1 (Anomaly)	6.35	5.80 - 6.72	1
Station M2 (Ambient)	7.93	7.65 - 8.21	1.60

In summary, the hydrographical conditions of the anomaly station (M1) and the ambient station (M2) are nearly identical. Their stratification structures are similar and no statistical differences in horizontal fluxes and overall mixing conditions can be found. Consequently, no significant difference in turbulence properties should be expected. This supports the choice of M2 as the control station for this field experiment. However, it is necessary to take into account the difference in the bottom slope and average wind speed. Although both stations have same water depth, M2's steeper slope could result in a higher turbulent dissipation rate at the bottom boundary layer. The stronger wind experienced at M2 could also result in higher dissipation rate in the upper water column due to the penetration of wind stress effects.

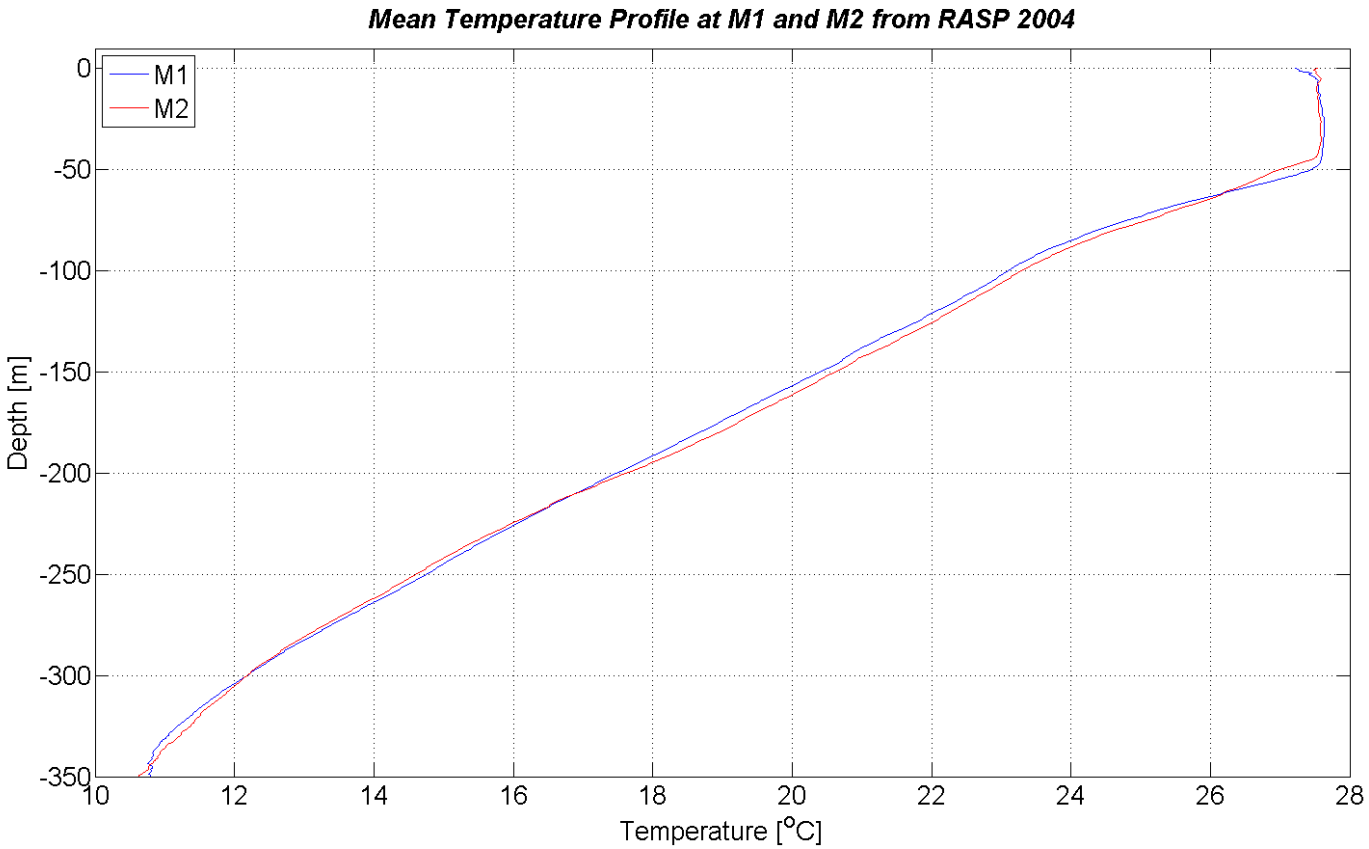

Figure 15. Mean vertical temperature profiles of the Anomaly Station M1 (blue) and the Ambient Station M2 (red).

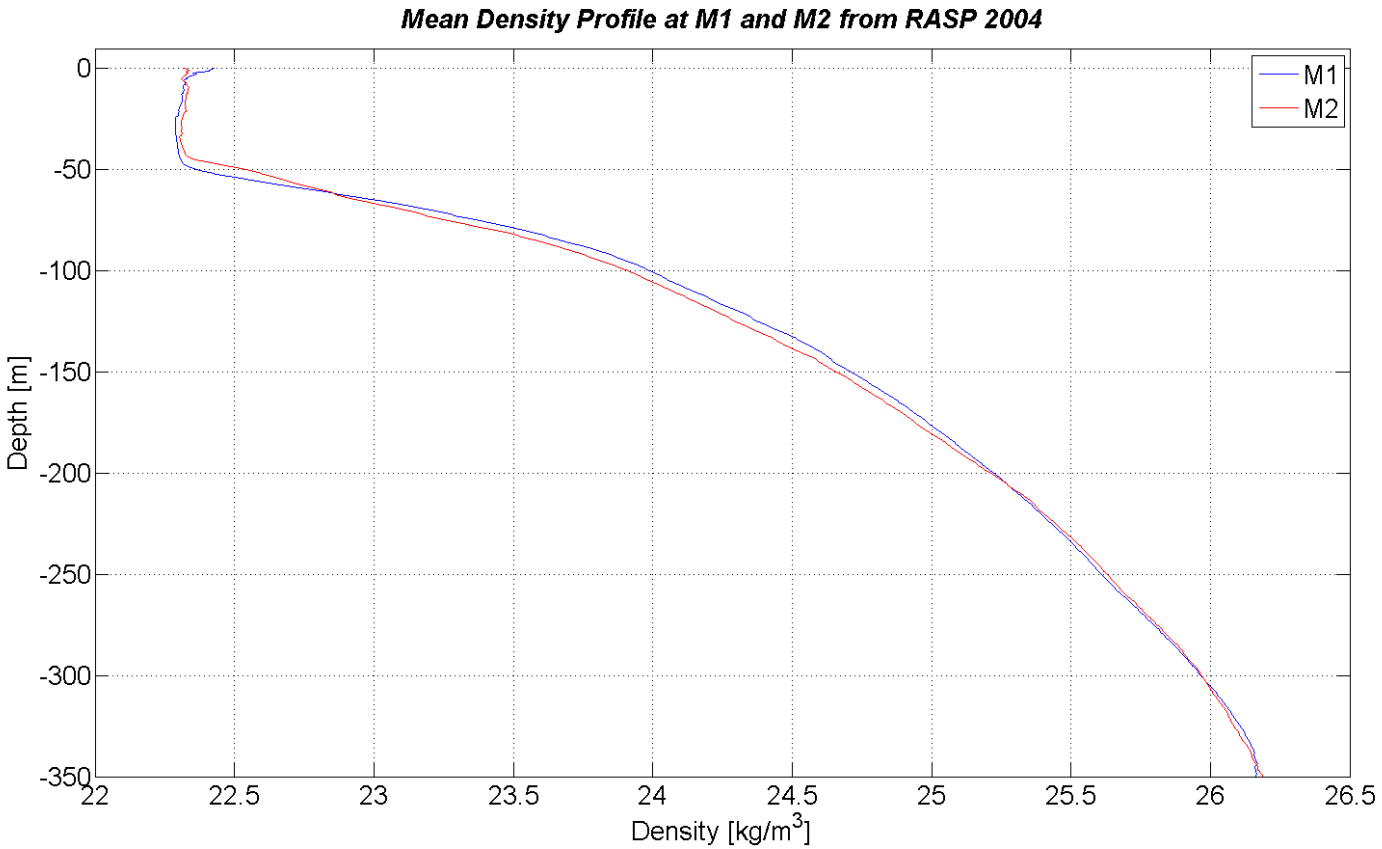

Figure 16. Mean vertical density profiles of Anomaly Station M1 (blue) and the Ambient Station M2 (red).

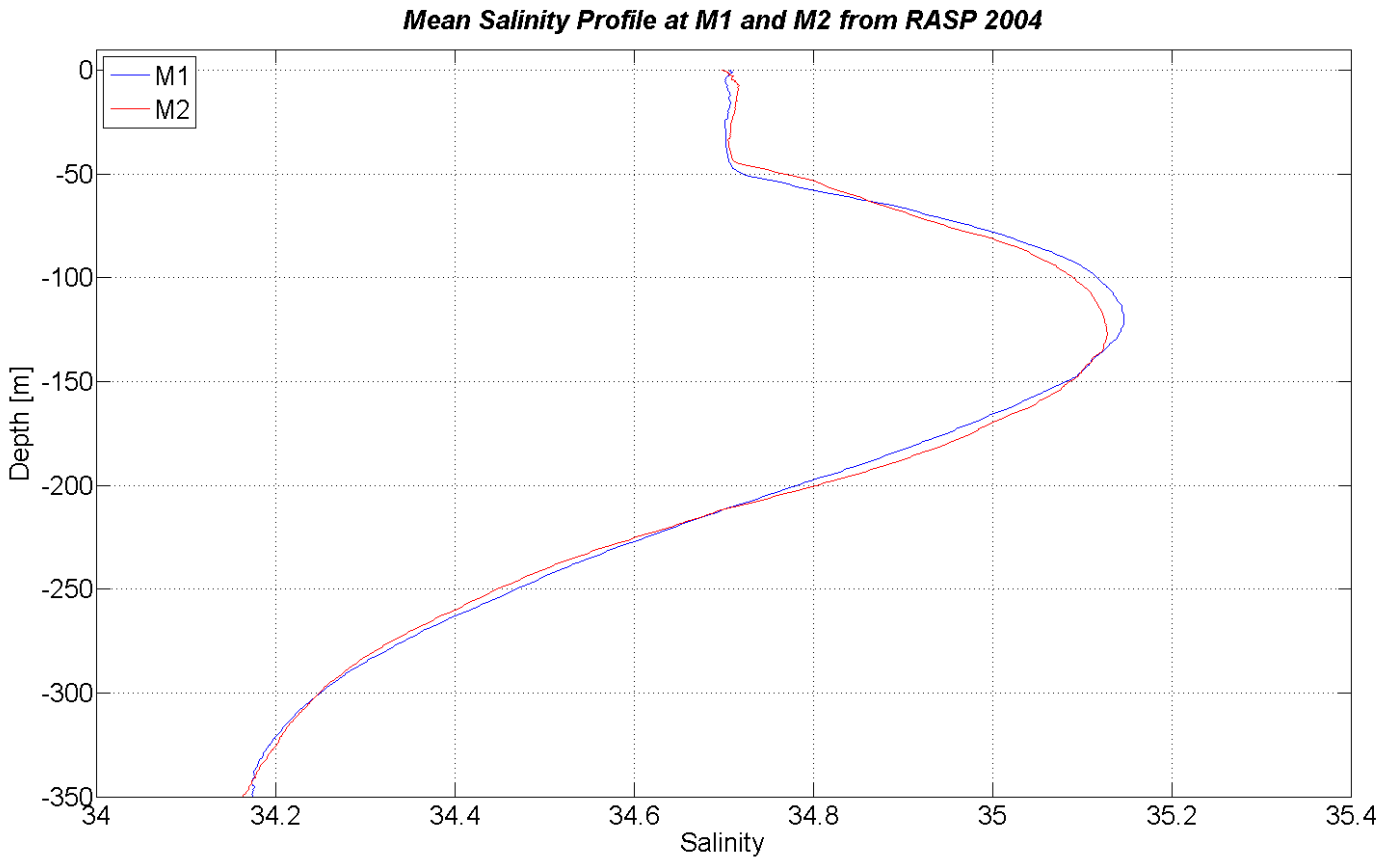

Figure 17. Mean vertical salinity profiles from Anomaly Station M1 (blue) and the Ambient Station M2 (red).

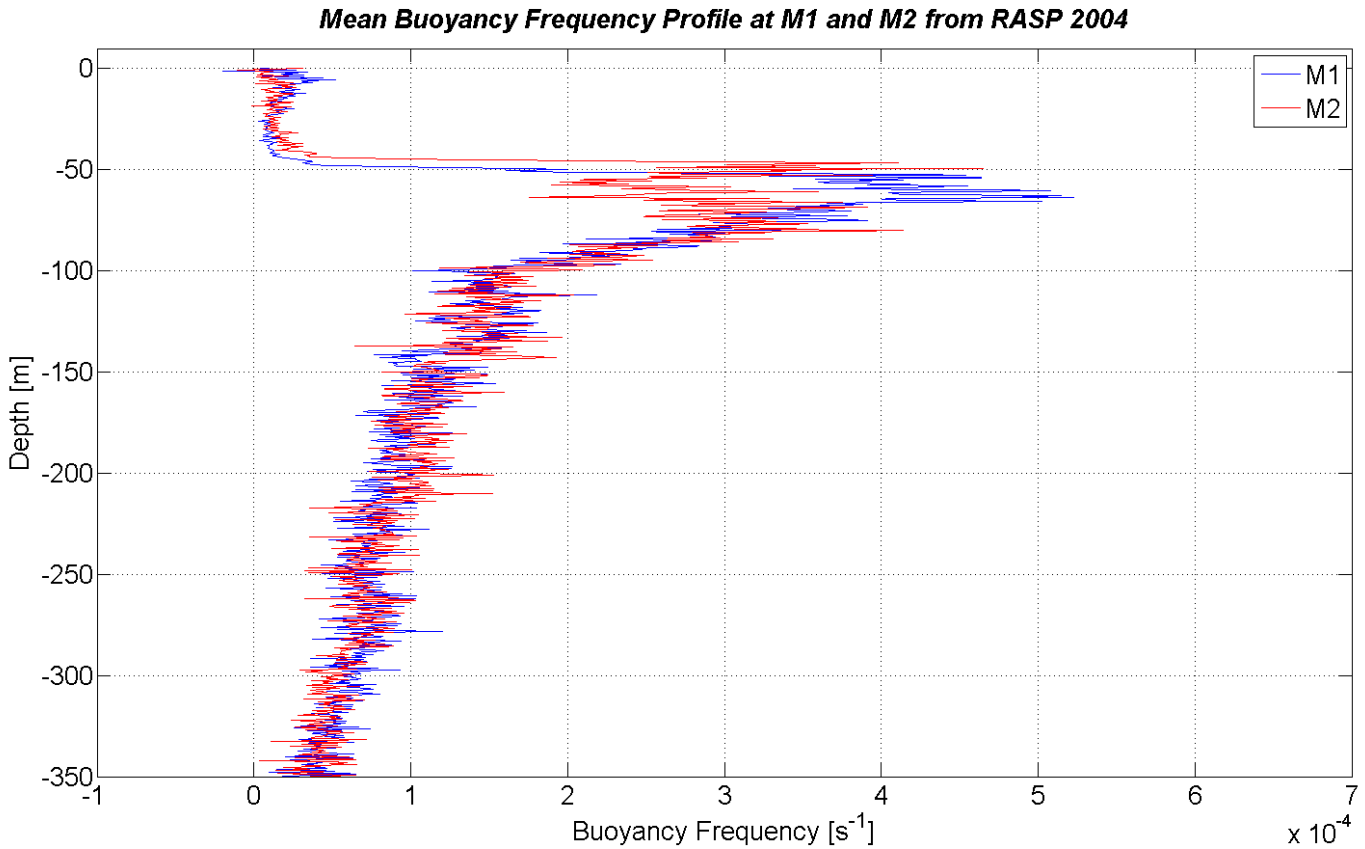

Figure 18. Mean vertical buoyancy frequency profiles from Anomaly Station M1 (blue) and the Ambient Station M2 (red).

2.4 Data

In the 20 days between August 10th and September 5th, 2004, a total of 484 vertical microstructure profiles were collected. Among those, 146 profiles were collected at the anomaly station (M1) and another 146 profiles were collected at the ambient station (M2). The rest are obtained from the station located at the end of the diffuser pipe (OF1) and stations along the transect from the diffuser to M1 (OF2, S1, S2, and S3). The stations and profiles collected from RASP 2004 are summarized in Table 4**.**

Table 4. Summary of vertical microstructure profiles collected during RASP 2004 at seven stations (Figure 13).

Station	Number of Profiles	Use in Data Analysis
OF1 (diffuser end)	40	Individual
OF2	38	Transect from diffuser to anomaly
S1	37	Transect from diffuser to anomaly
S2	39	Transect from diffuser to anomaly
S3	38	Transect from diffuser to anomaly
M1 (anomaly)	146	Experimental Station
M2 (ambient)	146	Controlled Station
Total number of	484	

It can be expected that different parts of the water column have different physical characteristics. For example, the upper mixed layer and bottom boundary layer are expected to have higher turbulent activities due to wind stress and boundary friction, respectively. To distinguish between different hydrographical regimes along the water column, it is necessary to divide the vertical profiles into the following vertical zones:

- Upper Mixed Layer (0 - 50 m, well-mixed water layer near the surface);
- Seasonal Pycnocline (~50 - 100 m, depending on stratification);

- Below Pycnocline (~100 - 320 m);
- Bottom Boundary Layer (bottom 30 m of the water column).

This classification of vertical zones agrees with the stratification structures observed from the mean density and buoyancy frequency profiles (Figure 19).

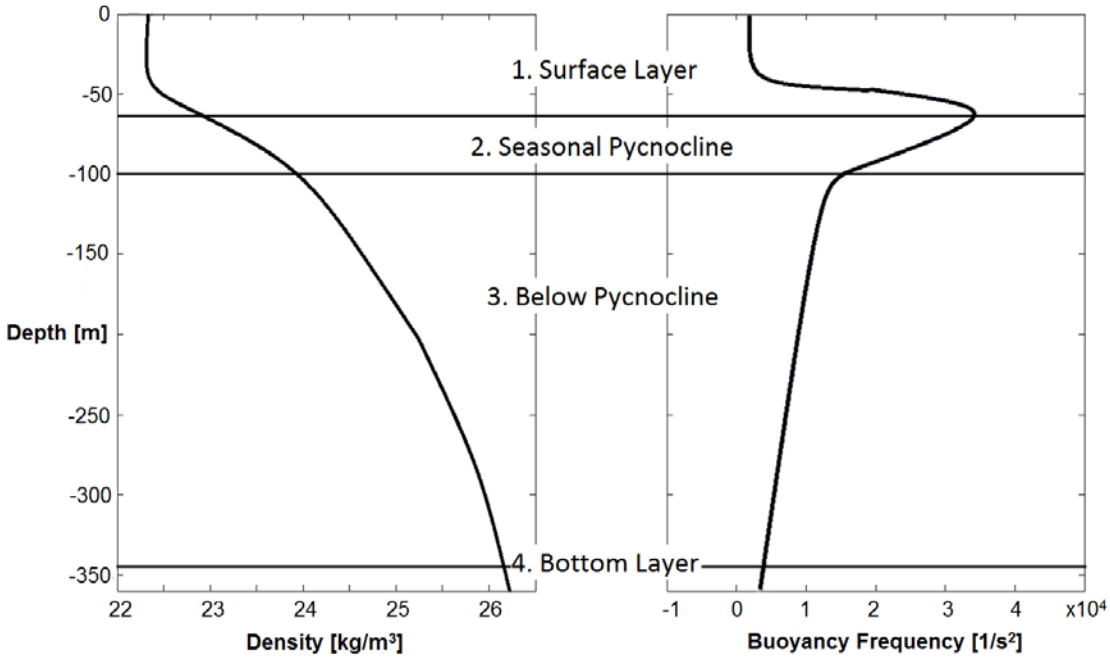

Figure 19. Averaged density (left) and buoyancy frequency (right) profiles of both anomaly and ambient stations. The vertical zones are defined based on these vertical characteristics.

Two averaging scales were used in this study. Parameters were either calculated by averaging over a 0.5 m range or averaging a defined turbulent patch. Table 5 shows the number of half meter segments and the number of identified patches for each vertical zones of each station. For example, parameters such as mean dissipation rate, vertical temperature gradient (dT/dz_{rms}), and Thorpe scale were averaged over a vertical scale of 0.5 m (Table 6). The benefit of this method is to provide a uniform and nonbiased view of the water column. However, the physical processes that occur in the water column are smoothed out by the averaging. Alternatively, the parameters can be averaged over the

scale of the overturn patch. This preserves the physics of the process so it can be studied. Turbulent patches in the density profiles are identified by using the zero-crossing counting method [*Prandke and Stips*, 1992] as described in the previous chapter. Consequently, patch parameters, such as vertical patch size, separation length (vertical distance between zero-crossing of the temperature microstructure gradient), mean patch dissipation, and maximum patch dissipation, turbulent Reynolds number Re_T, turbulent Froude number Fr_T, were calculated for each identified patch (Table 7). The mean values are considered to be statistically significant when their 95% confidence intervals (Table 8 and Table 9) do not overlap.

Table 5. Number of half-meter intervals and identified turbulent patches for the anomaly station (M1) and the ambient station (M2).

Vertical Zone	Number of Identified Patches		Number of 0.5 m Intervals	
	M1	M2	M1	M2
UP	491	656	11,887	11,536
SP	1,513	1,598	15,270	15,338
BP	6,649	6,915	62,380	60,427
BB	1,035	948	8,760	8,760
ALL	9,688	10,117	98,397	96,088

Table 6. Mean dissipation rates, dT/dz_{rms} values, and Thorpe overturn scales for the different vertical zones. The mean values are computed from the 0.5 m bins. Bold numbers in red indicate significant differences (95% confidence interval) between M1 and M2.

Parameter	Vertical Zone	M1 (anomaly)	M2 (ambient)
Dissipation Rate [W/kg]	UP	***0.632 x 10^{-7}***	***1.032 x 10^{-7}***
	SP	0.669 x 10^{-7}	0.737 x 10^{-7}
	BP	***0.329 x 10^{-7}***	***0.419 x 10^{-7}***
	BB	***0.654 x 10^{-7}***	***0.331 x 10^{-7}***
	Full Depth	***0.447 x 10^{-7}***	***0.536 x 10^{-7}***
dT/dz_{rms} [K/m]	UP	***0.086***	***0.089***
	SP	***0.176***	***0.187***
	BP	***0.163***	***0.179***
	BB	0.173	0.177
	Full Depth	***0.157***	***0.169***
Thorpe Scale [m]	UP	1.787	1.734
	SP	***0.179***	***0.209***
	BP	0.655	0.663
	BB	***1.046***	***0.961***
	Full Depth	0.760	0.753

Table 7. Mean properties of turbulence patches in different vertical zones. Bold numbers in red indicate significant differences (95% confidence interval) between M1 and M2.

Patch Parameter	Vertical Zone	M1 (anomaly)	M2 (ambient)
Mean Dissipation Rate [W/kg]	UP	1.780×10^{-7}	2.420×10^{-7}
	SP	0.482×10^{-7}	0.907×10^{-7}
	BP	0.353×10^{-7}	0359×10^{-7}
	BB	***0.205×10^{-7}***	***0.144×10^{-7}***
	Full Depth	0.486×10^{-7}	0.559×10^{-7}
Max. Dissipation Rate [W/kg]	UP	3.070×10^{-7}	3.970×10^{-7}
	SP	2.090×10^{-7}	2.170×10^{-7}
	BP	0.818×10^{-7}	0.910×10^{-7}
	BB	0.487×10^{-7}	0.447×10^{-7}
	Full Depth	1.096×10^{-7}	1.263×10^{-7}
Separation Length	UP	8.77	8.57
	SP	7.44	7.38
	BP	7.74	7.66
	BB	7.97	8.12
	Full Depth	7.77	7.12
dT/dz_{rms} [K/m]	UP	0.478	0.495
	SP	0.476	0.478
	BP	0.481	0.463
	BB	0.486	0.466
	Full Depth	0.481	0.467
Patch Size [m]	UP	1.505	1.468
	SP	1.680	1.860
	BP	1.927	2.128
	BB	2.060	2.206
	Full Depth	1.880	2.050

Table 8. Confidence Intervals of the calculated parameters. Differences between two parameters are considered to be statistically significant only when the two 95% confidence intervals do not overlap.

Parameter	Vertical Zone	Anomaly (M1)			Ambient (M2)		
		Mean	[Confidence Interval]		Mean	[Confidence Interval]	
Mean Dissipation Rate [W/kg]	**UP**	6.32E-08	5.54E-08	7.10E-08	1.03E-07	9.68E-08	1.10E-07
	SP	6.69E-08	6.11E-80	7.27E-08	7.37E-08	6.85E-08	7.89E-08
	BP	3.29E-08	3.17E-08	3.41E-08	4.19E-08	4.05E-08	4.34E-08
	BB	6.54E-08	4.65E-08	8.43E-08	3.31E-08	2.97E-08	3.66E-08
	Full Depth	4.47E-08	4.25E-08	4.70E-08	5.36E-08	5.21E-08	5.51E-08
dT/dz [K/m]	**UP**	8.64E-02	8.57E-02	8.71E-02	8.88E-02	8.81E-02	8.96E-02
	SP	1.76E-01	1.73E-01	1.79E-01	1.87E-01	1.83E-01	1.90E-01
	BP	1.63E-01	1.62E-01	1.65E-01	1.79E-01	1.78E-01	1.81E-01
	BB	1.73E-01	1.69E-01	1.77E-01	1.77E-01	1.73E-01	1.81E-01
	Full Depth	1.57E-01	1.56E-01	1.58E-01	1.69E-01	1.68E-01	1.70E-01
Thorpe Scale [m]	**UP**	1.79E+00	1.75E+00	1.83E+00	1.73E+00	1.70E+00	1.77E+00
	SP	1.79E-01	1.74E-01	1.84E-01	2.09E-01	2.03E-01	2.14E-01
	BP	6.55E-01	6.49E-01	6.62E-01	6.63E-01	6.57E-01	6.69E-01
	BB	1.05E+00	1.02E+00	1.07E+00	9.61E-01	9.40E-01	9.82E-01
	Full Depth	7.60E-01	7.52E-01	7.67E-01	7.53E-01	7.46E-01	7.59E-01

Table 9. Confidence Intervals of the calculated patch parameters. Differences between two parameters are considered to be statistically significant only when the two 95% confidence intervals do not overlap.

Patch Parameter	Vertical Zone	Anomaly (M1)			Ambient (M2)		
		Mean	[Confidence Interval]		Mean	[Confidence Interval]	
Mean Dissipation Rate [W/kg]	**UP**	1.78E-07	4.41E-07	2.15E-07	2.42E-07	2.03E-07	2.81E-07
	SP	8.42E-08	7.45E-08	9.40E-08	9.07E-08	8.06E-08	1.01E-07
	BP	3.53E-08	3.28E-08	3.77E-08	3.59E-08	3.38E-08	3.81E-08
	BB	2.05E-08	1.69E-08	2.42E-08	1.44E-08	1.23E-08	1.65E-08
	Full Depth	4.86E-08	4.55E-08	5.16E-08	5.59E-08	5.24E-08	5.94E-08
Max Dissipation Rate [W/kg]	**UP**	3.07E-07	2.45E-07	3.69E-07	3.97E-07	3.27E-07	4.67E-07
	SP	2.09E-07	1.66E-07	2.52E-07	2.17E-07	1.82E-07	2.51E-07
	BP	8.18E-08	7.40E-08	8.96E-08	9.07E-08	8.33E-08	9.88E-08
	BB	4.87E-08	3.34E-08	6.40E-08	4.47E-08	2.95E-08	5.99E-08
	Full Depth	1.10E-07	1.00E-07	1.19E-07	1.26E-07	1.17E-07	1.35E-07
Separation Length [m]	**UP**	8.77E-02	8.50E-02	9.05E-02	8.57E-02	8.35E-02	6.80E-02
	SP	7.44E-02	7.31E-02	7.56E-02	7.38E-02	7.25E-02	7.50E-02
	BP	7.74E-02	7.68E-02	7.80E-02	7.66E-02	7.60E-02	7.72E-02
	BB	7.97E-02	7.81E-02	8.12E-02	6.12E-02	7.96E-02	8.29E-02
	Full Depth	7.77E-02	7.72E-02	7.82E-02	7.72E-02	7.67E-02	7.71E-02
dT/dz [K/m]	**UP**	4.72E-01	4.55E-01	5.01E-01	4.95E-01	4.73E-01	5.16E-01
	SP	4.76E-01	4.63E-01	4.89E-01	4.78E-01	4.64E-01	4.91E-01
	BP	4.81E-01	4.75E-01	4.88E-01	4.63E-01	4.57E-01	4.67E-01
	BB	4.86E-01	4.70E-01	5.03E-01	4.66E-01	4.49E-01	4.83E-01
	Full Depth	4.81E-01	4.76E-01	4.86E-01	4.67E-01	4.62E-01	4.72E-01
Patch Size [m]	**UP**	1.51E+00	1.38E+00	1.63E+00	1.47E+00	1.37E+00	1.57E+00
	SP	1.65E+00	1.60E+00	1.76E+00	1.86E+00	1.77E+00	1.95E+00
	BP	1.93E+00	1.67E+00	1.98E+00	2.13E+00	2.68E+00	2.19E+00
	BB	2.06E+00	1.91E+00	2.21E+00	2.21E+00	2.01E+00	2.40E+00
	Full Depth	1.88E+00	1.84E+00	1.92E+00	2.05E+00	2.00E+00	2.10E+00

Because of the intermittency of turbulence parameters in the ocean (such as dissipation rate and microstructure temperature gradients), a large number of samples are necessary to provide results that can represent the overall condition and avoid undersampling error. A method to estimate the necessary number of samples based on the "intermittency factor" δ^2 was developed by *Baker and Gibson* [1987]. For example, it is estimated to obtain estimates of mean dissipation rates with 10% accuracy at the 95% confidence level in the seasonal thermocline ($\delta^2 = 3$) requires 2600 data samples and for Pacific equatorial undercurrent ($\delta^2 = 7$) requires 10,000 data samples. The required number of dissipation measurements is estimated and compared with the RASP 2004 dataset in Table 10. The value of δ^2 at each vertical zone is between 3.4 and 4.3 and it requires between 3000 and 5100 samples. The result confirmed that it satisfies the theoretical requirements on a 95% confidence level within 10% accuracy.

Table 10. Sampled and required number of dissipation measurements to achieve a 95% confidence level within 10% accuracy following *Baker and Gibson* [1987]. δ^2 is the intermittence factor of turbulence (variance of the natural logarithm of the measured dissipation rate).

Vertical Zones	δ^2	# Required by Theory	# Samples in 2004
UP	4.3	5,100	12,000
SP	4.1	4,900	15,000
BP	3.9	4,000	61,000
BB	3.4	3,000	9,000

2.5 Results

To demonstrate the effect of the independent variable, the results from the experimental station must be compared against the control station. Here the results from the anomaly station (M1) are compared against the ambient station (M2). As discussed in Section 2.3, M2 is expected to have a significantly higher dissipation rate than at M1 due to the environmental conditions of the site. This result can be observed in the mean

dissipation rate profiles of both stations (Figure 20). It is apparent that the dissipation rate is higher in the upper mixed layer (UP) and seasonal pycnocline (SP), while it is lower in the bottom boundary layer (BB) at M2.

To better visualize and quantify the differences between the stations, turbulent parameters at each station are presented as a ratio of the ambient (M2) to the anomaly (M1) in Table 11 and Figure 21. A value larger than 1 indicates the specific parameter is larger at M2 than at M1. Based on the environmental conditions (see Section 2.3), it is expected that the ratio of the dissipation rates of M2 to M1 at all vertical zones would be larger than 1 (Figure 21). If the observed data give the expected result, then it means the turbulence in the region is mainly environmental. If not, there must be additional forcing to produce the different than expected turbulent features.

Table 11. M2 to M1 ratio of the mean turbulence. Ratio > 1 indicates higher turbulence intensity in at the ambient station; values < 1 indicate higher values at the anomaly station.

Vertical Zones	Patches			Profile (0.5m bins)		All parameters
	Mean Dissipation	Max Dissipation	dT/dz	Mean Dissipation	dT/dz	Mean
UP	1.36	1.29	1.04	1.63	1.03	1.33
SP	1.08	1.04	1.00	1.10	1.06	1.04
BP	1.02	1.11	0.96	1.27	1.10	1.06
BB	0.70	0.92	0.96	0.51	1.02	0.82
ALL	1.15	1.15	0.97	1.20	1.08	1.09

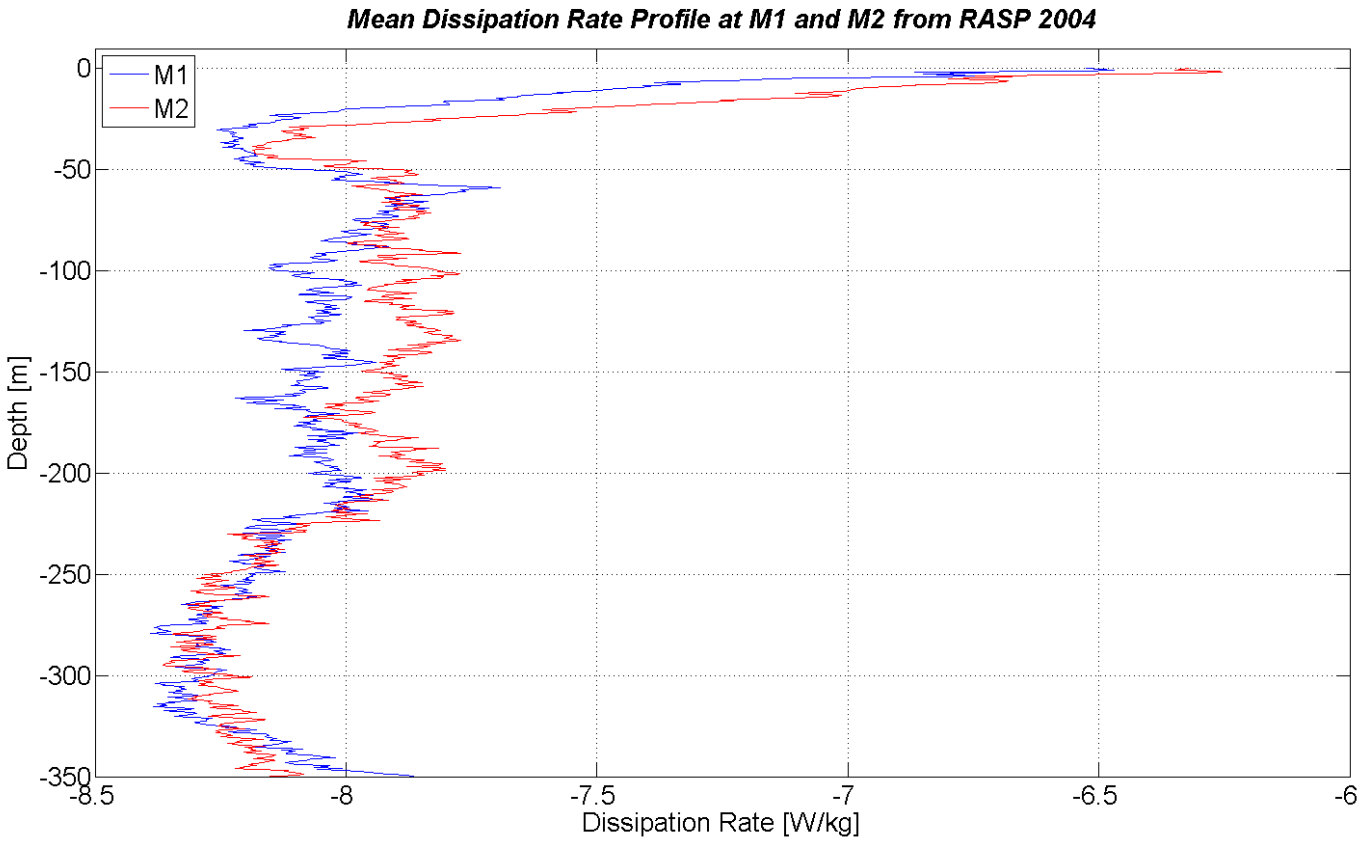

Figure 20. Mean dissipation profile at anomaly (blue) and at ambient (red), computed from all 146 profiles collected at each station. Dissipation rate is significantly higher in the upper mixing layer (0 to 50 m) at the ambient station due to higher wind stress. Because of the significant higher dissipation rate in the surface layer and below the pycnocline, the season pycnocline layer (50 to 100m) would be expected to have similar difference. On the contrast, the difference between the stations in the season pycnocline layer is very small. Higher dissipation rate can also be observed in the bottom boundary layer (320m to end of profile).

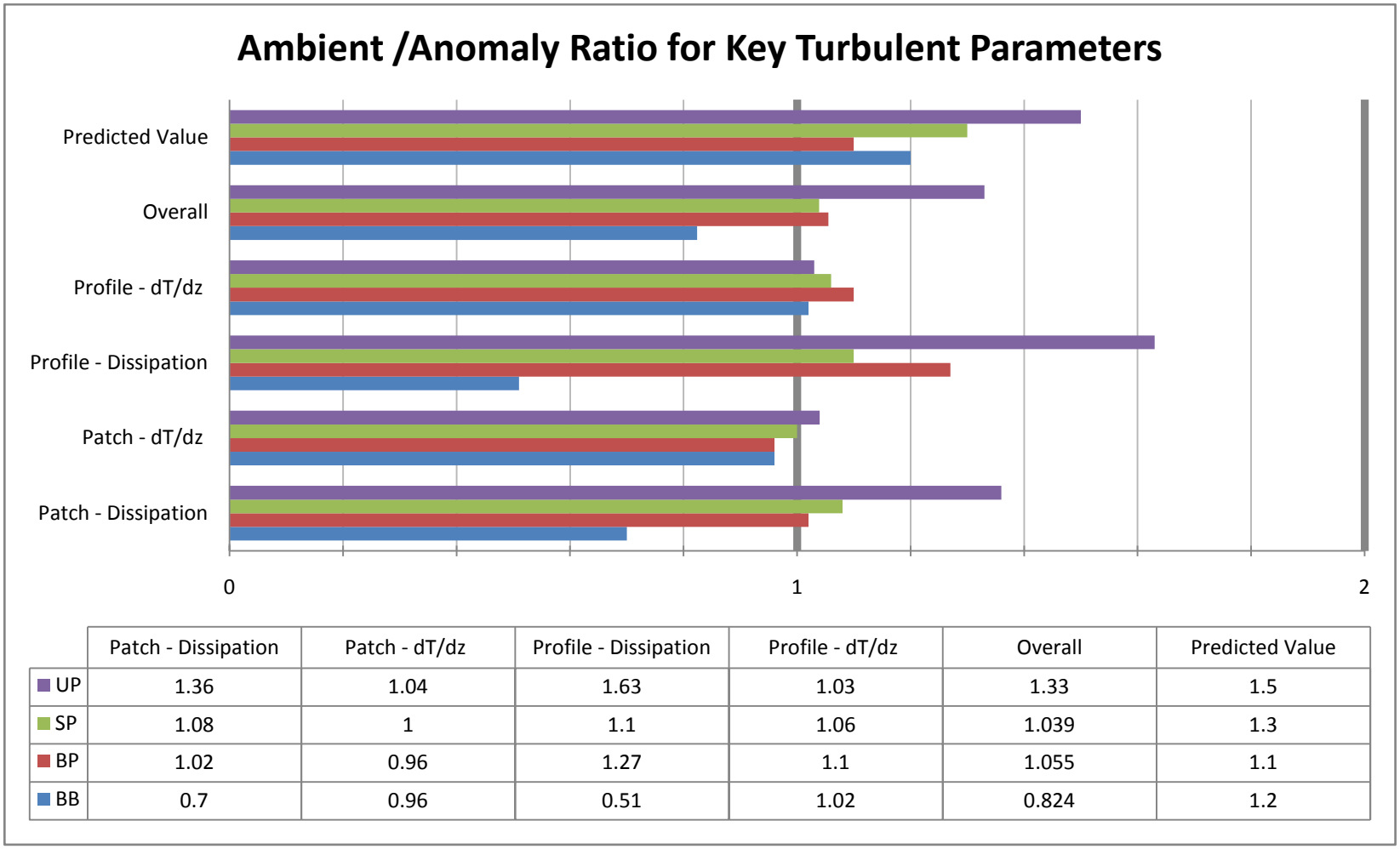

	Patch - Dissipation	Patch - dT/dz	Profile - Dissipation	Profile - dT/dz	Overall	Predicted Value
UP	1.36	1.04	1.63	1.03	1.33	1.5
SP	1.08	1	1.1	1.06	1.039	1.3
BP	1.02	0.96	1.27	1.1	1.055	1.1
BB	0.7	0.96	0.51	1.02	0.824	1.2

Figure 21. Ratio of key parameters between ambient and anomaly stations compared with the predicated values according to the environmental conditions. Ratio > 1 indicates that a parameter has a larger value at ambient.

The ratios of the observed dissipation rates at the upper mixed layer (UP) and below pycnocline (BP) are larger than 1 as predicted. The dissipation rate in the upper mixed layer (UP) is higher at M2 than at M1 by a factor of 1.63 (Table 11). This result agrees with the predicted value of 1.60 estimated from the average wind speed and kinetic energy (Table 3). The dissipation rate in the below pycnocline layer (BP) is also higher at M2 as predicted. For the seasonal pycnocline (SP), the ratio of dissipation rate is expected to be in between the value at UP and BP because of the penetration of the wind stress effect. However, ratio at SP is smaller than at BP. It suggests that the dissipation rate at M1 is higher than the ambient value. Hence, the dissipation rate at M1 is higher than expected and reduces the ratio of M2 to M1. Similarly, the less than 1 ratio suggests that a significantly higher bottom boundary layer (BB) dissipation rate is observed at M1. This contradicts the prediction that M2 should have a higher dissipation rate due to its steeper slope (Section 2.3). The mean BB dissipation rate at M1 exceeds the value at M2 by a factor of two (0.65×10^{-7} W/kg at M1 and 0.33×10^{-7} W/kg at M2). If the M2 is expected to have a higher dissipation rate throughout the water column due to the wind conditions and bottom topography, then it must require a very powerful turbulence source at M1 to result in higher dissipate rates.

A similar conclusion can also be drawn from the parameters averaged over identified patches (Table 11). They show higher turbulence intensity in UP and slightly higher in BP at M2 as predicted by the wind speed kinetic energy argument. In addition, it is also found that the turbulence is more intense in the SP and significantly higher in BB at M1 than at M2. Chapter III will take a more in-depth look at the patch parameters and the evolution of turbulent patches.

To minimize the differences caused by the effects of wind stress to the upper water column, the mean dissipation rates of SP and BP are normalized by the dissipation rate of UP at each station. Thus, the normalized UP dissipation rates at both stations become 1. The normalized mean BP dissipation rate is 0.52 for anomaly (M1) and 0.41 for ambient (M2). Based on the confidence intervals of those two values, this difference is insignificant. The normalized mean SP dissipation rate is 1.1 for at M1 and 0.72 for at

M2. This is a significant difference of over 50%. If the environmental conditions are nearly identical at both stations and the effect of wind stress is neglected, then the observed difference must be caused by a very energetic source in the anomaly area.

In summary, a higher dissipation rate is observed at M1's SP and BB. This observed difference, occurring only in certain vertical zones, indicates that the turbulent source must be located from a distance away from the stations and its influence propagates horizontally throughout the layer. Since the control ambient station (M2) is practically identical to the experimental anomaly station (M1) except for the existence of the Sand Island outfall diffuser, it can be concluded that the diffuser jets are responsible for the elevated mixing activities observed in the SP and BB layers at M1.

(Note that the SI units, W/kg, of dissipation rate are used here. Since W = J/s = kg m^2/s^3, so W/kg is identical to m^2/s^3 as seen in text that prefers kg-m-s units. The value of the dissipation rate can range from 10^{-1} W/kg in a very active region to 10^{-10} W/kg (instrumentation limits) in a very quiet abyss.)

2.6 Two Possible Mechanisms

Results from the comparison of the experimental and control time series data revealed that the sewage outfall diffuser jets enhanced the turbulence mixing in the seasonal pycnocline and bottom boundary in the area. The ambient control station shows relatively weak mixing at the depth of the pycnocline and bottom boundary layer, compared with the region near the diffuser. There are two possible mechanisms that could cause the observed result: 1) The advection of turbulent sewage water (plume) from the outfall into the anomaly area and 2) internal waves generated and radiated from the diffuser jets.

To study the advection of the highly turbulent plume water from the diffuser to the far field, two GPS drogues (Figure 22) were deployed on 13 of the 20 measurement days. The deployment covered complete tidal cycles in Mamala Bay (Figure 23). The

drogues were deployed directly above the diffuser at the trapping depth of the sewage and the parachutes were set at 30m and 50m below the surface. Their tracks were recorded by the attached GPS. The drifting-paths of the drogues reveal that the sewage plume advected along the shore, westward during one of the 13 observation and southeastward for the rest (Figure 23). This finding is in agreement with other observations such as *Fischer et al.* [1979] and showed that the turbulent sewage plume was never advected offshore into the anomaly area.

For this current pattern, the discharge of waste water released from the diffuser was modeled by *Bondur et al*. [2009]. According to the model (Figure 24), the extent of the plume into the anomaly area is limited to approximately 600 m south of the diffuser. This result also is supported by microstructure measurements from Station OF2 (midpoint of the diffuser) to Station M1 and is plotted as a transect contour plot. The temperature gradient, optical backscattering, and dissipation rate show that the sewage water was trapped in the range of the pycnocline. The extent of the discharged sewage into the anomaly area was limited to Station S2, approximately 600 m away from the diffuser.

Summarizing the observations of sewage plume water discharged into the anomaly area, there is no indication that the differences in turbulence intensity between the anomaly and ambient stations are caused by turbulent water bodies advected from the diffuser. Hence, the proposed advection scenario is rejected.

RASP 2004 measurement campaign was not designed to investigate the internal waves generated by the diffuser jet. However, detail of the hypothesized internal waves mechanism will be discussed in Section 4.3.

Other major conclusions from RASP 2004 are summarized in Figure 25.

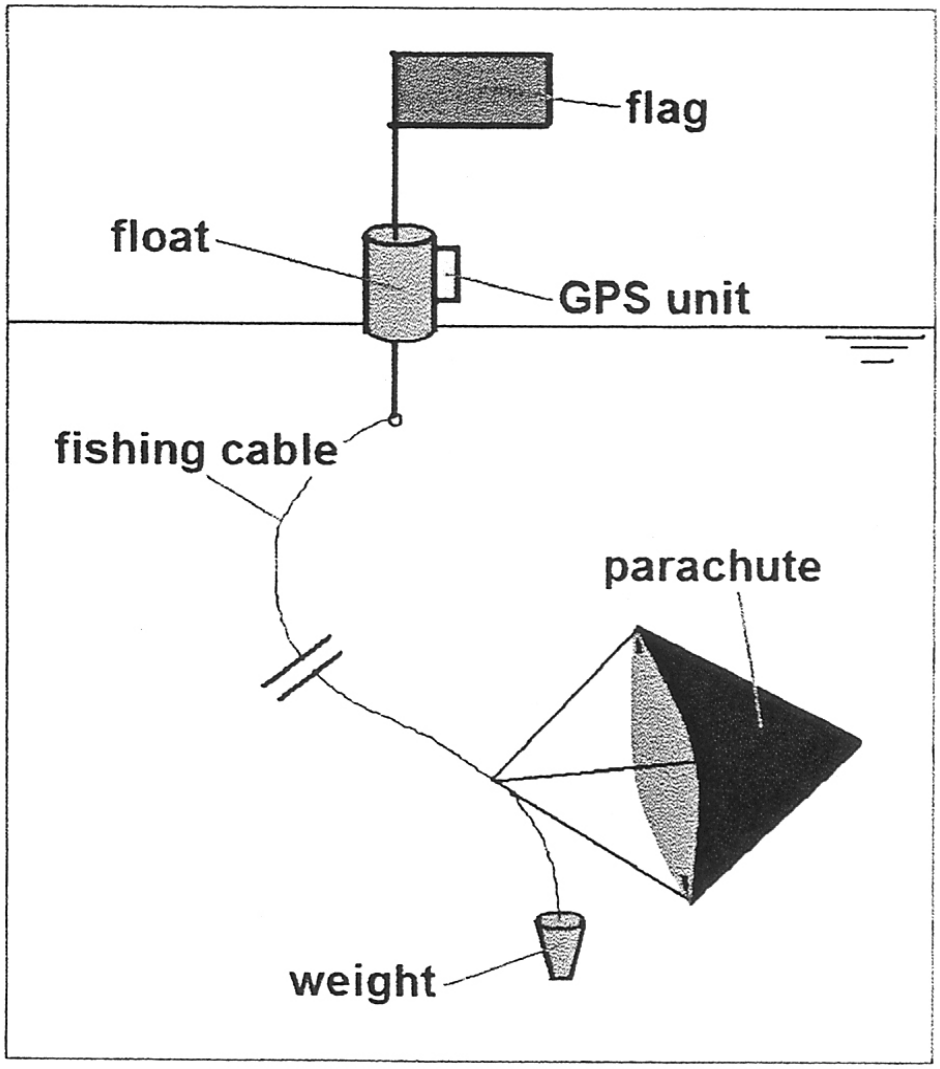

Figure 22. Schematic of drogues constructed to observe sewage advection. Parachutes are set at depth of 30m and 50m. A GPS receiver monitored the drift path of the drogues until they were recovered in the evening.

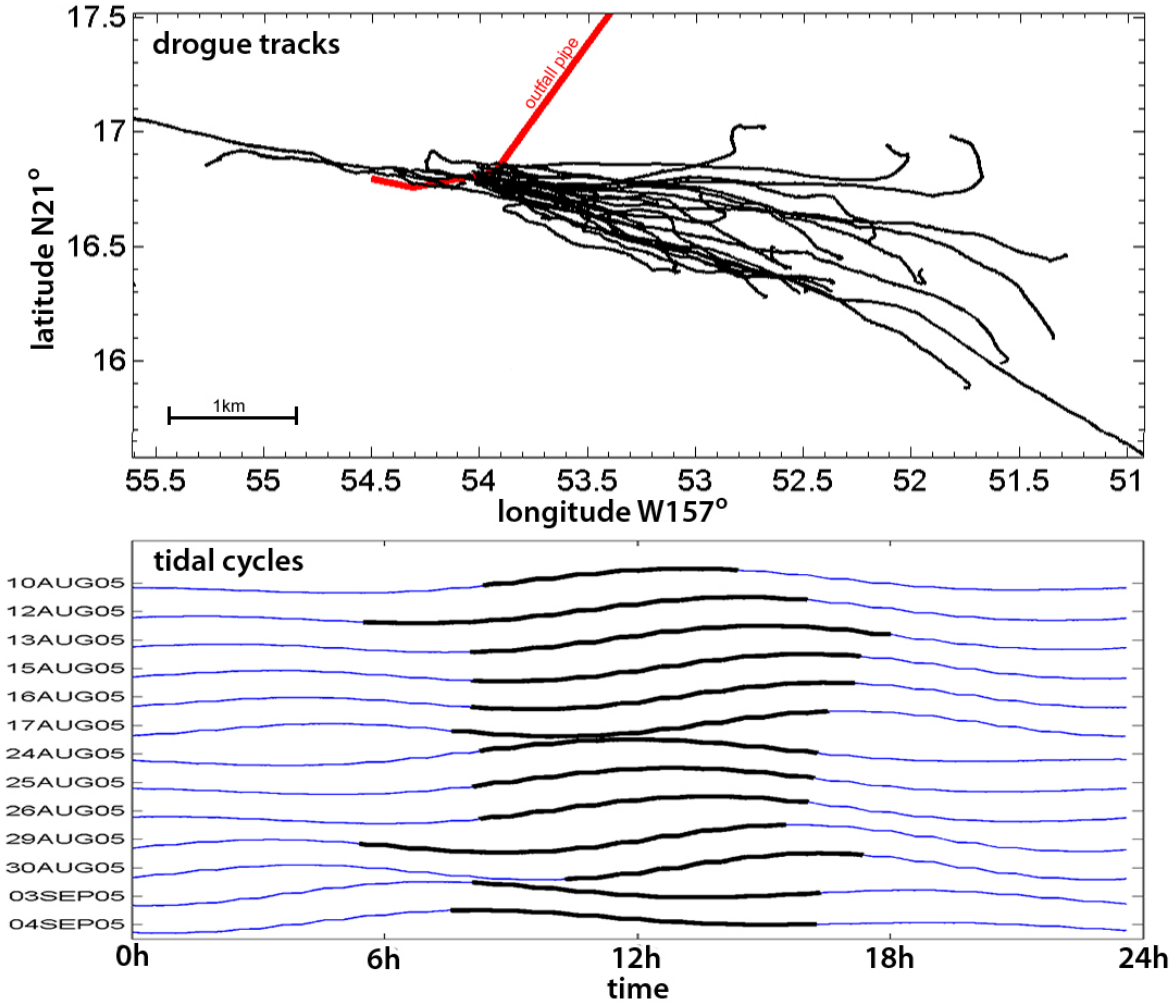

Figure 23. Drogue paths deployed during RASP 2004 to study the advection of sewage from the outfall. The drogues were deployed in the morning just above the diffuser at 30 m and 50 m depth. The lower panel shows the phase of the tidal cycle for the periods during which the drogues were in the water. The RASP 2004 drogue measurement periods covered all phases of the tidal cycle.

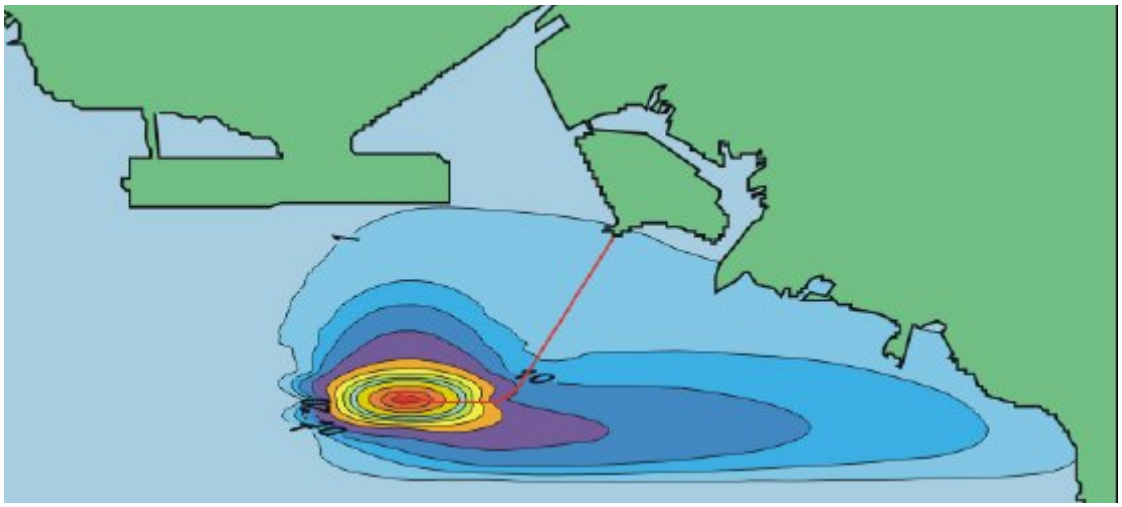

Figure 24. Result of numerical modeling of the plume water discharge in case of easterly currents (prevailing current direction during the RASP 2004 test phase). Note that the extent of the plume water in offshore (anomaly area) direction is approximately 600 m (length of the diffuser). [*Bondur et al.*, 2009].

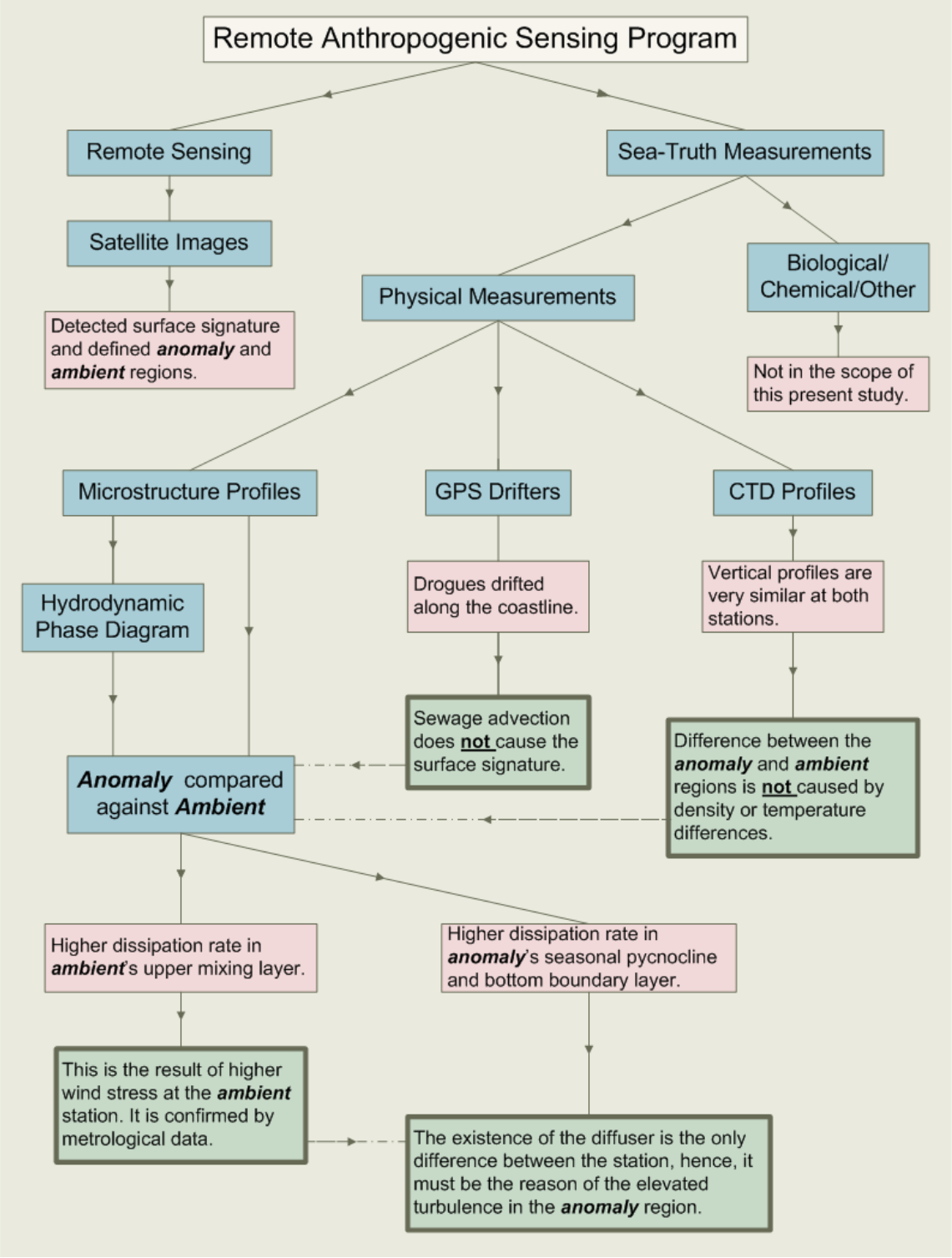

Figure 25. Summary of results and conclusion drawn from the physical parameters measured from the RASP.

CHAPTER III
COASTAL BUOYANCY TURBULENCE

3.1 Sample HPD from RASP 2002

Seven patches from RASP 2002 are selected to demonstrate the concept of the hydrodynamic phase diagrams (HPDs) and the issue caused by undersampling. These patches are identified from two microstructure profiles obtained near the diffuser (Figure 26). G4060001 (Figure 27, Figure 28) is collected at the western end of the diffuser section. A section of G4060001 between 40 and 45m is showed in Figure 29 to demonstrate turbulent patches found in vertical structures. G4010001 (Figure 30) is collected at approximately 3 km south of the outfall diffuser (Figure 26). Buoyancy frequency (N) and Thorpe Scale (L_T) are computed from the reordered density profile and averaged over the patch (Table 12). The normalized Froude numbers and normalized Reynolds numbers are then calculated as described in Chapter I and detailed in *Leung and Gibson* [2004].

Table 12. RASP 2002 parameters computed for the Hydrodynamic Phase Diagram shown in (Figure 31). L_{Tmax} is the maximum Thorpe overturn scale of the patch. The normalized Froude number is defined as Equation 7 and the normalized Reynolds number is defined as Equation 8.

Profile	Patch	Depth [m]	L_{Tmax} [m]	Re/Re_F	Fr/Fr_o
G4060001	A	68.3	0.6	49.96	0.51
G4060001	B	65.8	0.4	121.37	0.93
G4060001	C	56.8	1.1	485.62	0.99
G4060001	D	50.8	6.9	186.49	0.13
G4010001	E	200.6	4.1	267.16	0.43
G4010001	F	88.1	4.1	31.78	0.14
G4010001	G	67.7	10.8	632.36	0.28
G4030002	H	8.8	0.5	344.02	1.11

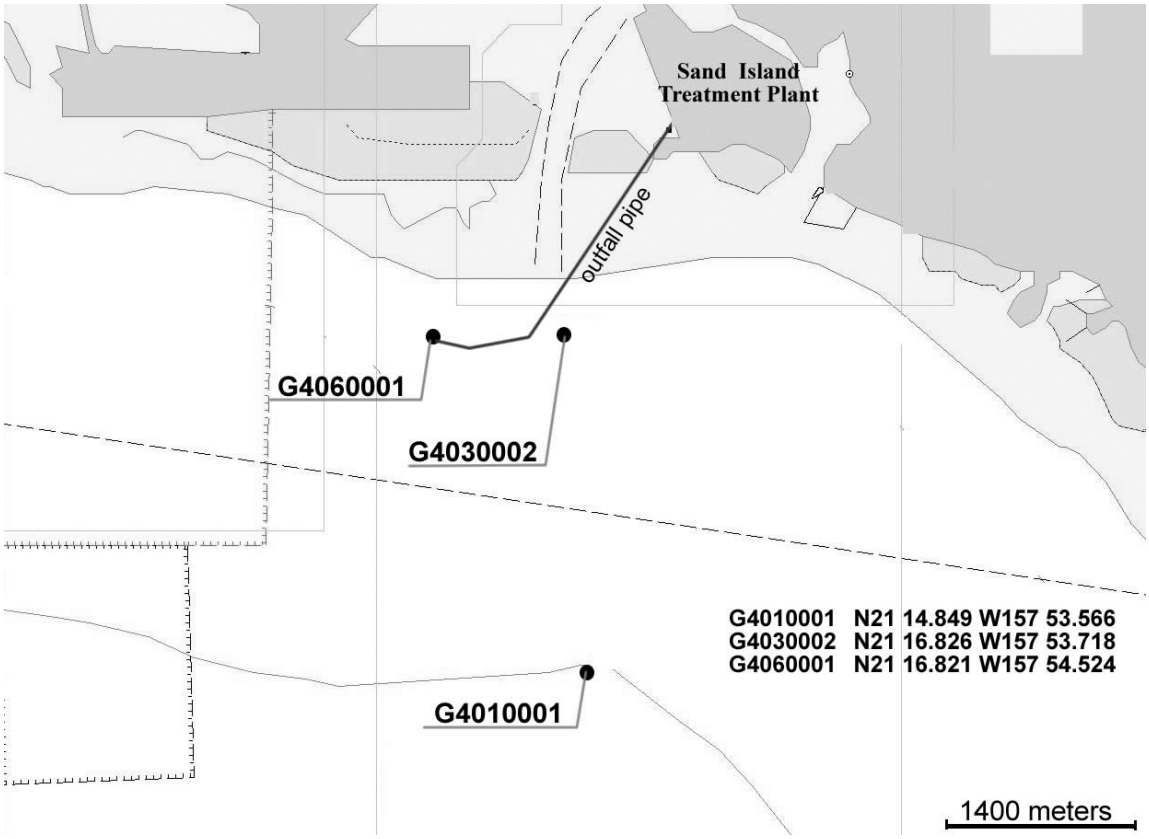

Figure 26. Location of selected RASP 2002 microstructure measurement profiles. G406001 and G403002 are collected at the west and east end of the Sand Island sewage outfall. G4010001 is collected approximately 3 km south of the outfall.

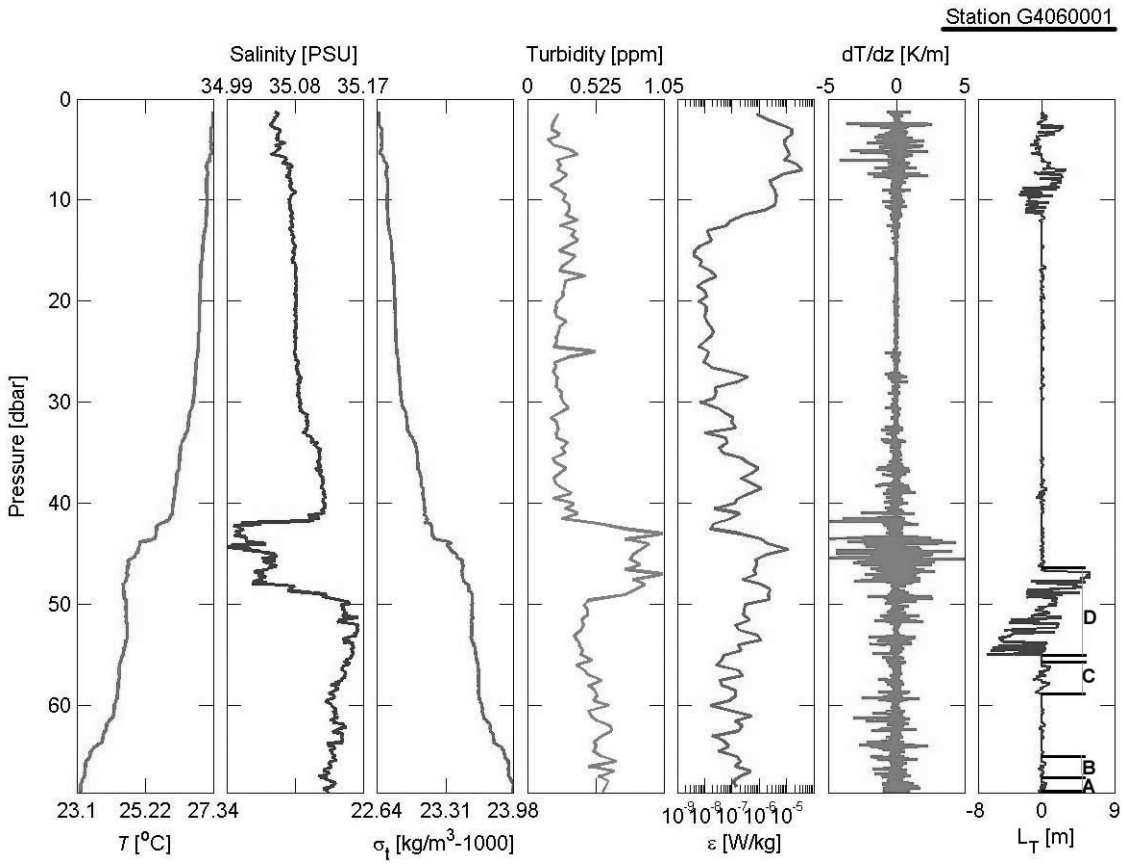

Figure 27. Microstructure profile at G4060001 near the eastern end of the diffuser (Figure 26), on September 2nd, 2002. From the left, temperature (°C), salinity (PSU), density (kg/m^3 -1000), turbidity (ppm), dissipation rate (W/kg), temperature gradient dT/dz (K/m), and Thorpe displacement scale L_T (m) are shown. The low salinity, high turbidity signature of the trapped plume can be identified between 42 and 50 m. Microstructure patches A, B, C, and D were identified from the Thorpe density displacement profile on the right most panel.

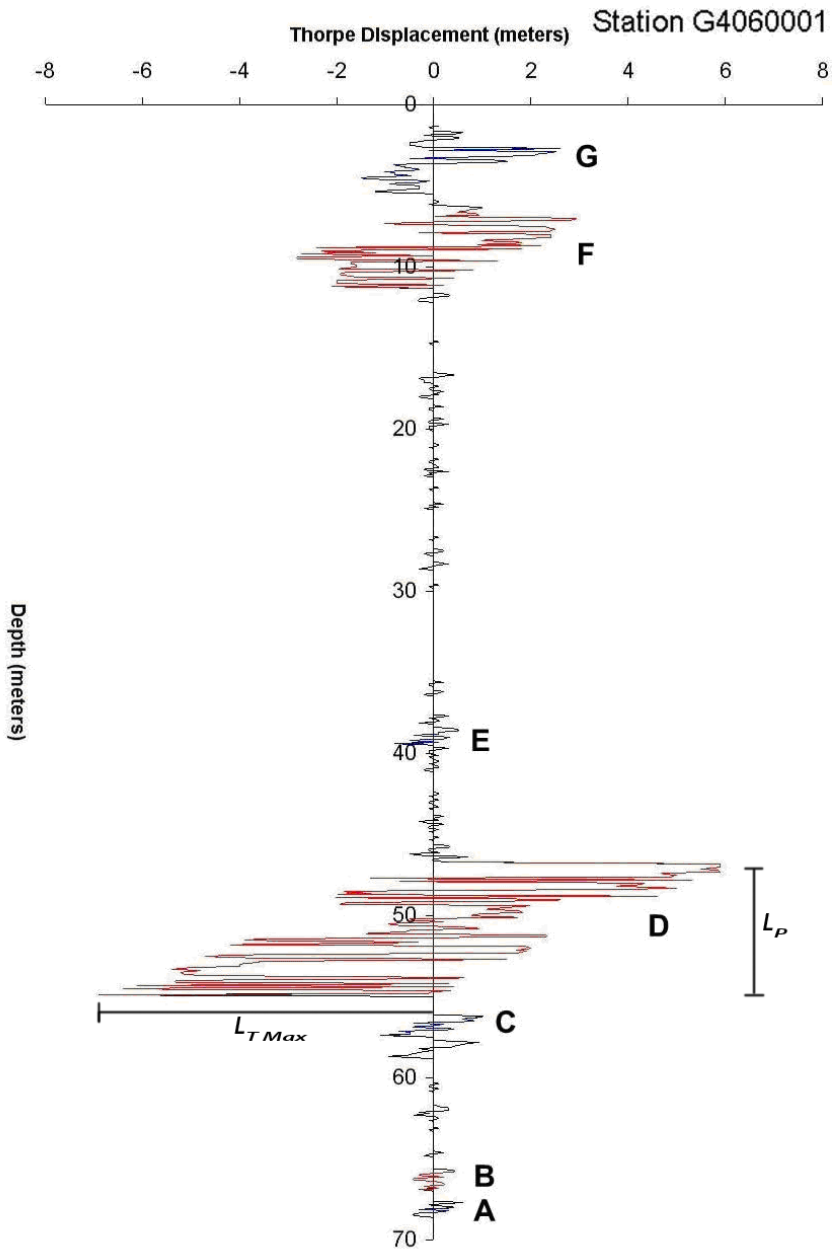

Figure 28. Example of patch identification from a Thorpe displacement profile. Maximum Thorpe displacement scale (L_{Tmax}) is the displacement of the water parcel from its stably stratified depth. Patch thickness (L_P) is the vertical scale of the overturning patch. Patches are identified and labeled from A to G. For example, patch D is L_p = 7.5 m, with L_{Tmax} = 7 m, and located at 50 m below surface.

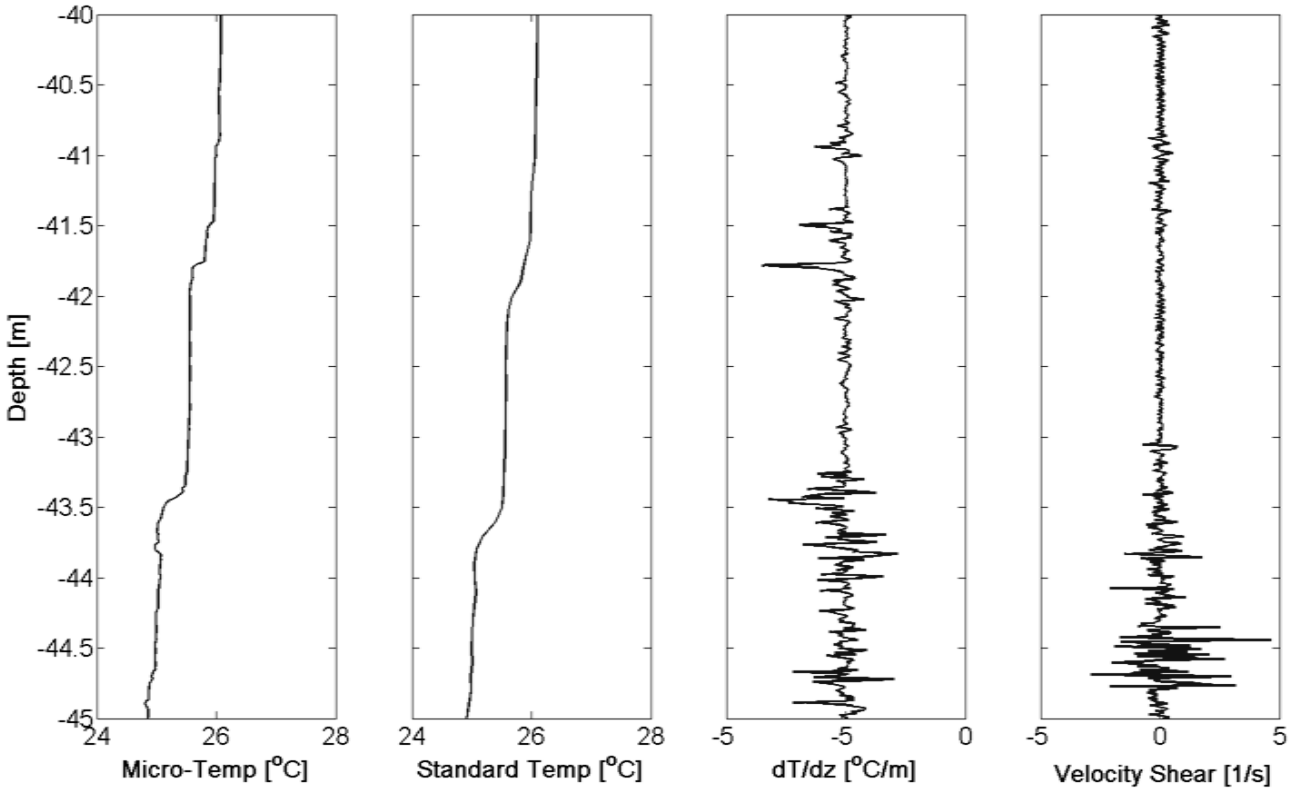

Figure 29. Section of profile G406001 between 40 and 45m. From left to right, first panel is microstructure temperature profiled by FP07 sensor with 10ms response time and 0.01m spatial resolution, second panel is standard temperature profile from PT100 sensor with 200ms response time and 0.1m spatial resolution, third panel is dT/dz calculated from microstructure temperature, and forth panel is velocity shear measured from a shear probe with 3ms response time. Standard temperature sensor profiled to obtain the fine structures in the water column. Patch structures outlined in Figure 1 can be seen here. A temperature structure without a corresponding velocity structure can be seen between 41.5m and 43.5m, a typical case for a completely fossilized patch. In contrast, strong velocity structure can be observed associated with the small scale temperature structure at 44.5m. Those are believed to be active overturns.

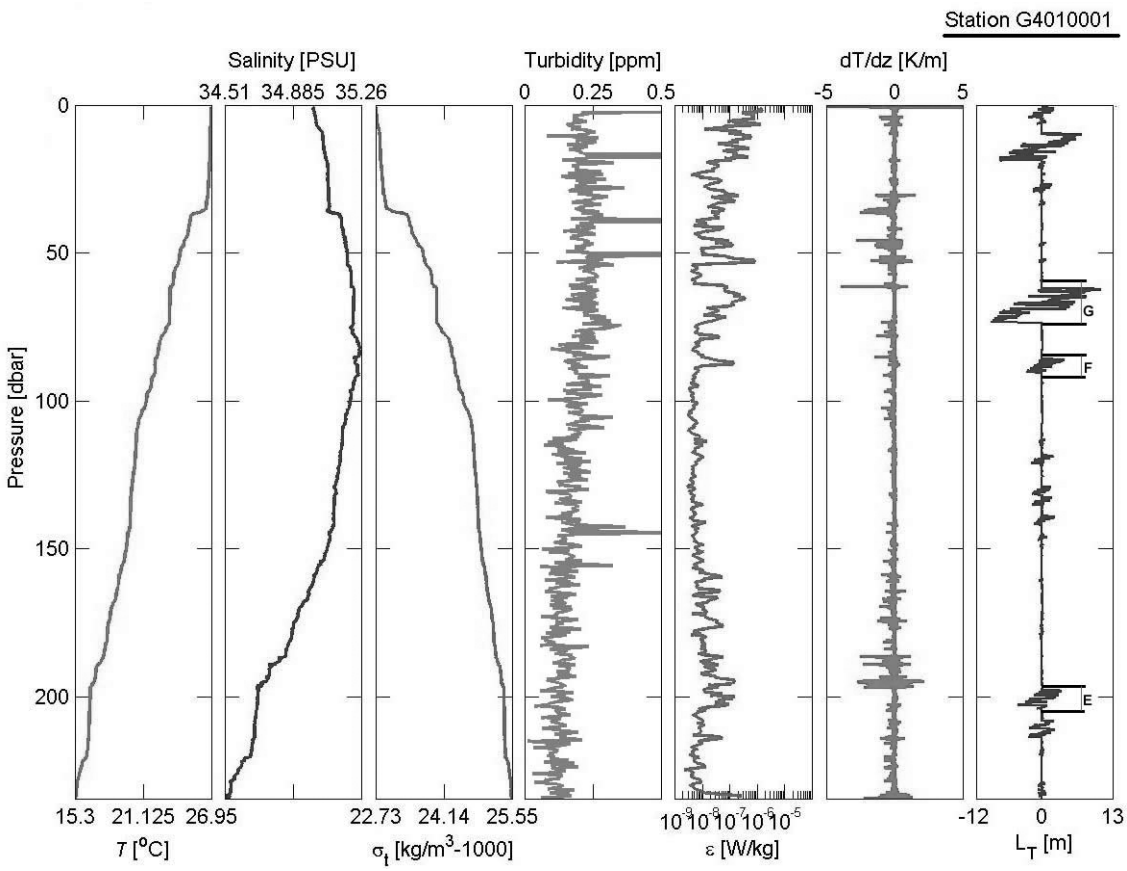

Figure 30. Microstructure profile at G4010001 about 3 km south of the diffuser (Figure 26). Microstructure patches E, F, and G were identified for analysis from the Thorpe displacement profile.

Consider patches A, B, C, and D from profile G4060001 (Figure 27) and their corresponding points on the HPD (Figure 31). A and B are two 0.5 m patches obtained at approximately 2 m and 4 m above the diffuser. They would be expected to be active patches because of the relatively small patch sizes and short distances from the diffuser. On the HPD, both points are located in the active+fossil quadrant, with the value of normalized Froude numbers (Fr/Fr_o) close to 1. This indicates that they were both active patches and were being damped out rapidly by buoyancy at the time of measurement. The overturn length scales L_{Tmax} of patches A, B, C, and D monotonically increase from 0.5 m to nearly 8 m as the sewage plume rises to the trapping depth and the patches grow from small scales to large. Patch D, the largest patch among the four, is located in the active+fossilized quadrant of the HPD. Even when the patch is being damped by buoyancy (kinetic energy being dissipated), its length scale is still preserved in the scale structure.

G4010001 is collected approximately 3 km south of the diffuser (Figure 26). All of its identified patches (E, F, and G) are located in the bottom left of the active+fossil quadrant (relatively smaller normalized Froude numbers). This result suggests these patches underwent further buoyancy damping than the ones found near the diffuser. They will eventually be damped by both buoyancy and viscous forces and will be fully fossilized. It is rare to find any active patches from the ocean interior because they are rapidly damped by buoyancy and other forces. H is collected from near the surface of G4030002 and was chosen to represent patches generated by wind mixing. Patch H is located in the active-turbulence quadrant of the diagram indicating it is an overturning patch, which is what would be expected in the mixing layer.

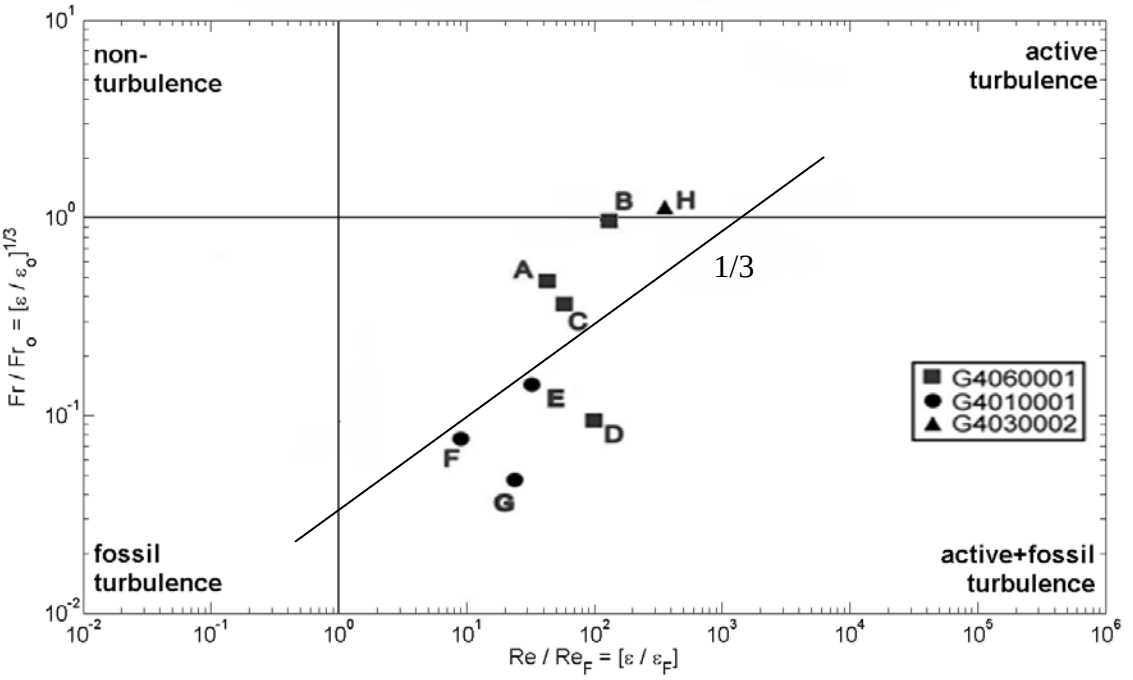

Figure 31. Hydrodynamic Phase Diagram from three selected microstructure measurements. Patches from G4060001 (squares) are collected at the west end of the outfall diffuser (Figure 26). Patches from G4010001 (circles) are collected 3km south of the diffuser. The 1/3 slope decay line indicates the evolution of patch decay. Patch H from G4030002 (triangle) is collected from the east end of the diffuser near the surface.

There were 1405 HPD points computed from the RASP 2002 profiles. Among those, 215 patches are active, 1185 are active+fossil, and only 5 are completely fossilized. Many of the active patches are found above other large non-active patches in the diagram, indicating these are secondary turbulent events possibly triggered by some vertical internal wave radiating mechanism. Such a patch that was brought back to life was coined “zombie turbulence” by Hide Yamazaki and observed in other buoyancy turbulence laboratory studies [*Rotter et al.*, 2007; *Gerz and Yamazaki*, 1993]. It is hypothesized that when propagating through the active+fossil patches, internal waves with comparable frequency would be able to reactivate the overturning motions of active+fossil patches.

The RASP 2002 dataset suffered from two major problems. First, the dataset were undersampled. Less than 0.5% of the identified patches are fossilized which indicates the dataset failed to cover the evolution of the turbulent patches from active to fossil, and hence, it is incomplete. This is mainly due to the measurement approach used in 2002, in which only the measurement was focused on the area near the diffuser (Figure 12). This introduces spatial and temporal bias to the dataset. It is a conceptual mistake to lump all the identified patches into one HPD and consider them as the result of one turbulent event, even when those patches are actually obtained at different time and at different locations.

Vertical profiles are only snapshots of the water column. Individual profiles are not enough to provide information on the overturn dynamics. Hence, it is necessary to profile the same location repeatedly over an extended period of time. Each observed patch can only represent a split second of the ongoing event. Conclusions regarding the hydrodynamic condition can only be made after all profiles are compiled and studied as a whole.

3.2 Results from RASP 2004

The measurement strategy was modified in 2004 based on the lessons learned from the 2002 and 2003 campaigns. All measurements were focused on the ambient and anomaly stations (Figure 14 and Chapter II) over 20 days. HPDs of turbulent patches generated by only natural sources can then be compared against with the one from man-made sources. As a result, RASP 2004 provided a unique opportunity to study the hydrodynamic state of a coastal region influenced by a submerged turbulence source. The outfall diffuser jets act as sources of submerged turbulence. It is believed that no other microstructure measurement campaign provides such a complete set of controlled HPD data.

There are 19,805 HPD points computed from RASP 2004 data (Figure 32). Among those 2% are active, 93% are active+fossil, and 5% are fossil. Grouped by stations, there are 9,692 points for the anomaly station (M1) and 10,117 HPD points for the ambient station (M2); the difference is approximately 4%. For M1, 2% are active patches, 93% active+fossil, and 5% are completely fossilized patches (Figure 33). For M2, 3% of them are active patches, 92% active+fossil, and 5% completely fossilized patches (Figure 34). The turbulent hydrodynamic states (phase of patch decay) of the two stations are almost identical to the overall hydrodynamic state of the entire region. This confirms that each station includes sufficient data for a representative time series. The slightly larger percentage of active patches at M2 is the result of higher wind stress due to its geographical location. The relative difference in wind stress between the stations is about 2%, as discussed in Chapter II.

The points are further categorized by depth (Figure 35 to Figure 42). The vertical zone categorization is described in Chapter II. A summary of each group can be found in Table 13 and Table 14. For the bottom boundary layer (BB), 2% of the anomaly eddies are active while only 0.5% are active in the ambient station. This agrees with the observed result as discussed in Chapter II. The enhanced turbulence activities in the anomaly region due to the diffuser jets provide a very significant result that can be used to differentiate the anomaly station from the ambient. Below the pycnocline (BP), a slight increase of active eddies (0.4% at M1 and 0.2% at M2) is observed. This is another feature that can be used to distinguish between the stations. At the depth of the seasonal pycnocline (SP), the hydrodynamic conditions are similar for both stations except that more patches are fossilized at M1.

For the uppermost region (UP), M2 has a significantly larger percentage of active eddies than the same group in M1, this is direct result of the wind conditions. Note that a significant number of uppermost anomaly eddies are active+fossil. As discussed previously, these patches are buoyancy-damped, yet to collapse, and capable of turning into zombies (i.e. re-activated patches). They are likely to be responsible for the surface signature observed by the optical satellite image.

From the RASP 2004 HPDs, it can be concluded that there are more active turbulence activities in the upper mixed layer at the ambient station due to higher wind stress. Elevated turbulence activities are observed in the seasonal pycnocline and bottom boundary layer at the anomaly station. All these results agree with the conclusion drawn by statistical analysis of the same dataset (Chapter II). Considering only the bottom three vertical zones (seasonal pynocline, below pynocline, and bottom boundary), the turbulence hydrodynamic states of the two stations are similar but with a noticeable difference: the total number of active patches is double in the anomaly station. Since the dataset were collected during varying meteorological, tidal, and current conditions, those effects would have equal effects on both stations. The existence of a submerged turbulence source in its proximity is the only long-lasting condition that is capable of producing more active patches at the anomaly station.

Table 13. Mean properties of turbulence patches in the different depth ranges. Bold numbers in red indicate a significant difference (95% confidence interval) between the stations.

Parameter	Vertical Zone	M1 (anomaly)	M2 (ambient)
ε_o [W/kg]	UP	0.726×10^{-5}	0.342×10^{-5}
	SP	10.15×10^{-5}	10.971×10^{-5}
	BP	2.958×10^{-5}	2.865×10^{-5}
	BB	1.015×10^{-5}	1.326×10^{-5}
	Full Depth	3.760×10^{-5}	3.837×10^{-5}
ε_F [W/kg]	UP	***1.300×10^{-9}***	***0.957×10^{-9}***
	SP	6.837×10^{-9}	7.273×10^{-9}
	BP	***2.357×10^{-9}***	***2.507×10^{-9}***
	BB	1.357×10^{-9}	1.388×10^{-9}
	Full Depth	2.869×10^{-9}	3.055×10^{-9}
Patch Size [m]	UP	1.505	1.468
	SP	1.680	1.860
	BP	1.927	2.128
	BB	2.060	2.206
	Full Depth	1.880	2.050

Table 14. Number of Hydrodynamic Phase Diagram points computed from RASP 2004 data. Numbers in red indicate significant higher value in that group between the ambient and anomaly stations.

	Total #	# of Active		# of Active+fossil		# of Fossil	
Both Stations	**19,809**	469	2.4%	18,390	92.8%	946	4.8%
Ambient	**10,117**	291	2.9%	9,349	92.4%	477	4.7%
Anomaly	**9,692**	178	1.8%	9,041	93.3%	469	4.8%

Ambient	**Total #**	**# of Active**		**# of Active+fossil**		**# of Fossil**	
Whole Column	**10,117**	291	2.9%	9,349	92.4%	477	4.7%
Upper	**656**	273	41.6%	382	58.2%	1	0.2%
Pycnocline	**1,598**	1	0.1%	1,502	94.0%	95	5.9%
Below Pycnocline	**6,915**	12	0.2%	6,564	94.9%	339	4.9%
Bottom Boundary	**948**	5	0.5%	901	95.0%	42	4.4%

Anomaly	**Total #**	**# of Active**		**# of Active+fossil**		**# of Fossil**	
Whole Column	**9,692**	178	1.8%	9,041	93.3%	469	4.8%
Upper	**491**	131	26.7%	358	72.9%	2	0.4%
Pycnocline	**1,513**	1	0.1%	1,405	92.9%	107	7.1%
Below Pycnocline	**6,649**	25	0.4%	6,325	95.1%	299	4.5%
Bottom Boundary	**1,039**	21	2.0%	953	91.7%	61	5.9%

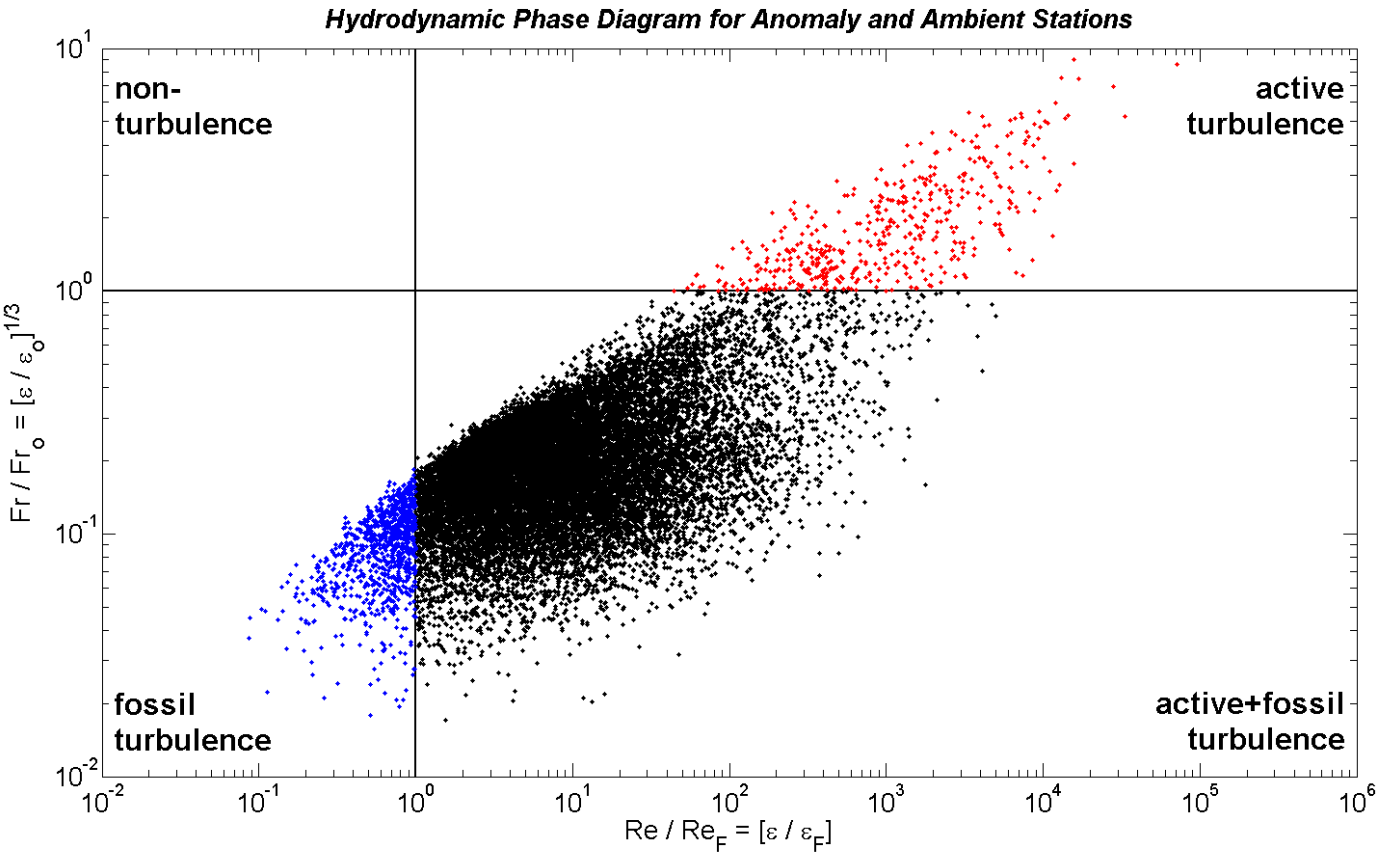

Figure 32. Hydrodynamic Phase Diagram for all patches observed in RASP 2004. Red dots indicate active patches. Black dots indicate active+fossil patches. Blue dots indicate fossilized patches.

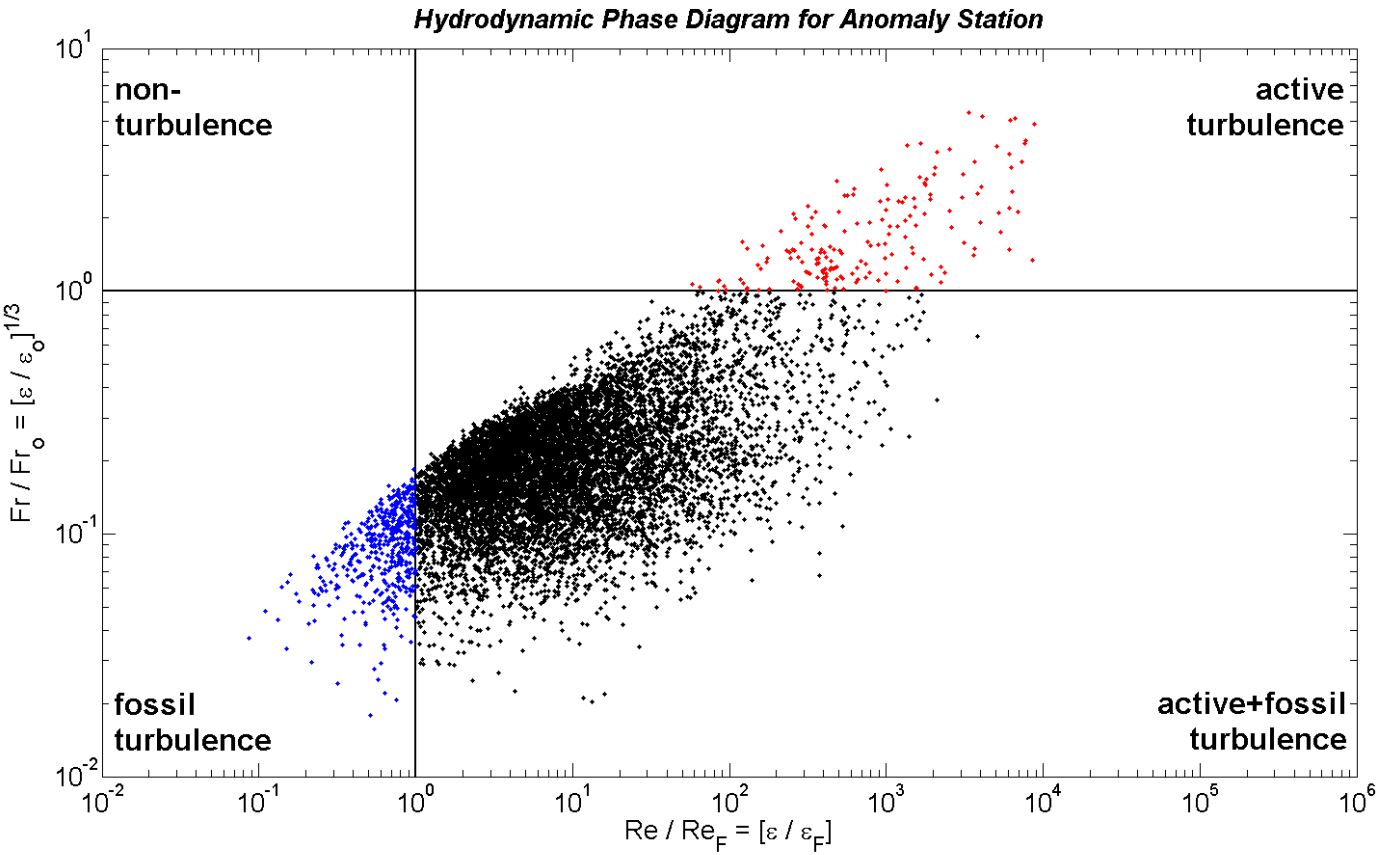

Figure 33. Hydrodynamic Phase Diagram for all patches observed at RASP 2004 Anomaly (M1) Station. Red dots indicate active patches. Black dots indicate active+fossil patches. Blue dots indicate fossilized patches.

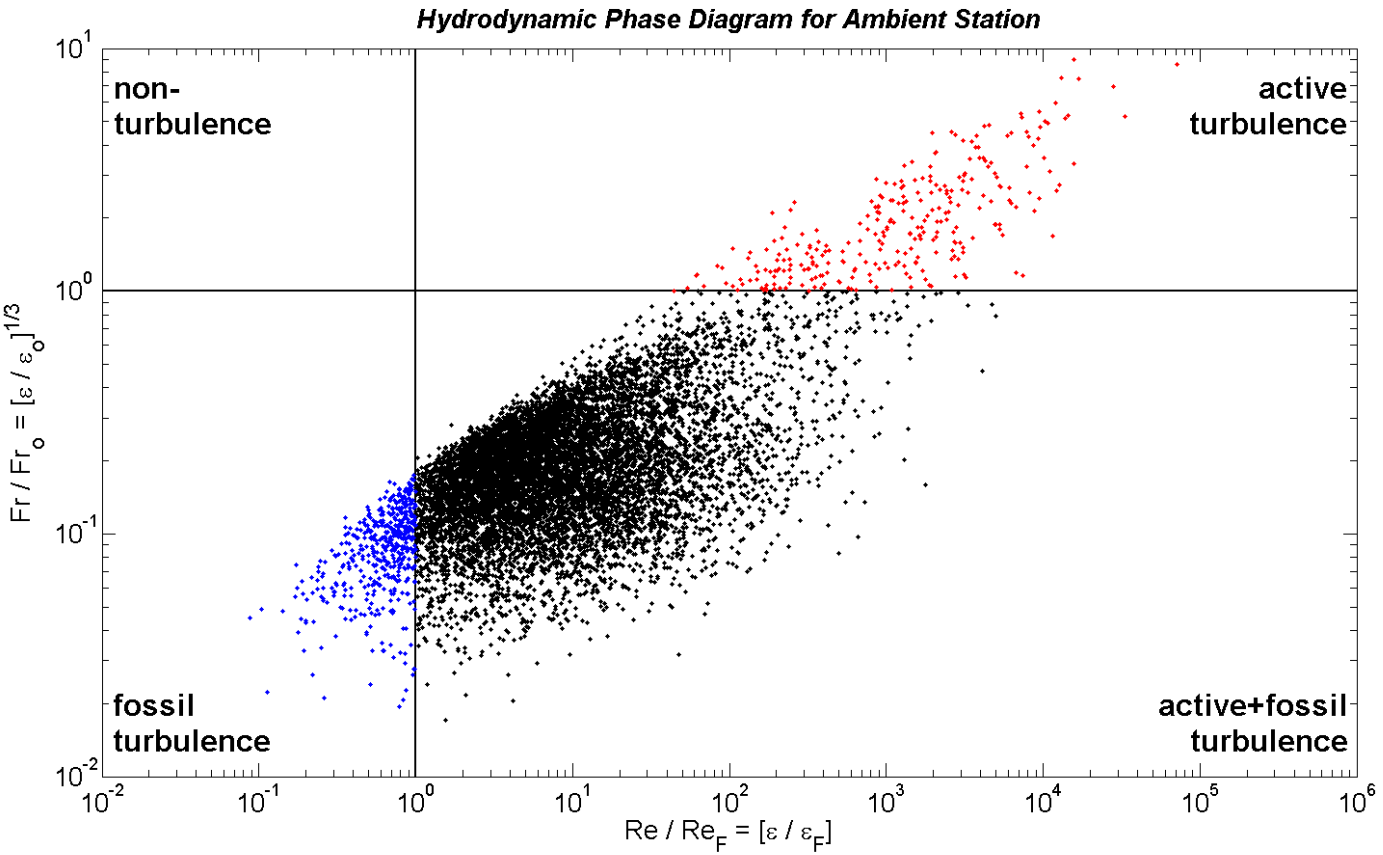

Figure 34. Hydrodynamic Phase Diagram for all patches observed at RASP 2004 Ambient (M2) Station. Red dots indicate active patches. Black dots indicate active+fossil patches. Blue dots indicate fossilized patches.

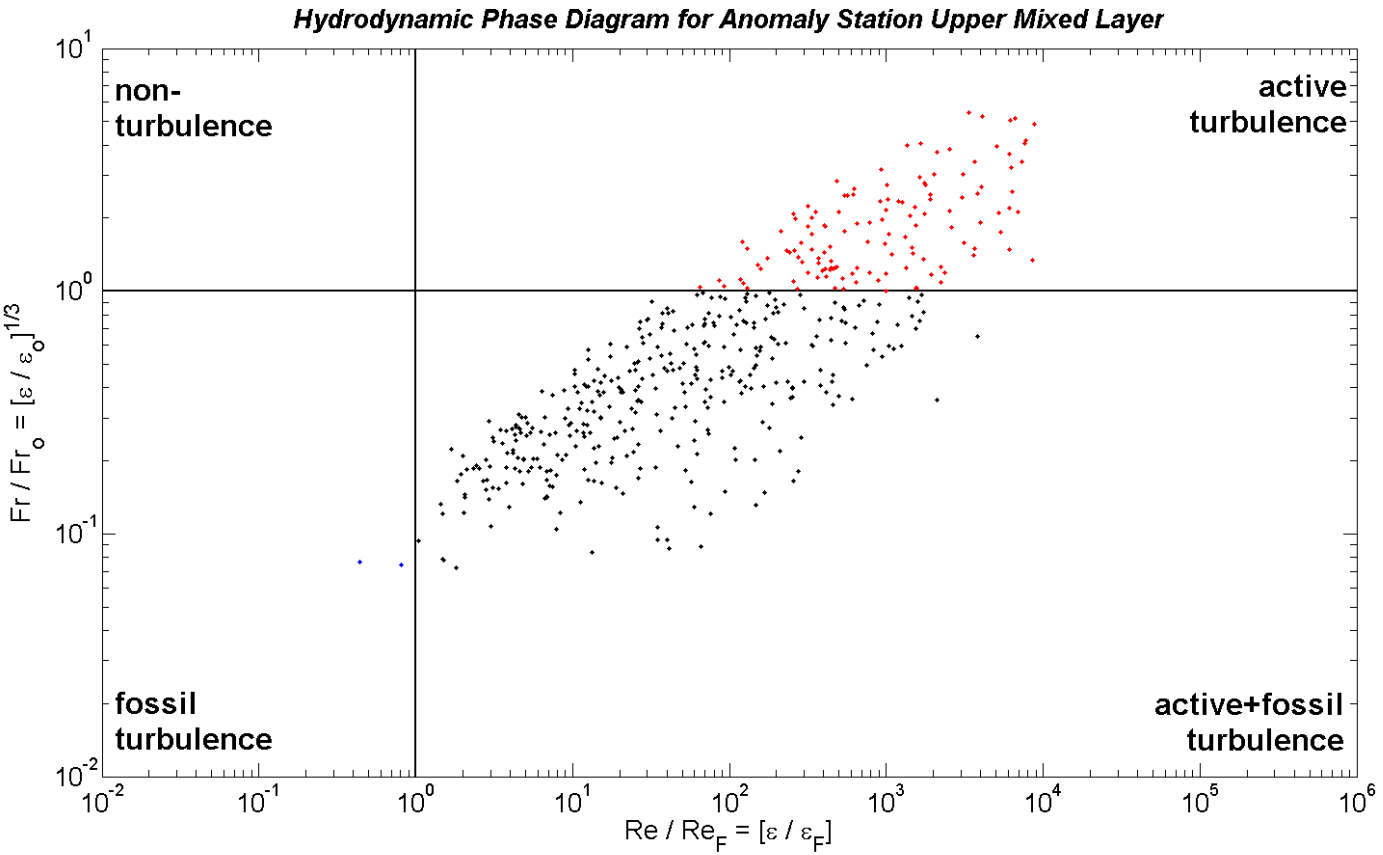

Figure 35. Hydrodynamic Phase Diagram for all patches observed Upper Mixed Layer at RASP 2004 Anomaly (M1) Station. Red dots indicate active patches. Black dots indicate active+fossil patches. Blue dots indicate fossilized patches.

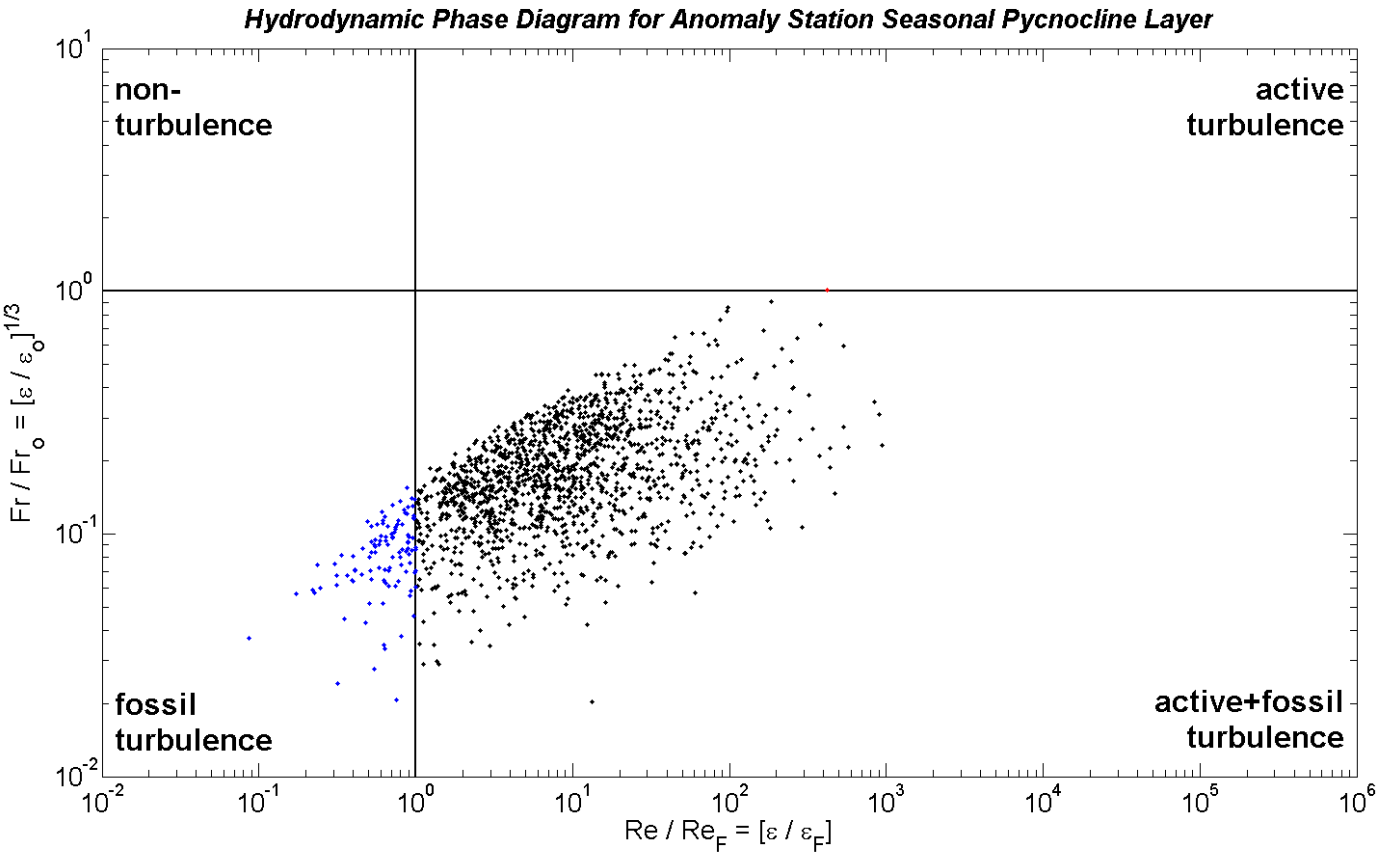

Figure 36. Hydrodynamic Phase Diagram for all patches observed Seasonal Pycnocline Layer at RASP 2004 Anomaly (M1) Station. Red dots indicate active patches. Black dots indicate active+fossil patches. Blue dots indicate fossilized patches.

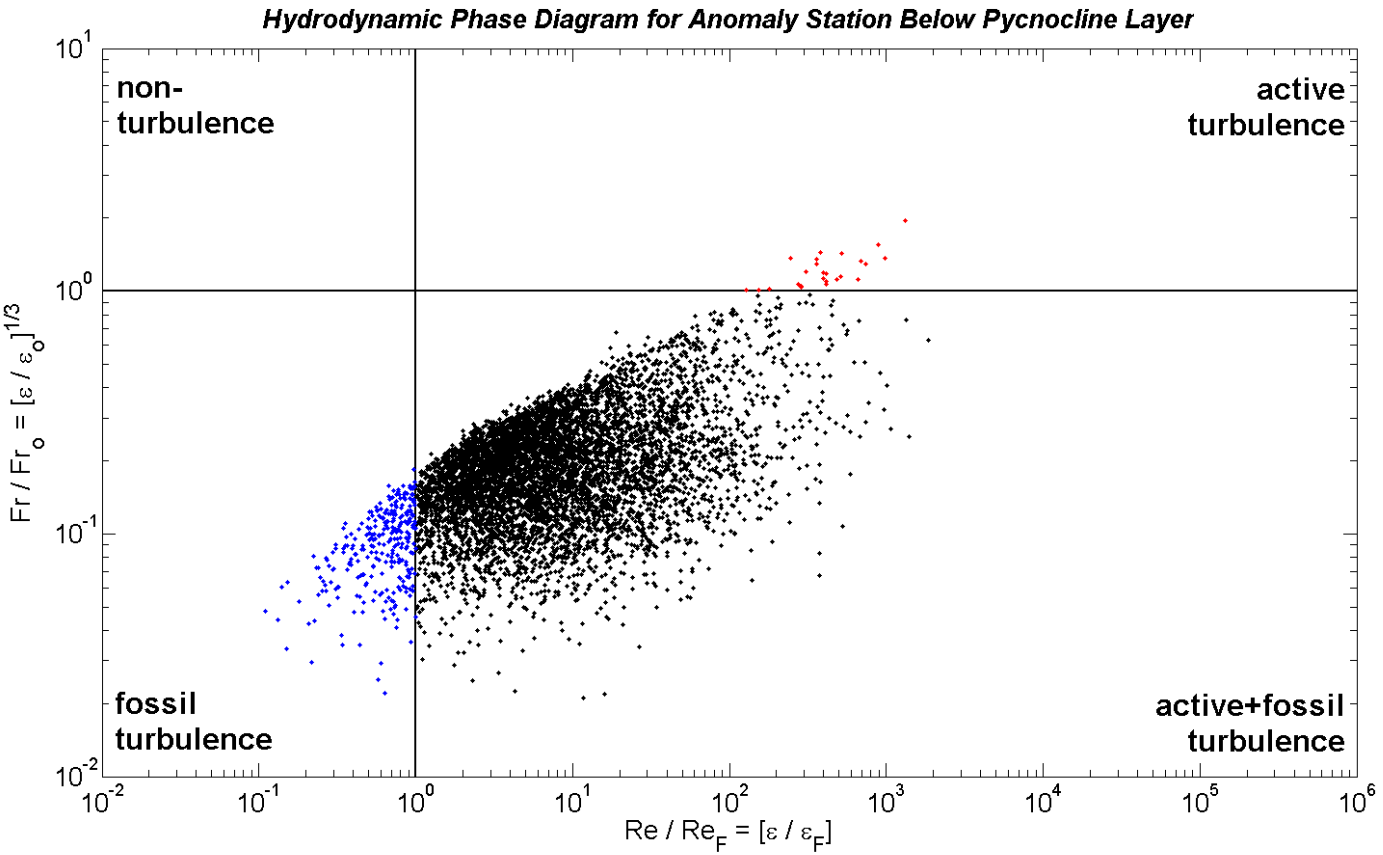

Figure 37. Hydrodynamic Phase Diagram for all patches Below Pycnocline Layer at RASP 2004 Anomaly (M1) Station. Red dots indicate active patches. Black dots indicate active+fossil patches. Blue dots indicate fossilized patches.

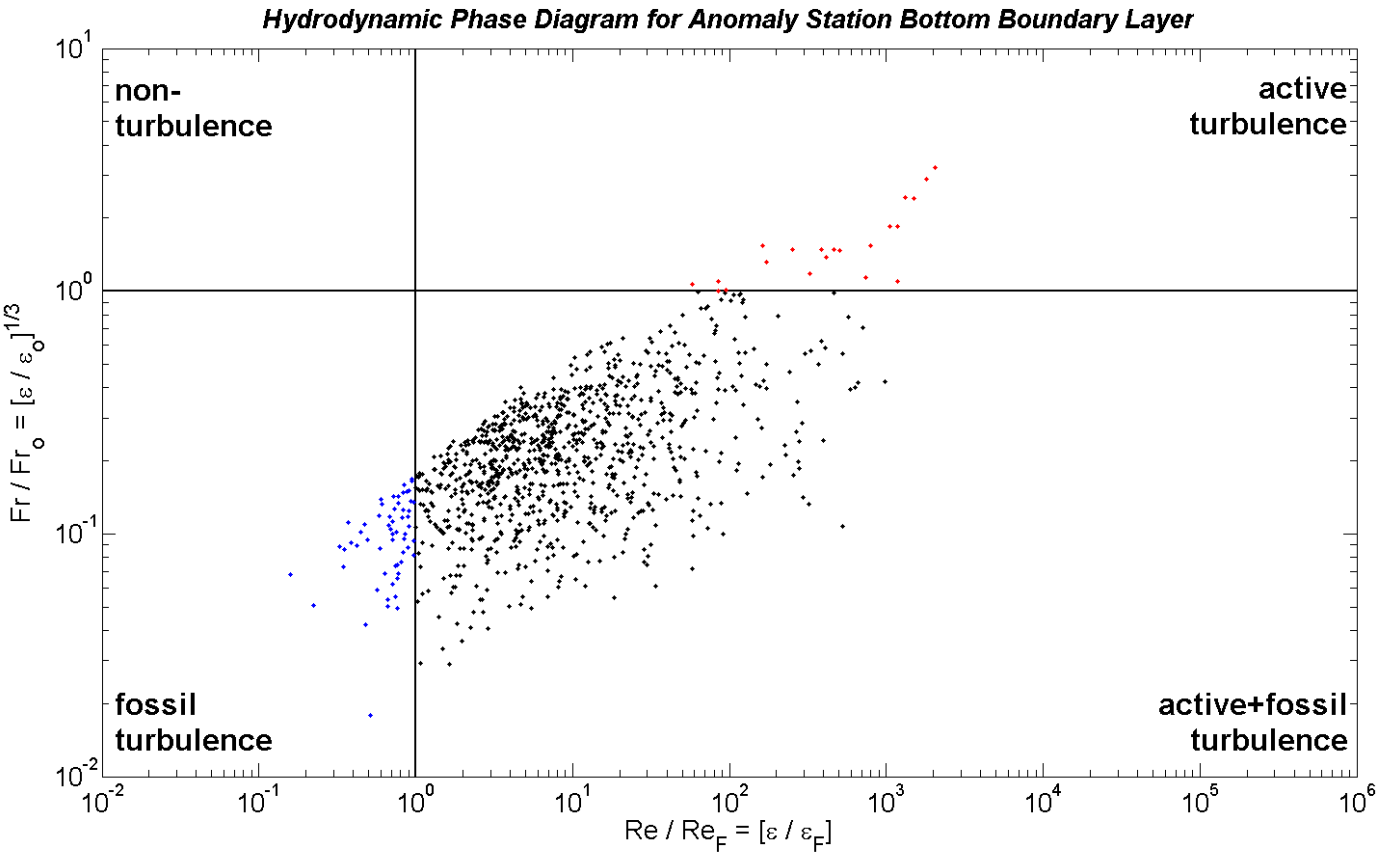

Figure 38. Hydrodynamic Phase Diagram for all patches at observed Bottom Boundary Layer at RASP 2004 Anomaly (M1) Station. Red dots indicate active patches. Black dots indicate active+fossil patches. Blue dots indicate fossilized patches.

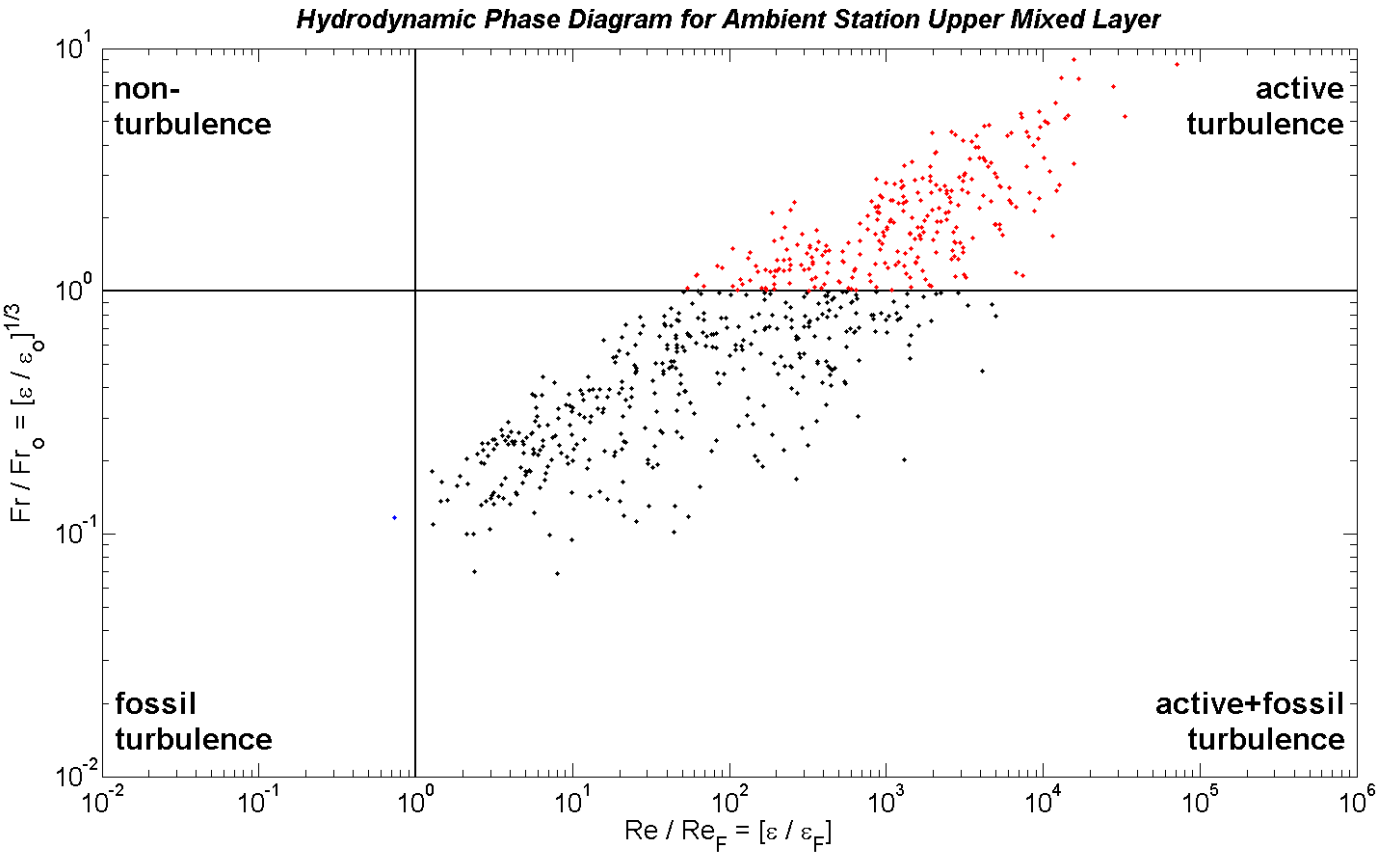

Figure 39. Hydrodynamic Phase Diagram for all patches observed in the Upper Mixed Layer at RASP 2004 Ambient (M2) Station. Red dots indicate active patches. Black dots indicate active+fossil patches. Blue dots indicate fossilized patches.

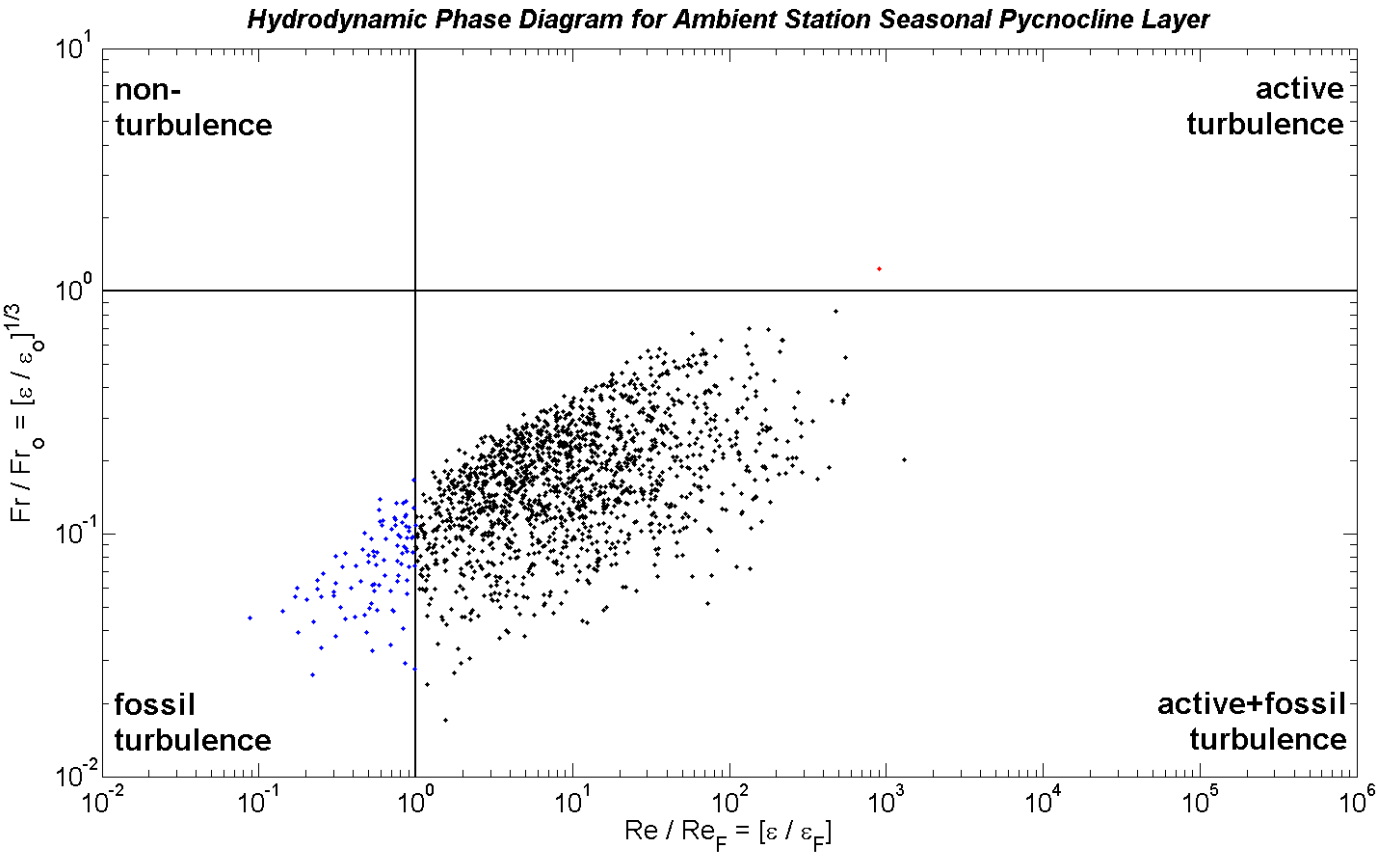

Figure 40. Hydrodynamic Phase Diagram for all patches observed in the Seasonal Pycnocline Layer at RASP 2004 Ambient (M2) Station. Red dots indicate active patches. Black dots indicate active+fossil patches. Blue dots indicate fossilized patches.

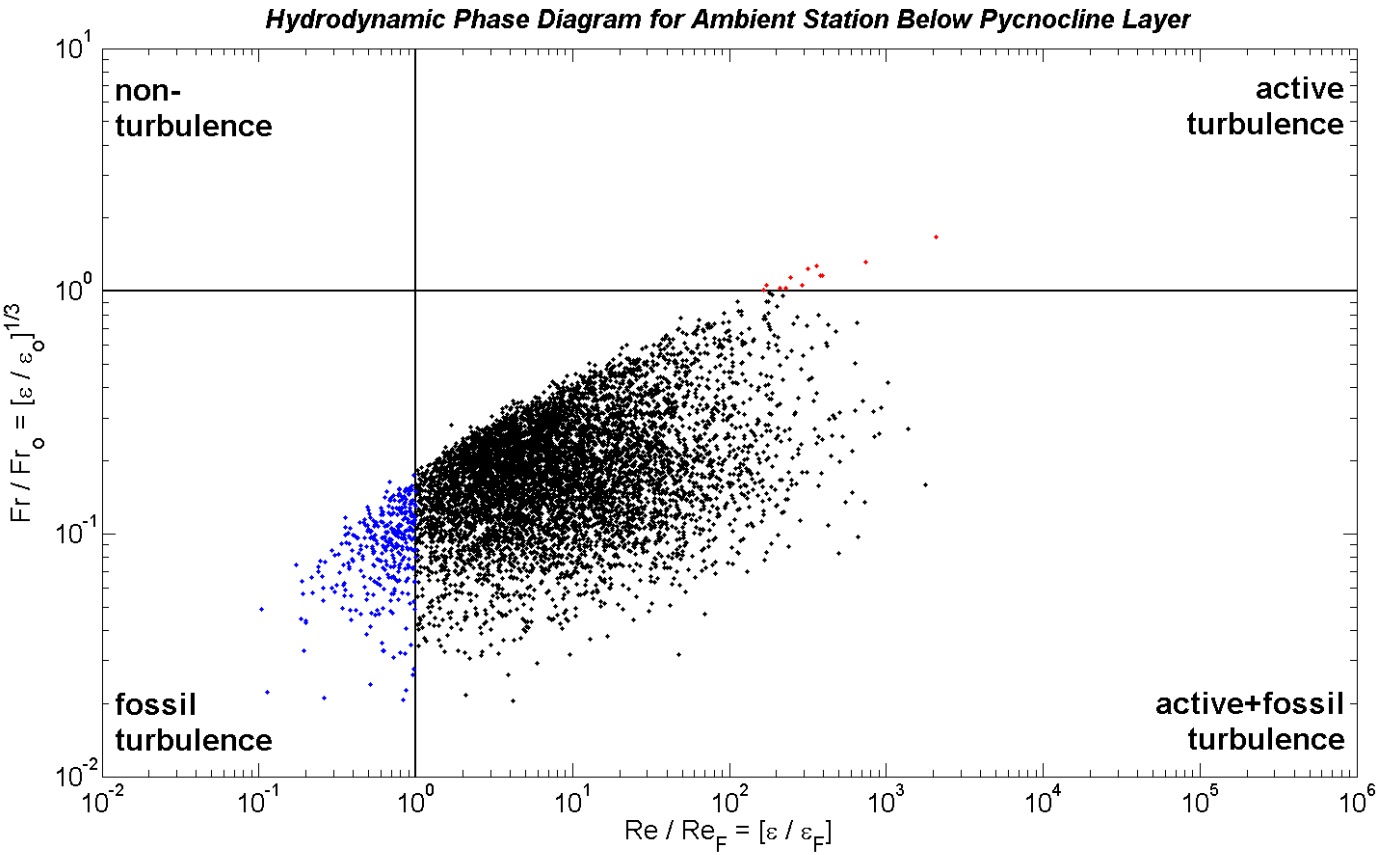

Figure 41. Hydrodynamic Phase Diagram for all patches observed in the Below Pycnocline Layer at RASP 2004 Ambient (M2) Station. Red dots indicate active patches. Black dots indicate active+fossil patches. Blue dots indicate fossilized patches.

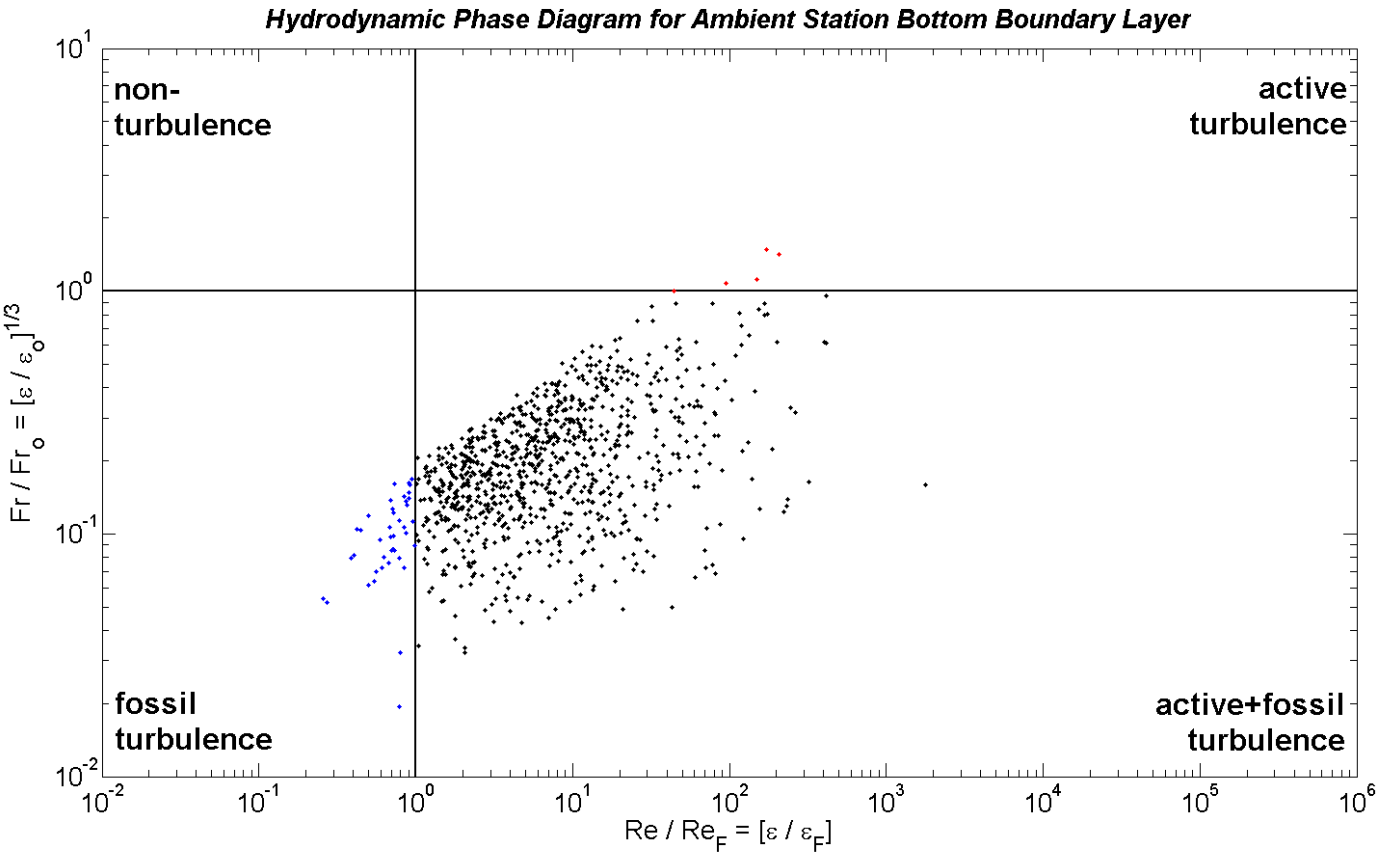

Figure 42. Hydrodynamic Phase Diagram for all patches observed in the Bottom Boundary Layer at RASP 2004 Ambient (M2) Station. Red dots indicate active patches. Black dots indicate active+fossil patches. Blue dots indicate fossilized patches.

3.3 Discussion

Seventy years ago, *Sverdrup et al.* [1942] asserted that most of the ocean is turbulent. With the advancement of technology and understanding of turbulence, the presented HPDs show that approximately 2% of the observed patches are active overturns (2.5% for both stations, 2.9% for ambient, and 1.8% for anomaly). Active patches are found in the surface and bottom boundary layers, which are the typical energetic "hot zones" for marine turbulence generation. On the other hand, approximately 5% of the identified patches are fossilized (4.8% for both stations, 4.7% for ambient, and 4.8% for anomaly). They are patches damped by buoyancy and viscosity with small length scale and relatively small dissipation rate. Even though they appear to be microstructures in vertical profiles, they are scalar features without corresponding velocity structures. From this study it is clear that there are more fossil patches than active patches in the water column under typical conditions.

The rest of the water column is dominated by active+fossil patches that are responsible for the mixing in the water column (Figure 43). Active+fossil is a phase of patch decay unique to stratified fluids in which the overturn is inhibited by buoyancy. Rather than collapsing and disappearing without a trace, buoyancy turbulence patches generated from the "hot zones" are damped out by buoyancy rapidly while their length scales are preserved. Because they can persist for a relatively long period of time, they would disperse over the water column until the neutral density layer is reached. This process contributes to the column’s mixing. These patches will further decay as they advect and are eventually damped out by viscosity. Microstructure studies that are focused on mixing "hot zones" often report smaller vertical diffusivities than those inferred from flow models (this phenomena is sometimes referred to as the "dark mixing" paradox). It is suggested that unobserved mixing events must occur somewhere in the ocean to explain how the ocean is mixed. This study shows that the majority of the

mixing is not missing but rather ignored when it occurs in the interior instead of the boundaries of the ocean. Many marine datasets should be reinterpreted by taking the fossilization effects and consequent undersampling implications into account. Serious undersampling errors will lead to underestimates of intermittency factors, turbulent diffusivities, and scalar dissipation rates from those datasets.

Length scales of the evolving patches can be studied from Figure 43. Active and fossil patches are generally smaller in vertical scale than the active+fossil patches regardless of depth (mixing regions). This agrees with laboratory studies done by *Fernado* [2003] on evolution of patch sizes and supports the model of increasing length cascade during the early stage of turbulence in stratified fluid. Turbulence is generated at the surface by winds and in bottom boundary layers by friction. Active patches require a relatively small scale (Kolmogorov scale) to overturn freely without the influence of any damping forces. The patches grow in size by eddy paring and reach Ozmidov scale as they drift toward the interior of the column [*Leung and Gibson*, 2004]. Buoyancy will then become dominant and inhibit the patches from overturning and they enter the active+fossil phase of patch decay. The patches continue to decay until they are small enough to be damped out by viscosity and become fossilized. This mechanism can be identified by the 1/3 decay slope on the overall HPD cluster as observed by other studies [*Lozovatsky and Erofeev*, 1994; *Gibson*, 1999].

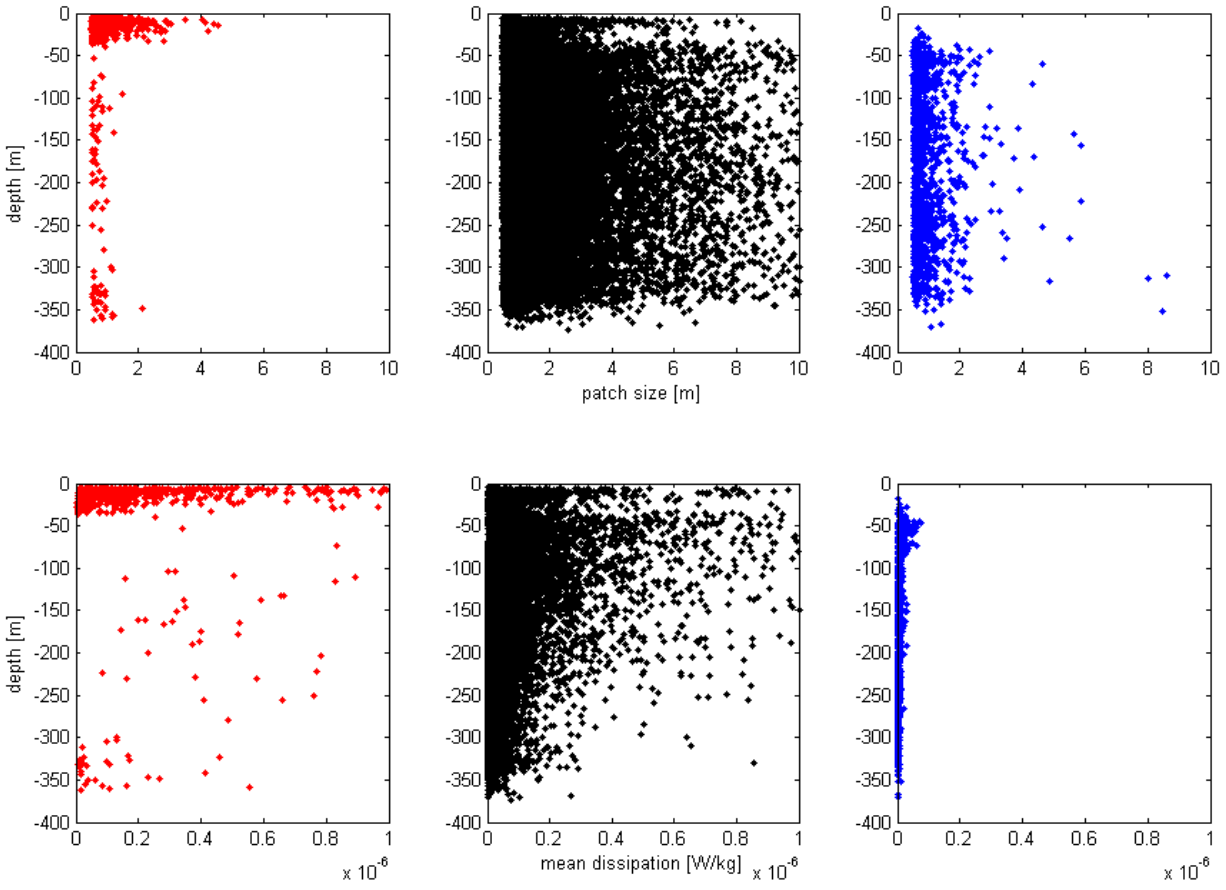

Figure 43. Patch size (top row) and mean patch dissipation rate (bottom row) versus depth. Red dots (left column) indicate active patches. Black dots indicate active+fossil patches (middle column). Blue dots indicate fossilized patches (right column).

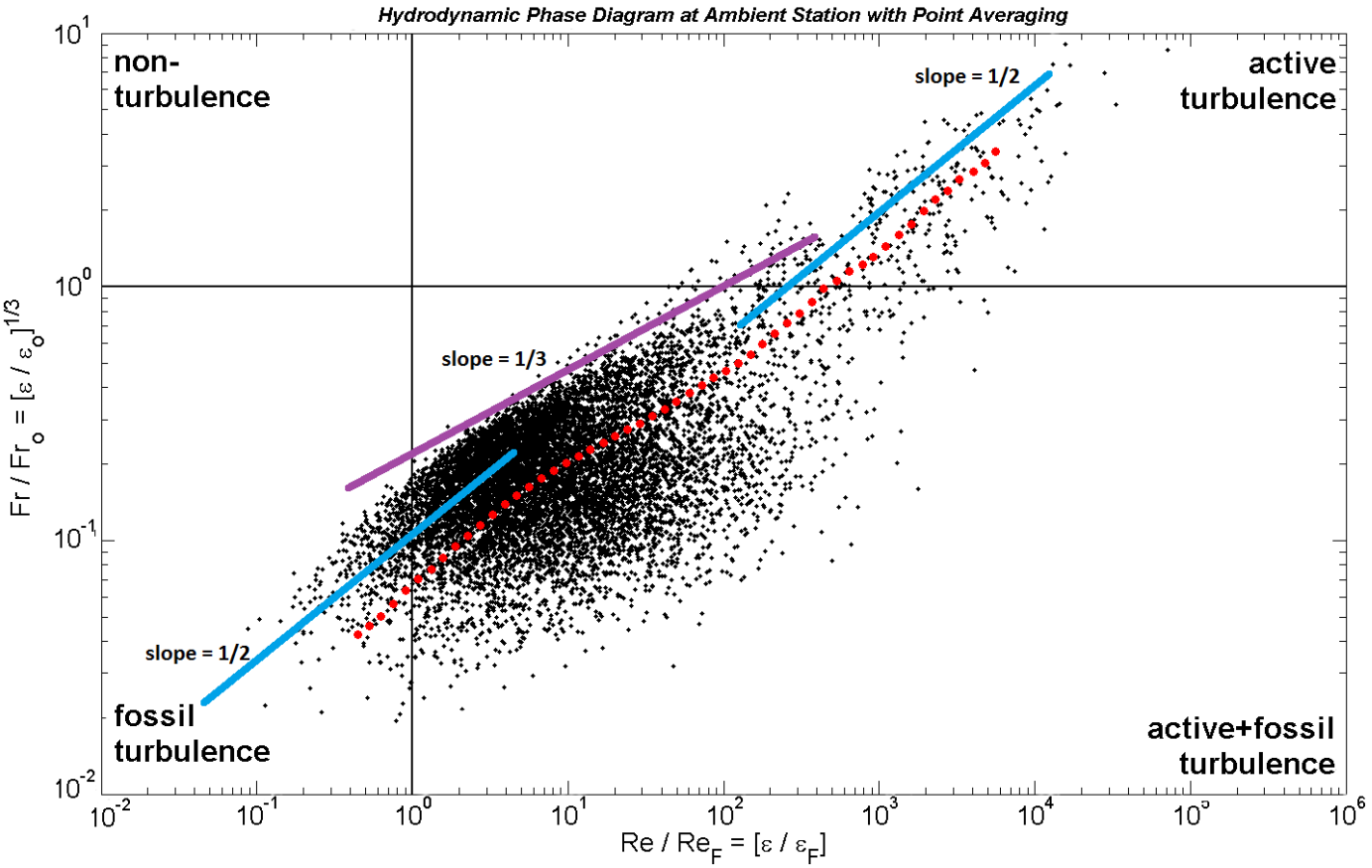

Figure 44. Hydrodynamic Phase Diagram of data collected from Ambient Station (M2) with equal probability averaging data points (red dots), which is the arithmetic averaging of HPD points in 50 segments of the data. The 1/3 Gibson-slope (purple) indicates the evolution of turbulent patches predicted by the Fossil Turbulence Theory. The 1/2 slopes (blue), during the active to active+fossil and active+fossil to fossil transitions, indicate the involvement of additional mechanism at those stages.

To better characterize the scattered cloud of HPD points, equal-probability averaging (arithmetic averaging of HPD points in 50 segments of the data) is used to study the tendency of Fr/Fr_o and Re/Re_F values. *Gibson* [1980] proposed those points should follow a decay line with slope of 1/3 on the HPD. The 1/3 slope is bounded by the physical limitation of patch decay in which $\varepsilon_o = \varepsilon_F$. The slope indicates the normalized Froude number (Equation 7) is equal to the normalized Reynolds number (Equation 8) and hence the patch is in the buoyancy-inertial-viscous balance (Table 1). *Lozovatsky et al*. [2005] investigated the characteristic of the decay slope with data collected from Black Sea shallow waters and found that the HPD cluster is bounded by the 1/3 slope, and the averaged data follow the 1/3 slope only during and after fossilization. That study concluded the importance of other, yet to be found, governing parameters in determining the decay process. The major differences between Lozovatsky's study and RASP are water depth and the type of mixing event dominating the region. For the former, the water is shallow (17 to 30 m) and wind mixing is the dominant source in the region. This can be seen in the HPD of that dataset [Figure 4 in *Lozovatsky*, 2005] where a majority of the patches are in the active and fossil stages with only a few are active+fossil. Its HPD cluster is located in higher Fr/Fr_o values indicating a more active mixing event.

For RASP, data are collected from 350 m water columns in which patches are allowed to fully develop and decay. The effect of wind forcing only penetrates the first ~30m of the column, and so wind mixing is not the dominant process. The equal-probability averaged HPD data of RASP (Figure 44) can be separated into three segments: the transition from active to active+fossil stage, active+fossil stage, and the active+fossil to fossil stage. The first and last segments follow closely on the 1/2 slope whereas the active+fossil segment follows the 1/3 slope. This result agrees with Gibson's prediction on patch decay when buoyancy effect is dominant. Other parameters or mechanisms may have contributed to the 1/2 slope observed in the other phases of the process.

One of the most widely used approaches to estimating the mixing efficiency (Γ) is based on the *Osborn-Cox* [1972] model:

$$\Gamma = K\epsilon/N^2 \tag{11}$$

where K is the eddy diffusivity, ε is kinetic energy dissipation rate, and N is buoyancy frequency. Patches at fossilized stages are the most efficient by definition because of the relatively low ε values. It is the ratio between available potential energy (APE) to kinetic energy (KE) dissipation [*Oakey*, 1982]. However, the problem with this approach is that both K and ε are often regarded as tunable parameters whose values can be adjusted to produce the desired results. For example, *Munk* [1966] concluded that a value of $K = 10^{-4}$ m^2/s was needed to explain the observed thermocline structure and mixing in the Pacific. On the other hand, *Kunze et al.* [2006] followed the "standard practice" and used Γ = 0.2 [*Osborn*, 1980] to estimate K in Saanich Inlet, British Columbia. This practice introduces a wide range of uncertainty to the mixing efficiency value. Other approaches are proposed to eliminate the need of K to estimate Γ. *Gregg and Horne* [2009] proposed the upper bound for Γ can be estimated from using

$$\Gamma = \frac{\nabla PE}{\nabla KE} = \frac{(N^2 L_T^2)/2}{(2\pi\varepsilon)/N} = \frac{1}{4\pi}\frac{L_T^2}{\varepsilon/N^3} = \frac{1}{4\pi}\frac{L_T^2}{L_O^2} \tag{12}$$

where L_T is Thorpe Scale, L_O is Ozmidov scale, and π is the circumference to diameter ratio. The estimated values of Γ from RASP 2004 by Equation 12 are summarized in Table 15.

Table 15. Estimated values of mixing efficiency at the ambient and anomaly stations.

Vertical Zone	M1 (anomaly)	M2 (ambient)
UP	0.14	0.08
SP	0.32	0.26
BP	1.09	0.87
BB	0.23	0.38

Time scale for the turbulent patches is given by

$$T = \sqrt[3]{L^2/\varepsilon} \tag{13}$$

where L is the length scale of the patch. A given patch with scale L would require T to decay. As a patch transits from active to fossil stages, its length scale increases and dissipation rate decreases, which in turn increases its time scale (Table 16). The mean decay time shows that the active+fossil and fossil patches persist about 4 and 5 times longer than the active patches respectively. This is the reason why the non-active patches are called "fossil turbulence". It is to denote their persistence long after the active patches were decayed.

Table 16. Time scale of patches in RASP 2004 at each phase of overturning.

	Active	Active+Fossil	Fossil
Mean Patch Size [m]	1.01	2.07	1.01
Mean Dissipation Rate [W/kg]	5.95E-07	6.56E-08	6.72E-09
Mean Decay Time [s]	119	403	533

This leads to a fine-tuned version of ocean mixing theory with the idea of fossil turbulence: active patches in the "hot zones" start the mixing process by initial stirring. The vector microstructures (overturns) will then rapidly evolve into scalar microstructures (active+fossil and fossil patches) by ambient damping. The influence of buoyancy and viscosity increases when the patches enter the later stages of decay. Hence, the mixing efficiency increases and the irreversible process of mixing is completed by diffusion. It is therefore more efficient to stir coffee with a spoon than a straw because larger overturns will generate larger scalar gradient which allows the optimal conditions for diffusion. From this description and the presented HPDs, it is clear that "hot zones" are only responsible for stirring while most mixing in the ocean happens throughout the water column. As seen from the non-1/3-slope of the HPD

clusters, there are other mechanisms, such as the collapse of Kelvin-Helmholtz billows or breaking internal waves that contribute to the overall mixing events at the active and fossil phases.

Wijesekera and Dillon [1997] proposed the ratio of Ozmidov scale to Thorpe scale, R_{OT}, can be used as an indicator of patch age. R_{OT} of patches identified from RASP is summarized in Table 17.

Table 17. Ratio of Ozmidov scale to Thorpe scale (R_{OT}) for all patches identified from RASP 2004 data.

Patches	Active	Active+Fossil	Fossil
R_{OT}	1.31	0.45	0.10

Fossil turbulence theory [*Gibson*, 1980] predicts that R_{OT} decreases from O(1) to less than 1 as the patches evolve from active to fossil. However, *Wijesekera and Dillion* [1997] use Shannon entropy to argue that as the mixing patch ages R_{OT} should increase from less than 1 to larger than O(1). They suggest those "events are not fossils but seem to be very young rather than very old" and should be referred to as "natal turbulence". *Smyth et al.* [2001] further suggest $R_{OT} \sim 0.5$ during the transition phase, which matches R_{OT} during the active+fossil phase of the RASP dataset.

It is important to note that *Wijesekera and Dillion* [1997] also suggest that it is possible for some classes of overturns to start from largest R_{OT} and decrease as they advect downstream. For example, grid-generated turbulence would have greatest R_{OT} just behind the grid because ε is largest there. This scenario supports the hypothesis that overturns are generated by stirring on the ocean boundary and advect to the interior. R_{OT} values from each station and vertical zone are presented in Table 18. The largest R_{OT} occurs on the surface (UP) and lowest in the interior of the water column (BP - below pycnocline layer). The bottom boundary layers (BB) also have relatively high values of

R_{OT} . In other words, R_{OT} decreases as the overturns advect to the interior. With *Wijesekera and Dillion*'s explanation [1997] on grid-generated turbulence and decreasing R_{OT}, it can be argued that the active stirring on the ocean boundary would create similar effects on the water column as a grid on stratified flow [*Stillinger et al.,* 1983; *Itsweire et al.*, 1986; *Xu et al,*. 1995].

Table 18. Ratio of Ozmidov scale to Thorpe scale (R_{OT}) for different vertical zones and measurement stations during RASP 2004.

Vertical Zone	M1 (anomaly)	M2 (ambient)
UP	0.78	1.04
SP	0.51	0.57
BP	0.28	0.31
BB	0.60	0.47

One motivation of this study was to investigate the existence of oceanic fossil turbulence by using Hydrodynamic Phase Diagram on the RASP dataset. The result agrees with the fossil turbulence theory's prediction and similar investigations (e.g. *Lozovatsky and Erofeev*, 1994; *Folkard et al.*, 2007). However, it is beyond the scope of this study to settle the 30-year debate between the two schools of thought on the evolution of turbulent patch (best summarized by *Caldwell* [1983] and *Gibson* [1987b]).

The first published use of the term "fossil turbulence" [*Woods*, 1969] was to denote the extensive volumes of small scale refractive index fluctuation apparently associated with clear air turbulence. A workshop on fossil turbulence was organized at the Colloquium on Spectra of Meteorological Variables, Stockholm, in June 1969 chaired by Woods. The panel report from the Colloquium concluded that fossil turbulence is frozen into a stationary fluid and evolves only by molecular diffusion. The presented RASP 2004 result shows evidence of such turbulence in the ocean, which is a scalar structure with weak velocity fluctuation and has high mixing efficiency due to molecular diffusion.

CHAPTER IV
DISCUSSION, CONCLUSIONS AND RECOMMENDATIONS

Based on the fossil turbulence theory and the hydrodynamic phase diagram (HPD) technique, microstructure near a sea-floor outfall diffuser in Sand Island, Hawaii was studied. The results provided an improved understanding of mixing processes in the ocean. The observed buoyancy-driven turbulence undergoes the following evolution stages as proposed by fossil turbulence theory:

1. Active (overturning) turbulence grows in length scale until it becomes limited by background buoyancy (i.e. Ozmidov scale). The overturning motion will then be inhabited.

2. When overturning halts, the kinetic structure gets progressively smaller in scale (collapsing) leading to complete dissipation.

3. At the same time, the scalar structure remains and becomes "fossilized" at the largest scales allowed by the buoyancy structure. These fossil (non-overturning) patches cause mixing by diffusion.

From the field data collected, this research study confirms that the observed buoyancy-driven turbulence follows the above evolution pathway. In addition, the data also show that elevated dissipation rates from point 2 above are found in the seasonal pycnocline and the bottom boundary layer near the diffuser (anomaly station).

By using the HPD technique, the analysis shows that most (> 90%) of the turbulent patches observed in the water column are inactive (not overturning). The analysis also shows the change in patch sizes at different stages of the evolution. Active patches increase in length scales before they become limited by buoyancy (step 1

above). Active+fossil patches (i.e. transitioning from point 2 above to point 3) move to successively smaller scales as the kinetic structure devolves, consistent with previous lab studies.

4.1 Discussion

The presented data are consistent with turbulence studies in the laboratory and in numerical modeling that show clear indications of the fossilization mechanism. Data collected from RASP show that 92% of observed patches are damped by buoyancy, leading to, non-active overturns. The percentage of non-active patches in the water column depends on the environmental conditions, local stratification, and the source of turbulence. However, this result shows that not all temperature structure obtained from vertical profiles are overturning patches. The 1/3 decay slope proposed by the fossil turbulence theory [*Gibson*, 1980] is confirmed both by the upper bound of the HPD cluster and the characteristic slope of HPDs with data from the RASP. It is clear that the active turbulence is limited by $Fr/Fr_o = 1$ and fossilization begins at $Re/Re_F = 1$. However, the ½ slope observed during the phase transitions suggests that other mechanisms may also play a role in patch decay (Figure 44).

The growth of turbulent patches is also studied from this dataset. Active and fossil patches have smaller length scales than the active+fossil patches (as shown in Figure 29 and Figure 43). This suggests that turbulence patches cascade from small scale to larger scale at early stages of patch evolution. The patches will then become fossilized and collapse. This result agrees with observations from laboratory stratified fluids [*Fernando*, 1988, 2003]. The initial increase of patch size is unaffected by the stratification, but as it grows to a certain size (Ozmidov scale), the buoyancy becomes dominant and suppresses the vertical growth.

The mixing efficiency (Γ) is defined as the ratio between available potential energy by molecular diffusion and the total dissipation rate of kinetic energy. It has a

suggested value of 0.2 [*Gregg et al.*, 1986; *Itsweire et al.*, 1993; *Moum*, 1996a] based on observations and experiments without considering the fossil turbulence mechanism. This study shows that the majority of mixing occurs in the active+fossil and fossil stages. The term “turbulence mixing” can be misleading, since the irreversible mixing process starts from turbulence stirring and ends with molecular diffusion. Surface and bottom layers of the water column were believed to be the source region for ocean mixing. However, the majority of the actual ocean mixing happens in the interior of the water column when molecular diffusion occurs in scalar microstructures.

The observed values generally agree with the theoretical values proposed by *Osborn* [1980]. The mixing efficiency is the lowest in the surface layer and as previously explained, the active patches initiate the mixing processes by mechanical stirring. Turbulent patches advect and the mixing processes are completed by diffusion in the interior of the water column. Mixing efficiencies in the seasonal pycnocline are very close to the theoretical value of 0.2. However, only 0.1% of patches in that layer are active. This shows that ocean mixing is not done by active overturns. The relationship between non-active patches and mixing becomes more defined in the below pycnocline layer, which has the highest number (> 6500) of non-active (active+fossil and fossil) patches and the highest mixing efficiency. It is a clear indication that mixing occurs in the interior of the ocean instead of the boundary. For the bottom boundary layers, the mixing efficiency is again closer to the theoretical value of 0.2 where most of the ocean mixing observation was done. (Note that 0.2 is not a universal value for ocean mixing, however, it provides a good reference when comparing with the "standard practice" employed by most oceanographers.)

With the existing definition, it is possible for Γ to be larger than one in the water column. This is because the current mixing models allow the incompressible and Boussinseq approximations with a linear equation of state of seawater [*Tailleux*, 2008]. *Tailleux* [2009] pointed out that a parameter ξ ,which is less than one but can also be negative [*Fofonoff*, 1998, 2001], should be introduced to the mixing efficiency estimation:

$$\Gamma = \xi \frac{\nabla PE}{\nabla KE} \tag{14}$$

The presented results support this argument and provide evidence for the need to re-examine published values of Γ with consideration of the fossil mechanism and gravitational potential energy that is ignored by linear approximations.

Turbulence plays an essential role in planetary heat, mass, and momentum transfer processes. However, sampling turbulence parameters such as dissipation rates and diffusivities is complicated due to the enormous range of length scales and time scales involved. Undersampling errors are likely if not inevitable. Similar to the contribution of Einstein's work to the classical mechanics, fossil turbulence offers a more sophisticated view of the stirring and mixing processes. Fossil turbulence parameters can be useful as a means of evaluating the completeness of a given data set to minimize such errors. Evidence of previous turbulence activity which may not be represented by the available data can be revealed from the fossilized patches. Further laboratory and field studies of fossil turbulence may permit more efficient and possibly more reliable inferences of space-time average turbulence properties in stratified flows and ultimately lead to the development of hydropaleontology.

4.2 Conclusion

This research provides an improved understanding of turbulent mixing in the ocean by classifying patches into three evolution stages: active (overturning), active+fossil (intermediate), and fossil (buoyancy-inhibited). Because of the self-similarity nature of turbulence, fossil turbulence should exist in all disciplines of fluid dynamics including oceanography. Data collected from this study shows that not all observed physical structures are active overturns and not all mixing is done by overturning patches. Fossil turbulence patches exist in the ocean in the same way as in atmosphere and other fluid bodies.

In conclusion, the findings of this study are:

1. Field Data collected near a sea-floor outfall diffuser show that turbulent patches evolve from active (overturning) to fossil (buoyancy-inhibited) stages, consistent with the process of turbulent patch evolution proposed by fossil turbulence theory.

2. The data show that active (overturning) and fossil (buoyancy-inhibited) patches have smaller length scales than the active+fossil (intermediate) stage of patch evolution, consistent with fossil turbulence theory and with laboratory studies.

3. Compared to a far-field reference, elevated dissipation rates near the diffuser were found in the seasonal pycnocline as well as in the bottom boundary layer.

4. More than 90% of the turbulent patches observed in the water column were non-overturning (active+fossil and fossil). Such patches can provide significant mixing in the interior of the ocean, far from surface and bottom boundary layers.

4.3 Future Work

4.3.1 Internal Waves Generated and Radiated from the Outfall Diffuser

One hypothesized mechanism to explain the observed higher dissipation rates in the seasonal pycnocline and the bottom boundary layer in the anomaly area is internal waves radiated from the near field of the diffuser into the anomaly area.

RASP 2004 measurement campaign was not designed to investigate the existence of narrowband internal waves generated by the diffuser jet; however, it still provides evidence of these waves and information for a hypothesis. A possible internal wave mechanism is proposed here to explain the observed differences of turbulence intensity between anomaly and ambient stations (Figure 45). This internal wave mechanism may

also explain the surface anomaly signatures identified by the satellite imagery. In the near field, the sewage from the diffuser mixes with the ambient seawater. Buoyancy forces and strong turbulence are generated from the density difference. The sewage water plume, driven by buoyancy, rises until it reaches the trapping depth. The actual trapping depth depends on the sewage density and local stratification which vary with time. Buoyancy forces within the rising sewage plume are then converted to internal wave energy and propagated along the pycnocline. This mechanism is observed to have a frequency comparable with the local buoyancy frequency by *Roberts et al.* [2002] at the Boston outfall. The internal waves propagating in the pycnocline increase the shear in this layer, which results in the observed higher level of turbulence in the anomaly station's seasonal pycnocline. It is known that propagating internal waves can generate surface anomalies by stretching and pinching the sea surface due to momentum transfer or direct interaction.

The model of internal waves generated by decaying turbulent patches is another possible mechanism that occurs in the near field. Such turbulence generated waves area a topic of discussion in the oceanographic community and demonstrated by different studies [*Sutherland et al*., 2004]. The internal waves generated by the diffuser jets can propagate in the pycnocline away from the diffuser or can be radiated to the bottom. This is similar to the internal waves generated at the continental slope [*Pound and Pickard*, 1983]. When the turbulence-generated internal waves encounters a bottom slope and critically reflected, its width will be compressed, wavelength reduced, energy amplified upon reflection. This results in enhanced turbulence mixing at the slope [*Kunze and Llewellyn Smith*, 2004]. The strong near bottom turbulence observed in the near field of the diffuser is the result of interaction. This process explains the higher dissipation rates measured in the bottom boundary layer at the anomaly station compared to the ambient station. When the turbulence-generated internal waves radiate from the diffuser jets at near-vertical (between 40^o to 60^o), they generate surface anomalies similar to the mechanism caused by the buoyancy-generated internal waves.

The applications and results of HPD need to be further examined. It is necessary to further develop the HPD technique into a robust procedure for patch classification. Data collected from the RASP provided some exciting results on the usage of HPDs to identify and classify overturn eddies using vertical profiles. Nonetheless, further studies are required to relate the hydrodynamic evolution to the overall hydrographical condition.

Evolution of eddies can be studied in laboratory with controlled turbulence sources, such as oscillating grids or submerged jets. By varying the Reynolds and Froude numbers of the flows, laboratory studies will provide a wide range of HPD points corresponding to different strengths of turbulence sources and understand the significance of the decay slope during different stages of decay. Future field observations should also be made to compare the laboratory results with marine and limnic environment. How will the eddies evolve under weak stratification, as buoyancy force plays such an important role in fossilization? What is the proper time scale from overturn to collapse? Future studies should continue to investigate the evolution of decaying turbulent patches. Based on the experience and result from these studies, it is suggested that the microstructure instrumentation needs to be improved in future experiments to test the eddy evolution model.

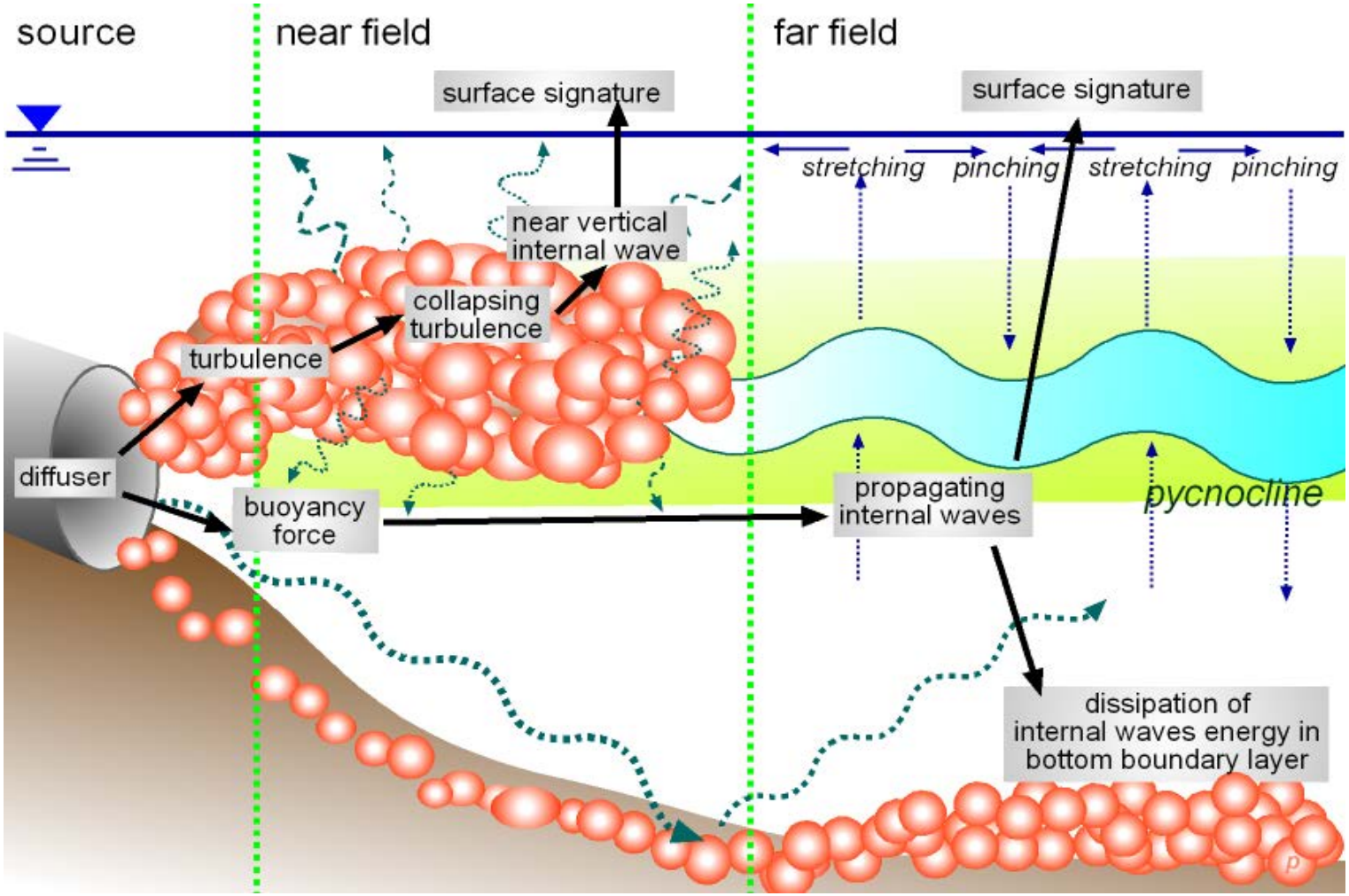

Figure 45. Sketch of the hypothesized internal wave mechanism derived from RASP 2004 microstructure investigation.

4.3.2 Future Field Measurement Improvements

Microstructures are fine scale physical fluctuations in the fluid body. High frequency sensors are capable of measuring such structures, but the free sinking nature of profiling makes it impossible to observe the dynamics of the turbulent patch evolution. Depending on the conditions, it can take up to 15 minutes to obtain a 350 m profile. Such profiles are often treated as ‘snapshots’ of the water column, but strictly speaking, this assumption is wrong. It is not possible for the profiler to measure more than one point of the column at any given moment. This often resulted in the assumption that all eddy like structures are active overturns and all non-active patches will collapse and disappear without a trace. Improved vertical profilers are needed to obtain simultaneous multiple-point measurements to provide a complete picture of patch decay.

Future studies should include profilers with multiple microstructure sensors arranged in a two dimensional array. Micro-thermistors, like FP-07 with response time of 10 ms, are often used in microstructure studies. It can easily be retrofitted into a 4 x 4 array of with 5 cm or less spatial resolution. Horizontal sections can then be measured as the profiler pass through the turbulent patches (Figure 46). Profiling can only provide quick looks of the water column but is impractical when monitoring long term or high frequency variations. A mooring mounted with current meters, standard CTDs, and micro-temperature sensors is recommended for future coastal buoyancy turbulence. Sensors can be mounted at each depth level of interest (pycnocline, bottom boundary layers, etc) to measure the microstructure of that specific layer. The WAVESCAN buoy on the surface is a wave directional buoy measuring waves, meteorological, and environmental parameters. Data from the mounted instruments can be transferred and stored on the buoy’s internal hard drive unit. The mooring can stay on site for months with minimal maintenance.

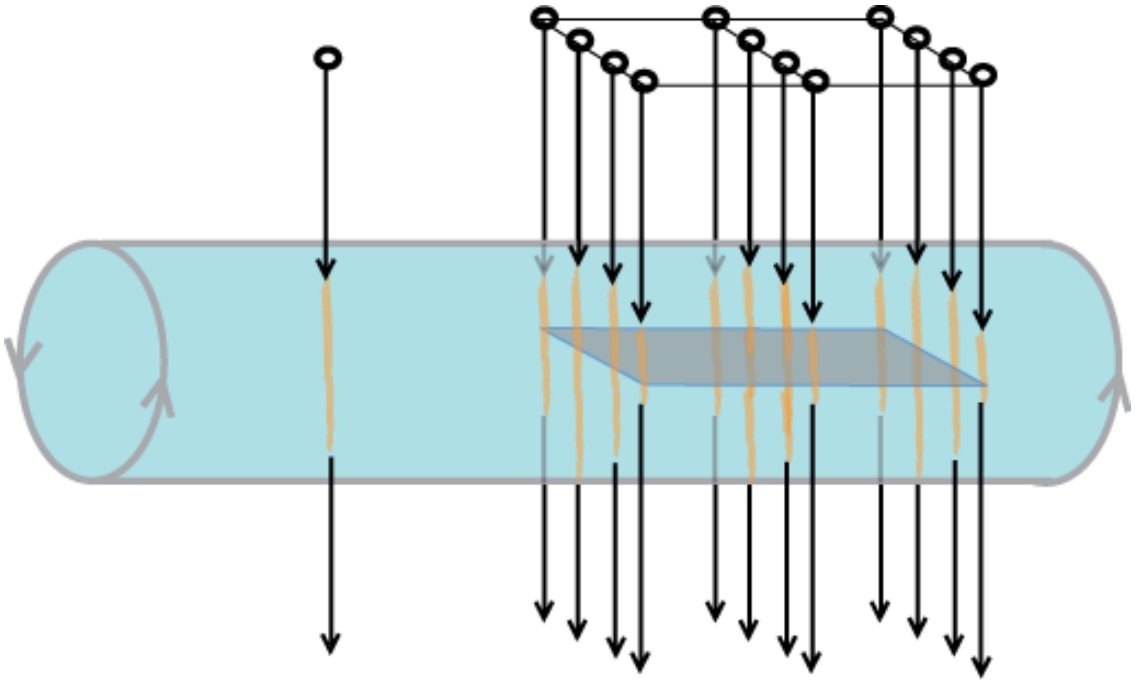

Figure 46. Profile with a single temperature sensor (left) can only provide 1-dimensional information of as it passes through the overturn where as an array of sensors (right) will be able to provide a cross-sectional snap shot of the eddy.

4.3.3 Future Application of Fossil Turbulence Detection

As discussed in the previous section, fossil turbulence is the remnant of a turbulence event when the eddies fail to overturn due to the buoyancy or other damping forces. Active eddies are damped out rapidly by external forces, whereas the non-overturn eddies collapse immediately and diffuse, only the active+fossil stage of the eddy can persist for a time scale much longer than the other two stages and make observation possible. For that reason, majority of the observed turbulence events are neither overturning nor collapsing. This argument is supported by the HPD analysis from field observations. Unfortunately, most turbulence studies only consider the active stage and the collapsing stage of the turbulence events, while the active+fossil stage is overlooked or simply ignored.

Marine animals have long incorporated the detection of the remnant of turbulence into their predatory instincts. For example, harbor seals Henry and Nick from a German study demonstrated their ability to follow a turbulent trail. Even blind-folded, the seals can quickly locate a toy submarine even after it passed through a pool. More amazing is the seals are able to follow the exact path of the toy submarine even minutes after the toy has been removed. The study concluded that their whiskers are responsible for the detection of turbulent trails created by swimming prey [*Wieskotten et al.*, 2010]. Other studies conducted on different species of fish concluded that they can detect the "footprint" left behind by their prey with the lateral-line sensory organs [*Franosch et al.*, 2003; *Gardiner and Atema*, 2007]. Studies [e.g. *Hanke et al.*, 2000; *Hanke and Bleckmann*, 2004] show that such footprints are “the ageing low-frequency water disturbances” and often puzzled by their long period of persistence.

If turbulence eddies dissipate and collapse immediately without a trace how could Henry and Nick follow the exact patch of the toy submarine even after it is removed from the tank? The answer is fossil turbulence. The active eddies generated by the toy submarine are rapidly damped by the buoyancy or any other forces. Instead of overturning, the eddies will enter the “bobbing mode” and preserve length scale and structure for a relatively long period of time before being damped out and collapsing. The active+fossil eddies stayed in the fluid long enough to provide Henry and Nick a trail of the submarine. The trail of the pre-existing turbulence may seem like a new concept to oceanographers, however, biological evolution has developed sensory organs in marine animals specifically for this task.

The idea of fossil turbulence was first introduced in the radio communication community as a possible inference to radio signal [*Woods*, 1969]. It is a widely accepted phenomenon in other aspects of fluid dynamical studies, such as atmospheric science [*Koch et al.*, 2005] and astrophysics [*Basse*, 2008]. The effects of the remanent turbulence in those disciplines are well published and considered. However, it is still a relatively new concept in marine science. The understanding of fossil turbulence mechanism will allow accurate estimation of the mixing efficiency and new focus on

ocean interior mixing investigation. Such knowledge can also be used on submerged turbulence detection in anti-submarine warfare, deepwater ecosystem studies, and remote detection of subsurface phenomena such as topographic features and freshwater or hydrocarbon plumes.

REFERENCES

Alford, M. H., M. C. Gerg, and M. A. Merrifield (2006), Structure, propagation and mixing of energetic baroclinic tides in Mamala Bay, Oahu, Hawaii, *Journal of Physical Oceanography*, *36*, 997-1018.

Baker, M.A. and C. H. Gibson (1987), Sampling turbulence in a stratified ocean: statistical consequences of strong intermittency, *J. of Physical Oceanography*, *17*, 1817-1837.

Basse, N. P. (2008), A study of multiscale density fluctuation measurements, *IEEE Transactions on Plasma Science*, *36*(2), 458-461.

Batchelor, G. (1996), *The Life and Legacy of G.I. Taylor*, Cambridge University Press, Cambridge, UK.

Baumert, H. Z, Simpson, J. H., and Sundermann, J.; Eds. (2005), *Marine Turbulence, Theories, Observations, and Models*, 630, Cambridge Univ. Press, Cambidge, UK.

Bondur, V. G. (2000), S*tudies in the Areas of Oceanology, Atmospheric Physics, Geography, Ecology, Ocean-related Problems, and Geocryology*, edited by Y. A. Israel, 254., Russ. Acad. of Sci., Moscow, Russia.

Bondur, V. G. (2004), Aerospace techniques in modern oceanology, *New Ideas in Oceanology Vol.1,* edited by M. E. Vinogradov and S. S. Lappo, 55 – 117, Nauka, Moscow, Russia.

Bondur, V. G. (2005), Complex satellite monitoring of coastal water areas, paper presented at 31st International Symposium on Remote Sensing of Environment, Nansen International Environmental and Remote Sensing Centre, Saint Petersburg, Russia.

Bondur, V. G., and N. N. Filatov (2003), Study of physical processes in coastal zone for detecting anthropogenic impact by means of remote sensing, paper presented at 7th Workshop on Physical Processes in Natural Waters, Inst. of Water Probl. of the N., Karelian Sci. Cent., Russ. Acad. of Sci., Petrozavodsk, Russia.

Bondur, V. G., and Y. V. Grebeniuk (2001), Remote indication of anthropogenic influences on marine environment caused by deep outfalls (in Russian), *Issled. Zemli Kosmosa*, *6*, 49-67.

Bondur, V. G., V. M. Zhurbas, and Y. V. Grebenuk (2009), Modeling and experimental research of turbulent jet propagation in the stratified environment of coastal water areas, *Oceanology*, 2009, *49*(5), 595–60.

Caldwell, D. R. (1983), Oceanic turbulence: Big bangs or continuous creation? *J. Geophys. Res., 88*, C12, 7543-7550.

Caldwell, D. R., T. M. Dillon, J. M. Brubaker, P. A. Newberger, and C. A. Paulson (1980), The scaling of vertical temperature gradient spectra, *J. Geophys. Res., 85*, 1917-1924.

Cloutman L. D. and R. W. Whitaker (1980), On convective and semiconvective mixing in massive stars, *The Astrophysical Journal*, *237*, 900-902.

Davidson, P. A. (2004), *Turbulence: An Introduction for Scientists and Engineers*, Oxford University Press, New York, NY, USA.

Dillon, T. M. (1982), Vertical overturns: A comparison of Thorpe and Ozmidov length scales, *J. Geophys. Res., 87*, 9601–9613.

Fernando, H. J. S. (1988), The growth of a turbulent patch in a stratified fluid, *J. Fluid Mech.,190*, 55-70.

Fernando, H. J. S. (2003), Turbulent patches in a stratified shear flow, *Physics of Fluid*, *15*(10), 3164-3169.

Feynman, R. P., R. B. Leighton, and M. Sands (1963), *The Feynman Lectures on Physics Vol. 1*, Addison–Wesley, Reading, MA, USA.

Fischer, H. B., E. J. List, R. C. Y. Koh, J. Imberger and N. H. Brooks (1979), *Mixing in Inland and Coastal Waters*, Academic Press, New York, NY, USA.

Fofonoff, N. P. (1998), Nonlinear limits to ocean thermal structure, *J. Mar. Res., 56*, 793–811.

Fofonoff, N. P. (2001), Thermal stability of the world ocean thermoclines, *J. Phys. Oceanogr., 31*, 2169-2177.

Folkard, A. M., A. J. Sherborne and Coates, and J. Michael (2007), Turbulence and stratification in Priest Pot, a productive pond in a sheltered environment, *Limnology*, *8*(2), 113-120.

Franosch, J. M., M. C. Sobotka, A. Elepfandt, J. L. van Hemmen (2003), Minimal model of prey localization through the lateral-line system., *Phys Rev Lett.*, 2003 Oct 10, *91*(15):158101.

Frisch, U (1995), *Turbulence: The Legacy of A. N. Kolmogorov*, Cambridge University Press, Cambridge, UK.

Gamov, G. (1954), On the formation of protogalaxies in the turbulent primordial gas, *Proc. Nat. Acad. Sci., 40*, 480-484.

Gardiner, M. and J. Atema (2007), Sharks need the lateral line to locate odor sources: Rheotaxis and eddy Chemotaxis. *The Journal of Experimental Biology, 210,* 1925-1934, doi:10.1242/jeb.000075.

Gargett, A. E., T. R. Osborn, and P. W. Nasmyth (1984), Local isotropy and the decay of turbulence in a stratified fluid. *J. Fluid Mech., 144*, 231-280.

Gerz T. and H. Yamazaki (1993), Direct Numerical Simulation of Buoyancy-Driven Turbulence in Stably Stratified Fluid, *J. Fluid Mech., 249*, 415-440.

Gibson, C. H. (1980), Fossil temperatures, salinity, and vorticity turbulence in the ocean, in *Marine Turbulence* edited by J. C. J. Nihoul, Elevier, Amsterdam, 221-257.

Gibson, C. H. (1986), Internal waves, fossil turbulence, and composite ocean microstructure spectra, *J. Fluid Mech, 168*, 89-117.

Gibson, C. H. (1987a), Fossil turbulence and intermittency in sampling oceanic mixing processes, *J. Geophys.*, Res. *92*, 5383-5404.

Gibson, C. H. (1987b), Oceanic turbulence: Big bangs and continuous creation, *J. Physicochem. Hydrodyn.*, *8*(1), 1-22.

Gibson, C. H. (1991), Fossil two-dimension turbulence in the ocean, in *Turbulent Shear Flows*, 7, edited by F. Durst and W. C. Reynolds, 63-78, Springer-Verlag, Berlin.

Gibson, C. H. (1996), Turbulence in the ocean, atmosphere, galaxy and universe, *Applied Mechanics Reviews, 49*, 299-316, astro-ph/9904260.

Gibson, C. H. (1999), Fossil turbulence revisited, *J. of Marine Systems, 21*(1-4), 147-167, astro-ph/9904237.

Gibson, C. H., and W. H. Swartz (1963), Detection of conductivity fluctuations in a turbulent flow field, *J.Fluid Mech., 144*, 357-364.

Gibson, C. H., V. Nabatov, and R. Ozmidov (1993), Measurements of turbulence and fossil turbulence near Ampere seamount, *Dynamics of Atmospheres and Oceans, 19,* 175-204.

Gloor, M. (1995), *Methode der Temperaturmikrostruktur und deren Anwendung auf die Bodengrenzschicht in geschichteten Wasserkorpern*, unpublished Ph.D. dissertation, Eidgenossiche Technische Hochschule, Zurich.

Gourlay, M. G., S. C. Arendt, D. C. Fritts, and J. Werne (2001), Numerical modeling of initially turbulent wakes with net momentum, *Phys. Fluids*, *13*, 3783-3802.

Gregg, M. C., (1980), Zero crossings of temperature microstructure, *Marine Turbulence*, edited by J. C. J. Nihoul, 135–142, Elsevier, New York, NY, USA

Gregg, M. C. and J. K. Horne (2009), Turbulence, acoustic backscatter, and pelagic nekton in Monterey Bay, *J. Phys. Oceanogr.*, *39*, 1097–1114.

Gregg, M. C., E. A. D'Asaro, T. J. Shay, and N. Larson (1986), Observations of persistent mixing and near-intertial internal waves, *J. Phys. Oceanogr., 16,* 856-885.

Hanke, W. and H. Bleckmann (2004), The hydrodynamic trails of Lepomis gibbosus (Centrarchidae), Colomesus psittacus (Tetraodontidae) and Thysochromis ansorgii (Cichlidae) investigated with scanning particle image velocimetry, *J. Exp. Biol., 207*, 1585-1596.

Hanke, W., C. Brucker & H. Brucker (2000), The aging of the low-frequency water disturbances caused by swimming goldfish and its possible relevance to prey detection, *J. Exp. Biol.*, *203*, 1193–1200.

Imberger, J. and C. Boashash (1986), Application of the Wignerville distribution to temperature gradient microstructure: a new technique to study small-scale variations, *J. Phys. Oceanogr., 16*, 1997-2012.

Imberger, J. and G. N. Ivey (1991), On the nature of turbulence in a stratified fluid. Part 2: Application to lakes, *J. Phys. Oceanogr.*, *21*, 659-680.

Itsweire, E. C., K. N. Helland, and C W. Van Atta (1986), The evolution of grid-generated turbulence in a stably stratified fluid, *J. Fluid Mech., 162*, 299-338.

Itsweire, E. C., J. R. Kose, D. A. Briggs, and J. H. Ferziger (1993), Turbulence in stratified shear flows: Implications for interpreting shear-induced mixing in the ocean, *J. Phys. Oceanogr.*, *23*,1508-1522.

Ivey, G. N. and J. Imberger (1991), On the nature of turbulence in a stratified fluid. Part I: The energetics of mixing, *J. Phys. Oceanogr., 21,* 650-658.

Ivey, G. N., J. R. Kose, D. A. Briggs, and J. H. Ferziger (1992), Mixing in a stratified shear flow: Energetics and sampling, *Center for Turbulence Research, Annual Research Briefs*, 335-344.

Jones A. E., P. S. Anderson, E. W. Wolff, H. K. Roscoe, G. J. Marshall, A. Richter, N. Brough, and S. R. Colwell (2010). Vertical structure of Antarctic tropospheric ozone depletion events: Characteristics and broader implications, *Atmospheric Chemistry and Physics, 10,* 7775-7794, doi:10.5194/acp-10-7775-2010.

Keeler, R. N., V. G. Bondur, and C. H. Gibson (2005), Optical satellite imagery detection of internal wave effects from a submerged turbulent outfall in the stratified ocean, *Geophysical Research Letters, 32*, L12610.

Koch, S. E., B. D. Jamison, C. Lu, T. L. Smith, E. I. Tollerud, N. Wang, T. Lane, M. Shapiro, D. D. Parrishand O. R. Cooper (2005), Turbulence and gravity waves within an upper-level front, *Journal of the Atmospheric Sciences, 62*(11), 3885-3908, doi:10.1175/JAS3574.1.

Kocsis O., H. Prandke, A. Stips, A. Simon, and A. Wuest (1999), Comparison of dissipation of turbulent kinetic energy determined from shear and temperature microstructure, *Journal of Marine Systems, 21,* 67-84.

Koh, Robert C. Y. and N. H. Brooks (1975), Fluid mechanics of waste water disposal in the ocean. *Annual Review of Fluid Mechanics, 7*, 187-211. ISSN 0066-4189.

Kolmogorov, A. N. (1941), The local structure of turbulence in incompressible viscous fluid for very large Reynolds numbers. Dokl. Akad. Nauk SSSR, *30*, 301-305.

Kunze, E. and S.G. Llewellyn Smith (2004), The role of small-scale topography in turbulent mixing of the global ocean, *Oceanography, 17*, 1, 55-64.

Kunze, E., J. F. Dower, I. Beveridge, R. Dewey and K. P. Bartlett (2006), Observations of biologically generated turbulence in a coastal inlet, *Science, 313*, 1768-1770.

Leung, P. T. and C. H. Gibson (2004), Turbulence and fossil turbulence in oceans and lakes, *Chinese Journal of Oceanology and Limnology, 22*, 1–23, astro-ph/0110248/published.

Libby, Paul A. (1996), *Introduction to Turbulence,* Taylor and Francis, Bristol, PA, USA.

Lozovatsky, I. D. and A. Y. Erofeev (1994), Marine turbulence in the coastal zone, paper presented at Oceans '94, IEEE, Brest, France.

Lozovatsky, I. D., R. Elena, and H. J. S. Fernado (2005), Mixing in shallow waters: Measurements, processing, and applications, *Journal of Ocean University of China (Oceanic and Coastal Sea Research)*, *4*(4), 293-305.

Luketina, D. A. and J. Imberger (1989), Turbulence and entrainment in a buoyant surface plume, *J. Geophys. Res.*, *94* (C9), 12619-12636.

Moum, J. N. (1996a), Efficiency of mixing in the main thermocline, *J. Geophys. Res.*, *101*, 12 057–12 069.

Moum, J. N. (1996b), Energy-containing scales of turbulence in the ocean thermocline, *J. Geophys. Res.*, *101*, 14 095–14 109.

Munk, W. (1966), Abyssal recipes, *Deep-Sea Res.*, *13*, 207–230.

Oakey, N. S. (1982), Determination of the rate of dissipation of turbulent energy from simultaneous temperature and velocity shear microstructure measurements, *J. Phys. Oceanogr.*, *12*, 256-271.

Osborn, T. R. (1980), Estimates of the local rate of vertical diffusion from dissipation measurements, *J. Phys. Oceanogr.*, *10*, 83–89, 1980.

Osborn, T. R. and C.S. Cox (1972), Oceanic fine structure, *Geophys. Fluid Dyn.*, *3*, 321-345.

Ozmidov, R. V. (1965), Energy distribution between oceanic motions of different scales, *Atmos. Ocean. Phys.*, *1*, 493–497.

Paka, V. M., V. N. Nabatov, I. D. Lozovatsky, and T. M. Dillon (1999), Oceanic microstructure measurements by BAKLAN and GRIF, *J. Atmos. Ocean. Technol.*, *16*, 1519-1532.

Peters H., M. C. Gregg, and J. M. Toole (1988), On the parameterization of equatorial turbulence, *J. of Geophys. Res.*, *93*, 1199-1218.

Pope, S. (2000), *Turbulent Flows*, Cambridge University Press, Cambridge, UK.

Pound, S. and G. L. Pickard (1983), *Introductory Dynamical Oceanography*, Pergamon Press, Burlington, MA, USA.

Prandke, H. (1994), *Test and inter-calibrations of an improved airfoil shear probe, Technical Report*, April 1994, ME Meerestechnik-Elektronik GmbH, Trappenkamp, Germany.

Prandke, H. and A. Stips (1992), A model of Baltic thermocline turbulence patches, deduced from experimental investigations, *Cont. Shelf Res.*, *12*, 643–659.

Prandke, H. and A. Stips (1998a), Test measurements with an operational microstructure-turbulence profiler: Detection limit of dissipation rates, *Aquatic Sciences*, *60*, 191-209.

Prandke, H. and A. Stips (1998b), Microstructure profiler to study mixing and turbulent transport processes, paper presented at OCEANS´98, IEEE, Nice, France.

Riley J.J. and S. J. DeBruynKops (2003), Dynamics of turbulence strongly influenced by buoyancy, *Phys. Fluids*, *15*, 2047, doi:10.1063/1.1578077.

Roberts, P. J. W. (1999), Modeling Mamala Bay outfall plumes. I: Near field, *J. Hydr. Eng.*, 564-573.

Roberts, P. J. W., C. D. Hunt, M. J. Michelsen (2002), Field and model studies of the Boston outfall, paper presented at 2nd International Conference on Marine Waste Water Discharges MWWD 2002, IEMES, Istanbul, Turkey.

Rotter J., H. J. S. Fernando, and E. Kit (2007), Evolution of a forced stratified mixing layer, *Phys. Fluids*, *19*, 065107, doi:10.1063/1.2740305.

Ruggiero, F. H. (2007), Characterization of high altitude turbulence for air force platforms, paper presented at HPCMP Users Group Conference 2007, IEEE, Pittsburgh, PA, USA.

Seim, H. E., and M. C. Gregg (1994), Detailed observations of a naturally-occurring shear instability, *J. Geophys. Res.*, *99*, 10049–10074.

Shen, Z., Y. P. Li, G. X. Chui, and Z. S. Zhang (2009), Large eddy simulation of stably stratified turbulence, *Science China Physics, Mechanics, & Astronomy*, *53*(1), 135-146, doi: 10.1007/s11433-010-0113-2.

Smyth, W. D. and J. N. Moum (2000), Length scales of turbulence in stably stratified mixing layers, *Phys. Fluids*, *12*, 1327-1342.

Stewart, R. W. (1969), Turbulence and waves in a stratified atmosphere, *Radio Science*, *4*(12), 1269-1278.

Stillinger, D. C., K. N. Helland, and C. W. Van Atta (1983), Experiments on the transition of homogeneous turbulence to internal waves in a stratified fluid, *J. Fluid Mech., 131*, 91-122.

Sutherland, B.R., M. R. Flynn, and K. Dohan (2004), Internal wave excitation from collapsing mixed region. *Deep-Sea Research II, 51*, 2889-2904.

Sverdrup, H. U., M. W. Johnson and R. H. Fleming (1942), *The Oceans, Their Physics, Chemistry, and General Biology*, Prentice Hall, Inc., Englewood Cliffs, NJ, USA.

Tailleux, R. (2008), Understanding mixing efficiency in the oceans: Do the nonlinearities of the equation of state for seawater matter? *Ocean Sciences, 5*, 285-291.

Tailleux, R. (2009), On the energetics of stratified turbulent mixing, irreversible thermodynamics, Boussinesq models, and the ocean heat engine controversy, *J. Fluid Mech., 638*, 339-382.

Taylor G. I. (1919), Tidal friction in the Irish Sea, *Philos. Trans. Roy. Soc. London*, 220A, 1– 93.

Tennekes, H. and J. L. Lumley (1972), *A First Course in Turbulence*, The MIT Press, Cambridge, MA, USA.

Thorpe, S. A. (1977), Turbulence and mixing in a Scottish loch, *Philos. Trans. Roy. Soc. London*, 286A, 125–181.

Turner, J. S. (1973), *Buoyancy Effects in Fluids*, Cambridge University Press, New York, NY, USA.

Vernin J. (2000), Mechanism of formation of optical turbulence, paper presented at 112th ASP Annual Meeting, Astronomical Society of the Pacific, Pasandena, CA, USA.

Wieskotten, S., G. Dehnhardt, B. Mauck, L. Miersch, and W. Hanke (2010), Hydrodynamic determination of the moving direction of an artificial fin by a harbour seal (Phoca vitulina), *Journal of Experimental Biology, 213*, 2194-2200.

Wijesekera, H. W. and T. M. Dillon (1997), Shannon entropy as an indicator of age for turbulent overturns in the oceanic thermocline, *J. Geophys. Res., 102* (C2), 3279-3291.

Winters, K. B. and E. A. D'Asaro (1996), Diascalar flux and the rate of fluid mixing, *J. Fluid Mech., 317*, 179-193.

Winters, K. B., P. N. Lombard, J. J. Riley, and E. A. D' Asaro (1995), Available potential energy and mixing in density stratified fluids, *J. Fluid Mech., 289*, 115-128.

Woods, J. D. (1969), Fossil turbulence, *Radio Science, 4*(12), 1365-1367.

Xu, Y., H. J. S. Fernando, and D. Boyer (1995), Turbulent wakes of stratified flows past a cylinder, *Phys. Fluids, 7*, 2243-2255.

VITA

Name: Pak Tao Leung

Address: Department of Oceanography,
MS 3146, Texas A&M University
College Station, TX 77843.

Email: ptleung@tamu.edu / ptleung@gmail.com

Education:

- Ph.D. in Physical Oceanography, Texas A&M University (2011)
- M.S. in Mechanical Engineering (Fluid Mechanics), University of California, San Diego (2002)
- B.S. in Mechanical Engineering, University of California, San Diego (1999)
- B.A. in General Physics, University of California, San Diego (1999)

Selected Publications:

Gibson, C. H., V. G. Bondur, R. N. Keeler, P. T. Leung (2008), Energetics of the beamed zombie turbulence maser action mechanism for remote detection of submerged oceanic turbulence, *Journal of Applied Fluid Mechanics*, *1*(1), 11-42.

Gibson, C. H., R. N. Keeler, V. G. Bondur, P. T. Leung, H. Prandke, D. Vithanage (2007), Submerged turbulence detection with optical satellites, *SPIE Optics + Photonics 2007 Coastal Ocean Remote Sensing Conf.*, 6680-33.

Gibson, C. H., V. G. Bondur, R. N. Keeler, P. T. Leung (2006), Remote sensing of submerged oceanic turbulence and fossil turbulence, *International Journal of Dynamics of Fluids*, *2*(2), 111-135.

Leung, P. T. and C. H. Gibson (2004), Turbulence and fossil turbulence in oceans and lakes, *Chinese Journal of Oceanography and Limnology*, *22*(1), 1-23.

Leung, P. T., H. Prandke, A. Anis, V. Boundur, C. H. Gibson, N. Keeler (2006), In-situ measurements to understand the mechanism of submerged turbulence detections from optical satellites, paper presented at 39th International Liege Colloquium on Ocean Dynamics, University of Liege, Liege, Belgium.